Controlled Cracking and Shape Recovery in Polymers

by

Jiexi Huang

A dissertation submitted in partial fulfillment
of the requirements for the degree of
Doctor of Philosophy
(Mechanical Engineering)
in the University of Michigan
2014

Doctoral Committee:

Professor Michael D. Thouless, Chair
Professor Krishnakumar R. Garikipati
Professor William W. Schultz
Professor Shuichi Takayama

2014

Dedication

To my grandfather

A C K N O W L E D G M E N T S

I want to thank my advisor Prof. Michael Thouless. This thesis would not have been possible without his help, support and patience.

I would also like to thank my committee members, Prof. Shuichi Takayama, Prof. Krishna Garikipati and Prof. Bill Schultz, for the brilliant comments and suggestions. I am thankful for the excellent example of rigorous scholarship they have provided.

My collaborations with the co-authors on this work – Prof. Shuichi Takayama (Chapter 2-3), Prof. Steve Schwendeman (Chapter 4), Dr. Toshiki Matsuoka (Chapter 2), Byoung Choul Kim (Chapter 2), Dr. Chris Moraes (Chapter 2), J. Max Mazzara (Chapter 4), and Fanbo Meng (Chapter 3) – have been very productive and fun.

A special thanks to my family. Words can not express how grateful I am to my grandfather, grandmother, my mother and father for all their love and encouragement. And especially for my grandfather who has been the inspiration and motivation during my entire PhD. Thank you.

TABLE OF CONTENTS

LIST OF FIGURES

LIST OF TABLES

ABSTRACT

Controlled Cracking and Shape Recovery in Polymers

by

Jiexi Huang

Chair: Professor Michael D. Thouless

Cracks and pores in polymers can be used as functional micro/nano structures, enabling mass-processing fabrication that is simple and cost-effective. Such technologies are especially popular for biological applications. To unlock the full potential of these technologies, we need to understand the behaviors and the mechanics behind them. An accurate prediction and precise control of these traditionally stochastic processes are desired to enhance the precision and repeatability of subsequent experiments and analyses. For this purpose, a crack control strategy based on a coupling of Linear Elastic Fracture Mechanics (LEFM) and flaw statistics was developed, addressing the problem for a wide range of materials.

Channels fabricated by cracking can narrow and generate nanoconfinements accompanied by a nanoscale squeezing flow that can facilitate the linearization of DNA and chromatin. To develop optimal nanochannel operation parameters and avoid unfavorable partial collapse, the non-uniform closure of liquid-filled channels was studied. The analyses suggested time scales for different narrowing and closure conditions to occur which can be used as a reference to tailor the operation parameters. The study of an elliptic channel in an infinite elastic body reveals the change in shapes and sizes during crack closure, which helps characterize the channel geometry during the dynamic process and understand the capabilities and limitations of the technique.

Pores in viscoelastic polymers can heal spontaneously driven by interfacial tension. A finite element model was developed to investigate the effect of temperature and geometry on the healing process. Material characterization was conducted for a specific polymer of PLGA which is one of the most commonly used biomaterials. In comparisons of simulation with experimental observations, simulation successfully predicted the various healing time based on material properties and environment.

CHAPTER 1

Introduction

Nano-scale cracks can be formed in layered engineering structures when a brittle film is supported on a compliant substrate. Motivated by using cracking as a reliable and easy fabrication technique for nanochannels, a precise control mechanism for crack initiation and propagation must be developed with respect to the properties of the materials in which the patterns are created. This problem is addressed in Chapter 2, where we demonstrated different strategies for controlling crack arrays and showed that while precise control is possible in any materials, the method is more robust in systems with sufficient long flaws. Nanochannels fabricated by controlled cracking can be closed by relaxation of the strain that opened the cracks. The confinement and flow generated by closing the channels can facilitate biological studies including DNA linearization and chromatin analyses. The crack closure is complicated by the viscous fluid that it contains. In Chapter 3, we analyzed the time-dependent non-uniform closure of thick-walled channels, and provided strategies for operation of the channels. The closure of cracks in elastic substrates is a passive process as a result of the applied compression. Autonomic shape recovery can occur in viscoelastic materials driven by interfacial tension. Finite element models with interfacial tension were developed and simulations were conducted with independently measured material properties to predict the healing time. The effect of temperature and geometry is discussed in Chapter 4.

When a layered engineering structure of a brittle thin film supported on compliant substrate is subjected to applied tension, parallel arrays of cracks form in the film. Depending on the material properties, the cracks are contained in the film or penetrate into the substrate. The crack patterns are of sizes ranging from tens of nanometers to micrometers. This type of cracking has proven to be an easy and low-cost fabrication method for micro and nano fluidic channels with applications of DNA linearization and chromatin analyses [1,2]. The major limitation is the non-uniformity of cracks. While the cracks occur in parallel arrays under uniaxial tension, the spacings and sizes vary between individual cracks [3].

Since the behaviors of biomolecules in the channels strongly depend on the confinement of the channels, the variation in channel sizes results in fluctuation in the outcome of subsequent experiments [2]. It is important to eliminate or control the stochastic nature of cracking. Geometrical features can be used to trigger cracks at specific locations. While the basic idea is intuitive, it is not so obvious how to realize the concept in practice, nor what the limitations are.

Crack patterns depend on the interaction between intrinsic flaw population and the fracture mechanics of crack channeling. These two factors vary with selection of materials. The popular substrate materials used in micro/nano fluidic devices include silicon and polymers such as Poly(dimethylsiloxane) (PDMS) and Poly(methylmethacrylate) (PMMA). To create patterns with cracking, film materials are selected accordingly including silicon compounds such as silicon dioxide and silicon nitride [4], metal [3], other polymers that are more brittle [5] or oxidized surface layer of the substrate polymer [1, 2, 6, 7]. Based on the intrinsic flaw population, film materials can be categorized into two groups. The first group are materials with sufficient long cracks. Examples of this group include metal films by physical vapor deposition, and oxidized PDMS. Published fracture-mechanics analyses of characteristic crack spacings do not reflect the actual spacings. The first part of the second Chapter of this dissertation uses the energy-based approach to predict the actual crack spacings and provides guidelines for the design of crack control structures. The other group of materials have only short defects. The prediction of cracking in these materials requires incorporation of the flaw population. Such a coupling between linear-elastic fracture mechanics (LEFM) and flaw statistics has not been presented before. In the latter half of Chapter 2 we predicted the natural crack distribution and proposed a different crack control strategy for this group of materials.

Nanochannels fabricated by tunneling cracking have tunable cross-sectional areas. This allows the flexibility to load the bio-molecules in the channel when it is in the widely open state to avoid damages, and to manipulate the molecules in nano confinements provided by closed channels. The crack closure of cracks in elastic substrates is usually considered as a reversed process of crack opening that is time-independent. When used as nanochannels, the cracks are filled with viscous substances that impede the closing, generating a flow and resulting in non-uniform closing along the length of the channel. The combination of flow and nano-confinement has proven to be more effective for DNA linearization compared with the traditional methods [2]. To understand the DNA and chromatin linearization process, the flow parameters and the channel dimensions under different strain conditions are

desired. More importantly, we need to develop optimal nanochannel operation parameters to avoid unfavorable conditions such as partial collapse of the channel that are sometimes observed in experiments [2]. Channels made by cracking have elliptic cross-section. The non-uniform crack closure also include shape change, which affect the level of confinement it can provide. In Chapter 3 an analysis of flow generated during channel narrowing using a uniform cylindrical tube is presented as a first approximation, followed by the study of non-uniform closure of axisymmetric thick-walled and elliptic channels in thick substrates.

Another type of healing of deformations in polymer is discussed in Chapter 4. The materials of interest are Poly(lactic-co-glycolic acid) (PLGA), which is one of the most popular biomaterials used in sutures, cadiovascular stents [8], and drug delivery devices [9–12]. The autonomic healing of pores in PLGA microspheres plays an important role in the drug release process [13] and can be used for microencapsulation of drugs and proteins [12]. The healing of intrinsic pores in PLGA microsphere are at a very small scale (nm) and occur both on and beneath the surface. Therefore, direct visualization is very difficult. As a simplified model, healing of surface indentation in PLGA films was measured and monitored by light microscopy [14], where the size of indentations was limited to be much larger (μm) than the pores in microspheres. We will use computational methods to obtain a better understanding and predict the healing time in porous PLGA microspheres. The healing process is modeled by viscous flow of materials driven by high surface tensions. In order to test the validity of the model, properties of thin PLGA films were measured and used in numerical calculations to compare the predicted healing time with experimental observations. The effect of temperature and geometries of the pores are studied.

CHAPTER 2

The control of crack arrays in thin films

2.1 Introduction

Quasi-periodic arrays of occurs in layered engineering structures when a brittle film is supported on a substrate. The general formation of these arrays depends on the geometry, the properties of the film, interface and substrate, and the tensile strain. However, the details of the arrays are governed by stochastic factors such as the distribution of the intrinsic flaws, and the sequence in which cracks initiate from these flaws. Crack arrays can be used for nano-fabrication purposes, and some recent experimental examples have been presented in the literature [1, 2, 15–17]. However, for the potential of these fabrication techniques to be fully realized, the stochastic nature of the cracking has to be eliminated or controlled. Such controlled cracking has been demonstrated in a silicon nitride film deposited on a silicon wafer [4], in a gold film on a poly(dimethylsiloxane) (PDMS) [7], and in the surface layer of oxidized PDMS [7]. While these examples show that it is possible to control crack patterns under some conditions, it is not clear the extent to which these patterns can be robustly controlled. In this paper, we use the mechanics of crack propagation to elucidate the answers to this question, and to provide strategies for controlling crack patterns in different types of materials.

Existing analyses for the formation of crack arrays fall into two groups: shear-lag and linear-elastic fracture mechanics (LEFM) analyses. The shear-lag analyses that consider the statistics of flaw populations [18–20] were generally developed for studies of crack arrays in laminated composites and the fragmentation of fibers embedded in a matrix, but also apply to the fracture of films on ductile substrates. A characteristic feature of shear-lag analyses is that once a pair of neighboring cracks are close enough to interact, it is impossible to introduce a third crack between them, no matter what level of strain is applied. If a fully-populated crack array is generated at one unique level of stress (Fig. 2.1a), these anal-

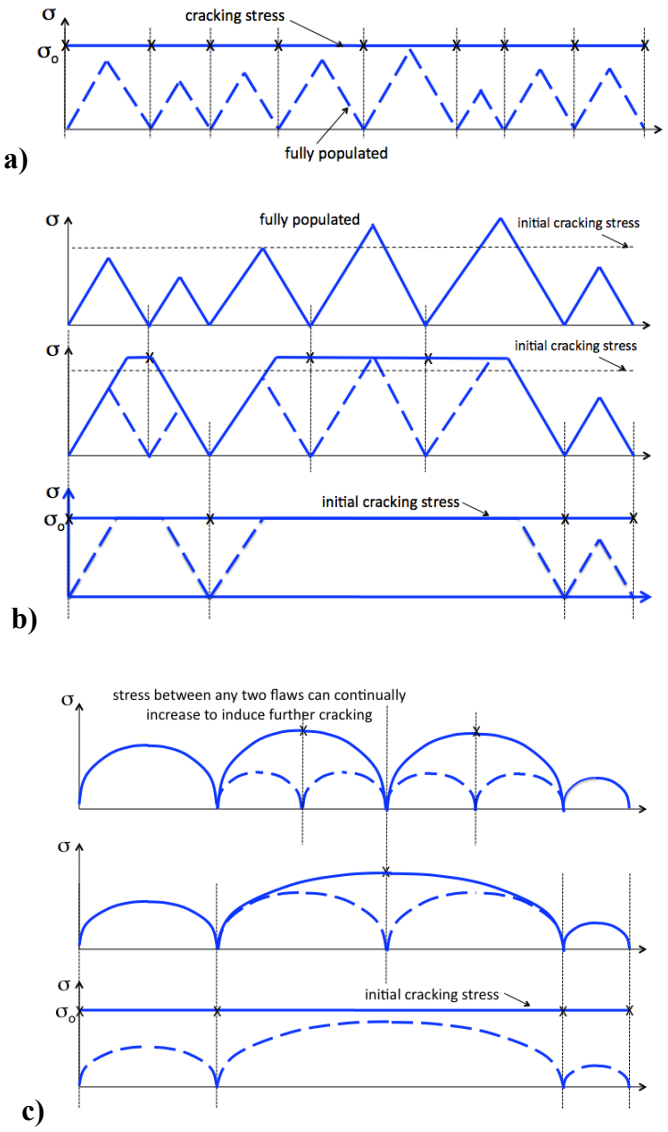

Figure 2.1: **(a)** If there is a single value for the cracking stress. a shear-lag model predicts the formation of a crack array at a single value of stress, with the crack spacing given by the solution to the ”car parking” problem. **(b)** If there are multiple cracking strengths, a shear-lag model predicts an increasing density of cracks until a saturated array is formed. **(c)** In an elastic problem, the stresses can continue increasing between two cracks, and further cracks can always channel between them, provided there is a suitable flaw to inititiate the crack.

yses result in the well-known solution to the "car-parking problem" [21, 22] that predicts a crack array with a spacing that varies by a factor of two, and a mean spacing of 1.337 times the smallest spacing. However, this simple result is not valid if the flaws are of different sizes, so that they can be activated by different stress levels (Fig. 2.1b) [19]. Furthermore, under conditions in which LEFM is appropriate, when there is so little delamination or interfacial slip that it occurs over distances much less than the crack spacing and the the shear stress on the interface is essentially unbounded, the maximum stress between two cracks can always be increased by additional loading (Fig. 2.1c). This means that it is always possible to introduce a third crack between two neighboring cracks, no matter how close they might be.

Published fracture-mechanics analyses of crack arrays have all been predicated on the assumption that there is a very high density of long flaws. Furthermore, only characteristic spacings have been obtained [23–27], with various assumptions about how these might be related to the average spacing. The analyses consider problems in which the cracks are limited to the thickness of the film [23–26], and those in which they can extend into the substrate [3, 27–29]. The mechanics of both situations is similar. When the strain in the film is equal to ϵ_o, the characteristic spacing of the array, s_{ch}, is of the form:

$$\frac{s_{ch}}{h} = f_2\left(\alpha,\beta,\frac{\Gamma_f}{\Gamma_s},\frac{{\epsilon_o}^2\bar{E}_f h}{\Gamma_f}\right). \tag{2.1}$$

In this expression, h is the film thickness, Γ is the toughness, the subscripts f and s denote the film and substrate respectively, the Dundurs' parameters for the modulus mismatch across the interface, α and β are given by [30]

$$\alpha = \frac{\bar{E}_f - \bar{E}_s}{\bar{E}_f + \bar{E}_s} \tag{2.2}$$

and

$$\beta = \frac{\bar{E}_f f(\nu_s) - \bar{E}_s f(\nu_f)}{\bar{E}_f + \bar{E}_s}, \tag{2.3}$$

where $\bar{E} = E/(1-\nu^2)$ and $f(\nu) = (1-2\nu)/[2(1-\nu)]$ in plane strain, E is Young's modulus, and ν is Poisson's ratio. However, the relationship between the characteristic spacing that can be calculated by LEFM and the actual spacings in an array have not be established. It depends on the interaction of two effects: the distribution of the intrinsic flaws responsible for initiating cracks, and the fundamental mechanics of the problem. In particular, LEFM dictates how the energy-release rate for a given flaw depends on both its length and

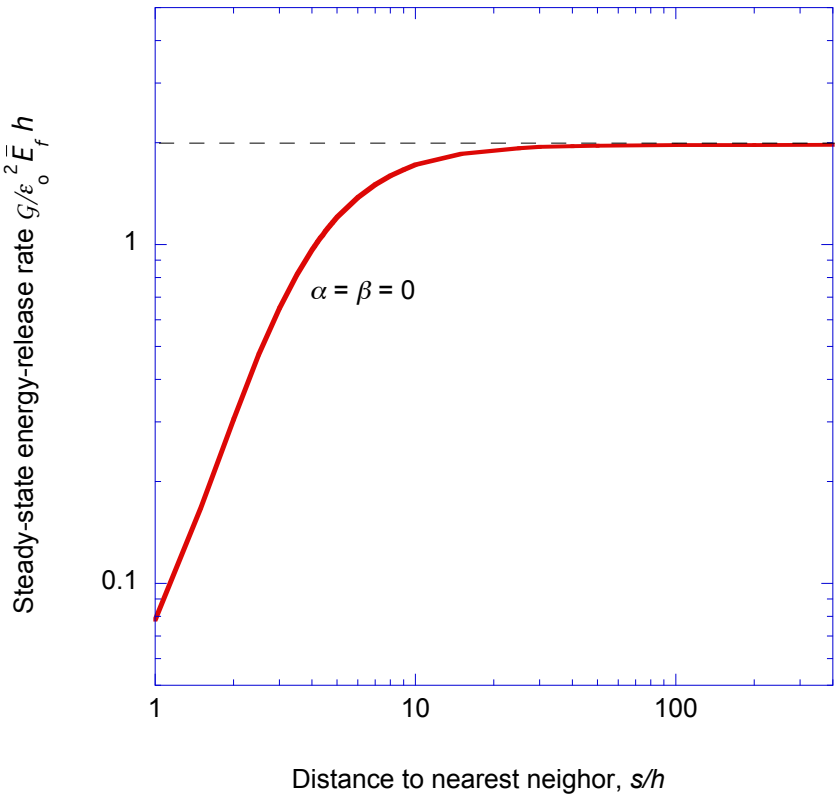

Figure 2.2: The energy-release rate for channeling a crack across the surface of a film depends on the distance to its two nearest neighbors (assumed to be equi-distant in this plot).

distance from longer neighboring cracks. The energy-release rate for a crack that is relatively short compared to the film thickness increases linearly with crack length; whereas, the energy-release rate for a relatively long crack scales linearly with film thickness (and is independent of crack length). Similarly, as illustrated in Fig. 2.2, cracks that are very close to their neighbors have reduced energy-release rates, while cracks that are further away have energy-release rates that are independent of spacing.

The underlying motivation of this chapter is to understand possible strategies for controlling crack arrays. The structure of this chapter consists of two parts. The first part contains analyses of the creation of uniform arrays, based only on fracture-mechanics concepts and ignoring statistical aspects of the problem. The analyses assume a sufficient density of long flaws, and further assume that the role of any artificial features is to project flaws at their tips sufficiently far to ensure that they will channel preferentially. These analyses are performed for crack arrays confined to a surface layer, and also for crack arrays that can penetrate into the substrate, as appropriate for stiff films on very compliant substrates. In the second part of this paper, the interaction of thin-film fracture mechanics with the

statistics of an intrinsic flaw population is addressed. The model is first used to analyze how natural crack patterns evolve with strain in the absence of geometrical features. It is subsequently used to analyze how artificial geometrical features, the statistics of an intrinsic flaw population, and LEFM can interact to create uniform crack arrays.

2.2 Fracture mechanics of controlling crack patterns

Fracture-mechanics models without including statistical effects are first used to illustrate a simple strategy for controlling crack patterns. The first case considered is a simple one where the modulus of the film and substrate are equal, and the cracks are confined to a surface layer of thickness, h. The second case considered is one in which the film has a much higher modulus than the substrate, so that the cracks penetrate into the substrate. This second case is complicated by the fact that an increase in strain can either drive existing cracks deeper into the substrate, or cause additional cracks of unknown depth to channel across the system. However, it will be seen that the two processes occur in sequence, so only when existing cracks have reached a critical depth (relative to their spacing) do additional cracks channel between them.

We used cracking of a stiff brittle oxidized layer on a compliant elastomeric (PDMS) substrate upon an applied remote tensile strain to fabricate nanochannel devices for biological applications. As shown in Fig. 2.3, two parallel reservoirs of $100\,\mu$m size are patterned in a PDMS slab by ordinary soft lithography. A remote tensile strain is applied to create parallel cracks connecting the reservoirs [2] . The size of these nanochannels can be adjusted by adjusting the applied strain. Biomolecules such as DNA and chromatin are added in reservoirs and can flow into the nanochannels. Once loaded in the nanochannels, the biopolymer can be linearized by gradually releasing the strain and narrowing the cracks. The uniformity of the nanochannels affects the quality of DNA linearization. This is a motivation for the following analyses.

In the following analyses, it is assumed that cracks are initiated from flaws along a free edge. The lengths of the flaws are sufficient to ensure that the energy-release rates are independent of crack length, and the density of the flaws is sufficient to ensure that cracks will propagate preferentially from wherever the local stress is a maximum. Periodic geometrical features separated by a distance S_o serve to provide locations where the intrinsic flaws extend well beyond their neighbors. A schematics of the patterned specimen used

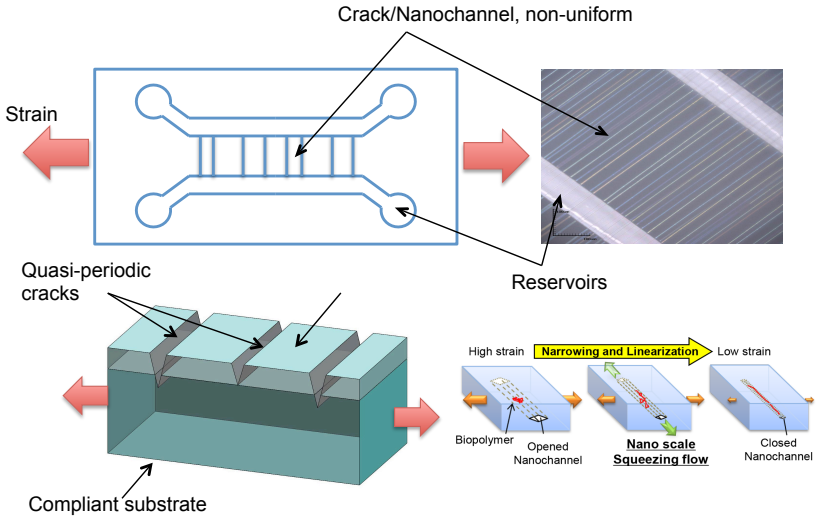

Figure 2.3: Schematics showing nanochannel device fabricated by cracking of thin brittle film supported on compliant substrate. Cracks form nanochannels connecting the reservoirs. Biopolymers loaded in the channels can be linearized by narrowing the cracks.

in the experiment is shown in Fig. 2.4. If the applied strain is sufficiently small, so that the exclusion length between cracks is greater than S_o, cracks will channel from the tips of only some of the geometrical features. In particular, flaws along the straight edges of the structure will be in the shadow of the geometrical features, and will not initiate cracks. As the strain is increased, more of the geometrical features will be associated with channel cracks. Eventually, the strain will be so large that the exclusion distance will be less than S_o, and at this point defects along the edge can initiate channel cracks. Therefore, tailoring the structure so that the spacing of the geometrical features corresponds to the desired spacing of the crack array requires a delicate balance between the applied strain and the properties of the film and substrate. Too low a strain will result in a random array of cracks initiated from only a limited set of features. Too high a strain will result in random cracks being initiated from flaws away from the features. This concept is first illustrated by relatively simple analyses corresponding to cases when the cracks do not penetrate into the substrate.

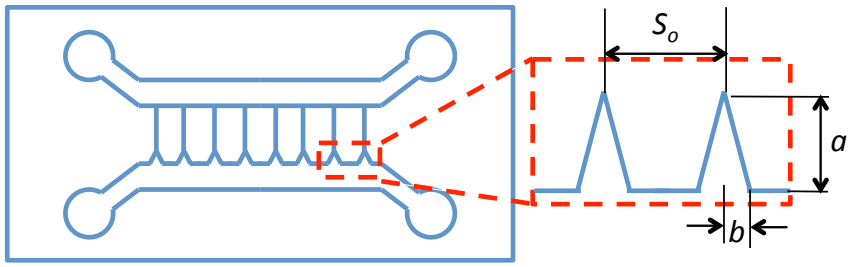

Figure 2.4: A schematic showing the patterned substrate with controlled cracking as nanochannels. The geometrical features are the sawtooth structure along the edge of the lower reservoir. Controlled crack array propagates from the tip geometrical features connecting the two reservoirs. The geometrical features are separated by a distance S_o and are with dimensions a and b.

2.2.1 Crack arrays limited to the film

The calculations were done by computing the energy change associated with introducing a steady-state crack in the middle of two existing cracks separated by a distance of $2s$. Although standard fracture-mechanics results from Tada *et al.* [31] can be used to analyze a homogeneous system, numerical calculations are required when the effects of a modulus mismatch are included.

The numerical calculations were done in two steps (Fig. 2.5). In the first step, the stress distribution $\sigma(y)$ along the mid-plane between two cracks at a distance $2s$ apart was calculated for a given value of strain, ϵ_o. In the second step, a crack was introduced along this plane, with surface tractions corresponding to $-\sigma(y)$ applied along the new crack surface. The resultant crack-opening displacements $u(y)$ were computed, and the steady-state energy-release rate, $\mathcal{G}_{ss}$, calculated from [32]

$$\mathcal{G}_{ss} = \int_0^h \sigma(y)u(y)dy/h. \tag{2.4}$$

The condition for whether a crack can channel was calculated by comparing this energy-release rate to the toughness of the film, Γ_f. The final step of the calculations involved equating the separation, S_o, of the geometrical features to $2s$. When S_o is sufficiently large to permit a new crack to propagate, a random crack array will be generated, because cracks can be formed away from the geometrical features. Conversely, if $2S_o$ is smaller than the

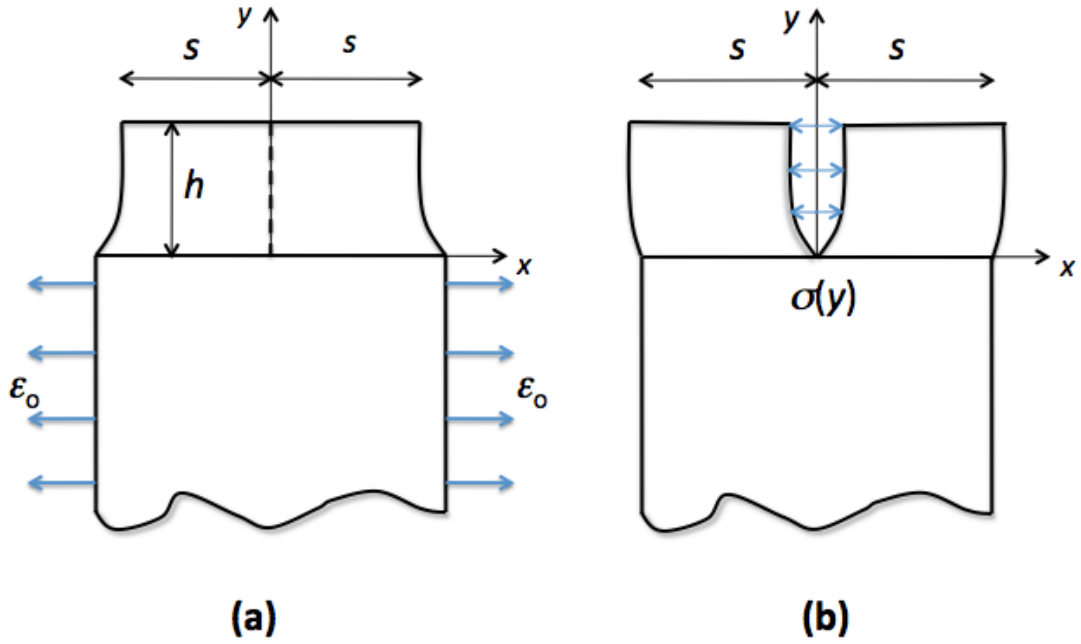

Figure 2.5: A schematic showing the process by which the energy changes associated with introducing a steady-state crack between two pre-existing cracks are calculated. In **(a)**, the stress distribution $\sigma(y)$ along the mid-plane between two cracks at a distance $2s$ apart is calculated for an applied strain of ϵ_o. In **(b)**, a crack is introduced along this plane, with surface tractions corresponding to $-\sigma(y)$ applied along the new crack surface, and the resultant crack opening displacements $u(y)$ are calculated.

distance that will allow an intermediate crack to propagate, then not every feature will have a crack associated with it and, again, there will be a random aspect to the crack pattern. There will, however, be a "Goldilocks" regime which is "just right" for propagating cracks from every feature, but no more. This regime is shown in Fig. 2.6 and 2.7, with and without modulus mismatch. As indicated in these figures, careful matching between the feature separation, the properties of the material, and the applied strain is required to realize perfectly periodic arrays.

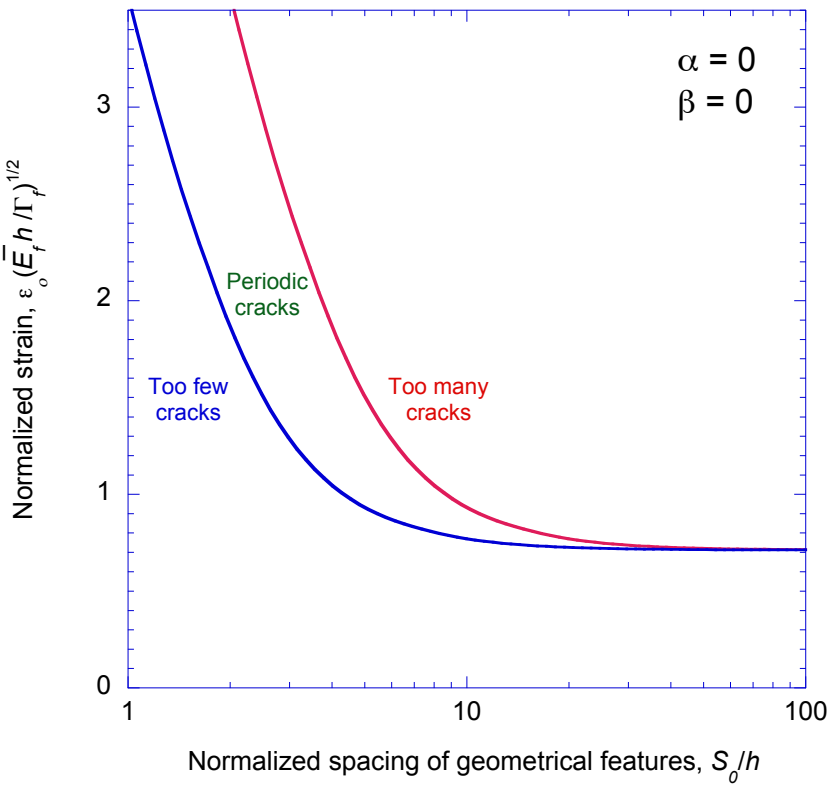

Figure 2.6: A plot showing the regimes of strains and feature spacing in which periodic crack arrays contained within the film can be obtained for a film with no modulus mismatch.

These conclusions are consistent with the experimental observations described by Kim *et al.* [7]. In their study, "V"-shaped notches were formed in poly(dimethylsiloxane) (PDMS) substrates using soft lithographic techniques. In particular, a 5:1 mixture of curing agent and PDMS (Sylgard 184, Dow Corning) was cast against silicon moulds and cured at 60 °C. The surface was plasma treated to create a thin surface layer of a relatively brittle silica-like material. While the material properties of this surface layer are not well-characterized, there is evidence that the modulus is only slightly higher than that of the substrate, and not large enough to drive cracks to significant depths within the substrate [1]. As shown in Fig. 2.8, a systematic increase in applied strain to this micro-patterned system results in a crack pattern that evolves from (i) random cracking at some of the notches, through (ii) periodic cracking at every notch, to (iii) random cracking at locations away from the notches.

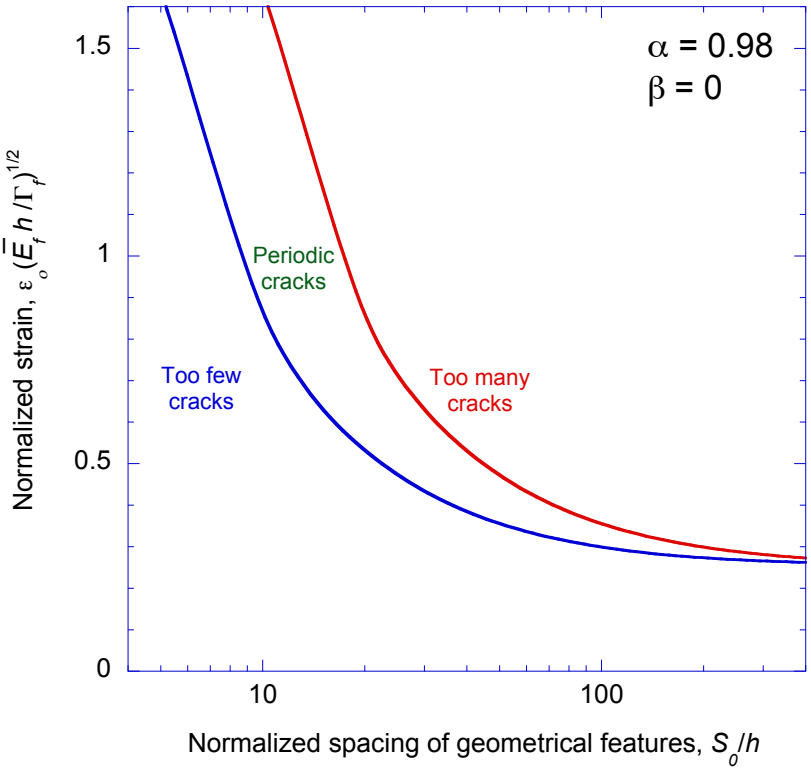

Figure 2.7: A Plot showing the regimes of strains and feature spacing in which periodic crack arrays contained within the film can be obtained for a film with a modulus mismatch corresponding to a value of $\alpha = 0.98$, and $\beta = 0$. (The film-to-substrate thickness ratio is 10^{-4}.)

2.2.2 Crack arrays penetrating into the substrate

A large modulus mismatch, such as that between a gold film and PDMS, results in the crack arrays penetrating relatively deep into the substrate [3]. This complicates the mechanics analysis because an increase in strain can result in two possible events: (i) the growth of existing cracks deeper into the substrate, or (ii) the channelling of intermediate cracks of unknown depth. In this section, a fracture-mechanics analysis is presented to determine the conditions required to control such crack arrays.

The analysis was done in a similar fashion to that of the previous section, and is illustrated by Fig. 2.9. In the first step, the strain that would just cause two existing cracks of depth a_o separated by a distance $2s$ to begin penetrating deeper into the substrate was determined. Then, the stress distribution, $\sigma(y)$, along the mid-plane between these two

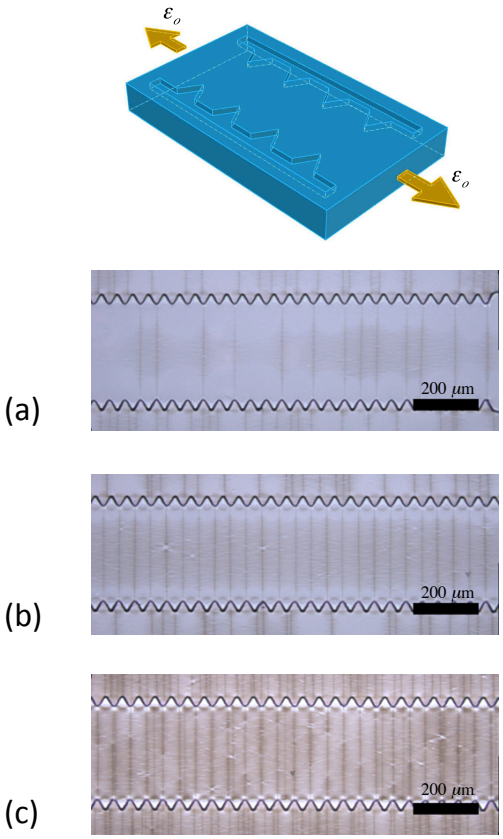

Figure 2.8: Micrographs showing the three regimes of cracking for an oxidized sample of PDMS, with **(a)** too few cracks, **(b)** one crack on each geometrical feature, and **(c)** too many cracks.

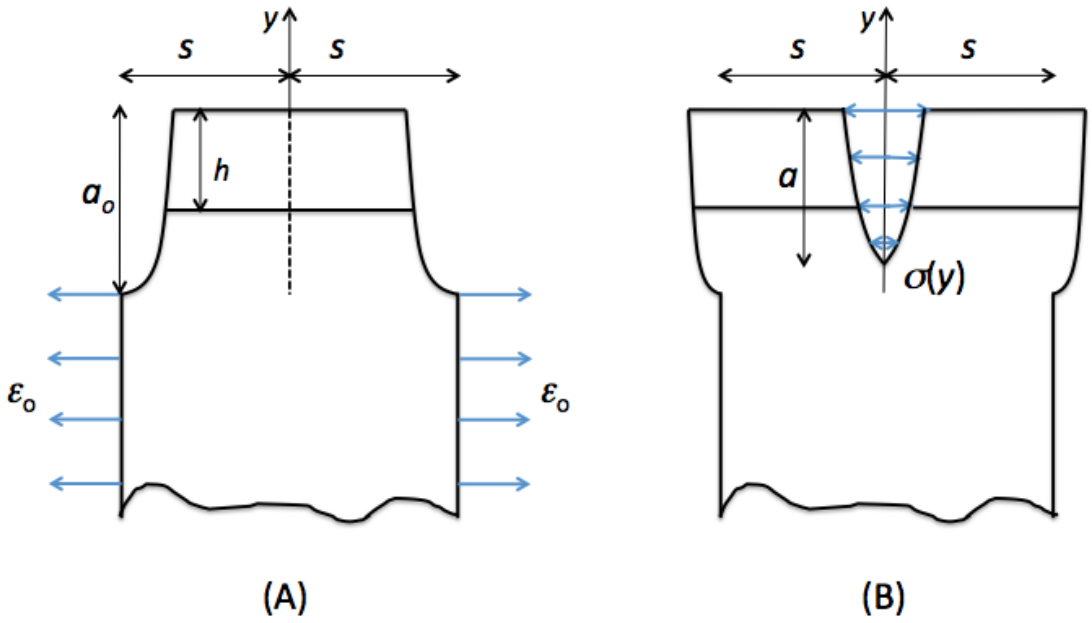

Figure 2.9: A schematic showing the process by which the energy changes associated with introducing a steady-state crack that propagates into the substrate between two existing cracks of depth a_o, separated by a distance $2s$. In **(a)**, the strain that would just cause the existing cracks to penetrate deeper into the substrate is determined. Then, the stress distribution, $\sigma(y)$, along the mid-plane between these two cracks is computed for this strain level. In **(b)**, a crack is introduced to an arbitrary depth a, with surface tractions corresponding to $-\sigma(y)$ along its surface. The corresponding crack-opening displacements, $u(y)$, are calculated.

cracks was computed for this strain level. In the next step, a crack was introduced along this plane to an arbitrary depth, a, with surface tractions corresponding to $-\sigma(y)$ along its surface. The corresponding crack-opening displacements, $u(y)$, were calculated, and the energy-release rate for channelling calculated from

$$\mathcal{G}_{ss} = \int_{h-a}^{h} \sigma(y)u(y)dy/a. \tag{2.5}$$

This energy-release rate was compared to the effective toughness

$$\Gamma = (h/a)\Gamma_f + (1-h/a)\Gamma_s, \tag{2.6}$$

to find whether an intermediate crack can form for any value of a. If no crack could form, the applied strain was increased, a new equilibrium crack depth for the original cracks determined, and the calculation was repeated.

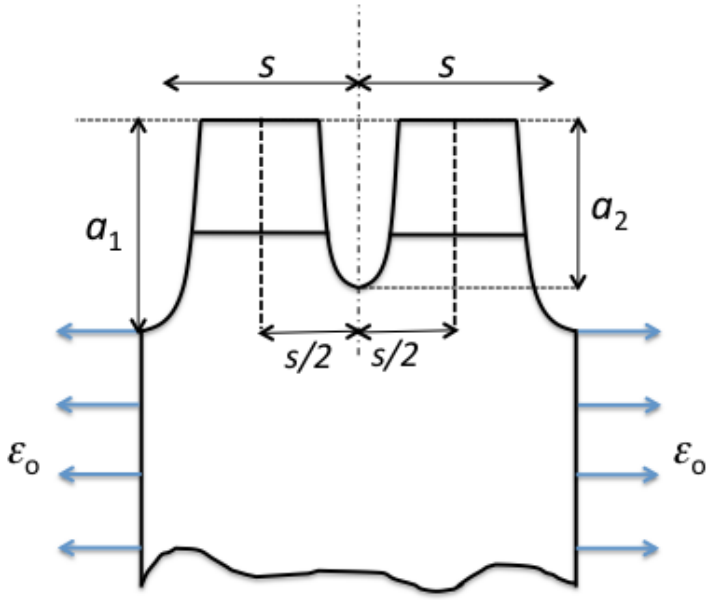

Figure 2.10: The secondary crack that is formed is shallower than the pre-existing cracks. A second set of calculations is then required to compute which cracks will grow, and the conditions for whether a tertiary set of cracks can channel between the other two sets.

The calculations were repeated until an intermediate crack of arbitrary depth could just be formed. At this stage, the calculations were repeated for all three cracks (Fig. 2.10), ex-

ploring the possibilities of either introducing another set of intermediate cracks or growing the existing cracks. These calculations revealed the sequence of cracking for this problem. The intermediate crack is first formed at a shallower depth than the original pair of cracks, and immediately unloads the original cracks. While further increases in strain increase the energy-release rate at the tips of all the cracks, only the shallower intermediate crack meets the condition to grow deeper. Eventually, it reaches the depth of the original cracks. Furthermore, during this stage, it is not thermodynamically possible to introduce any further intermediate cracks. Once all cracks are at the same depth, further increases in strain allows the entire set to propagate deeper, until eventually another set of shallow intermediate cracks can be introduced, and the entire sequence is repeated.

Following the approach and assumptions of the previous section, Fig. 2.11 shows the range of strains for which the crack spacing will match that of the geometrical features in a system for which the film modulus is 10^4 times higher than the substrate modulus, so that $\alpha = 0.9998$ and $\beta = 0$, and the film-to-substrate toughness ratio, Γ_f/Γ_s, is 35. This figure shows the same important conclusions that are evident from Fig. 4. There is a limited range of strains over which periodic cracking can be reliably obtained; channel cracks will be initiated at only some of the features if the strain is too low, and they will be initiated from sites away from the features if the strain is too high.

A new aspect of the problem is the prediction of how the crack depths evolve within the regime where the crack spacing matches the feature spacing. Figure 2.12 shows how the crack depths are initially bimodal at the lowest strain for which uniform cracking is obtained, with the newest cracks being shallower than the original ones. An increase in strain results in the growth of the new cracks, while the original cracks remain at their original depth (assuming no healing), until all the cracks are of the same depth. From this point on, an increase in strain causes all the cracks to grow deeper in a uniform fashion, until a new set of cracks is introduced.

Experimental observations of Kim *et al.* [7] for the three cracking regimes are shown in Fig. 2.13 for this situation where there is a huge modulus mismatch between the film and substrate, and the channeling cracks propagate far below the interface [3]. A similar process to that described in the previous section was used to fabricate a PDMS substrate with notches in it. A 10 nm adhesion layer of Cr was deposited by e-beam on the surface of the PDMS, followed by a 40 nm thick Au layer. Laser interferometry confirmed that the cracks which formed upon the application of a tensile strain were approximately 3 to 4

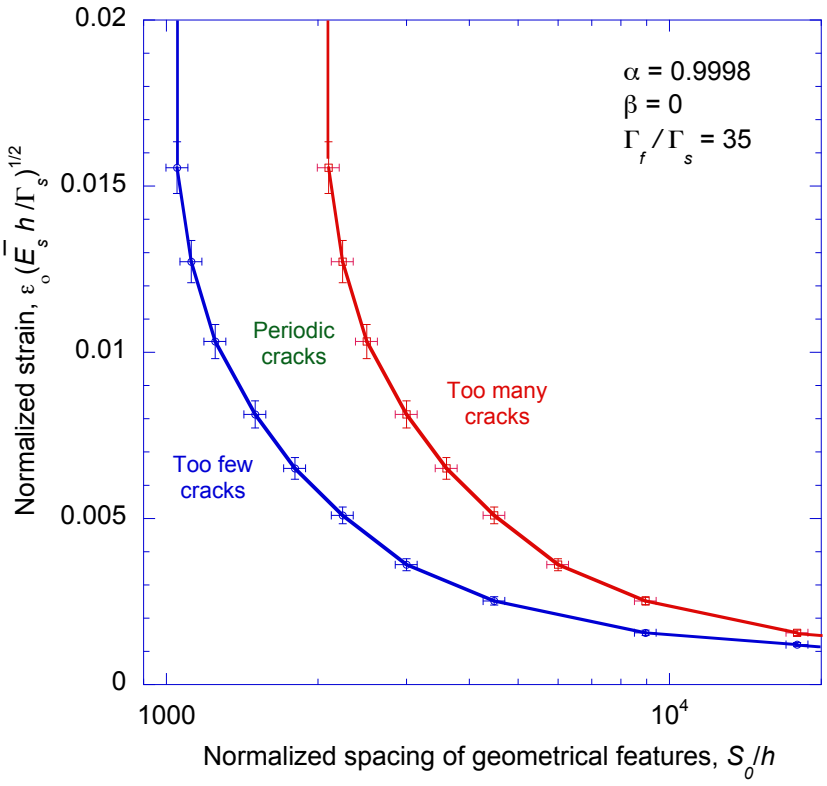

Figure 2.11: A graph of strains over which periodic arrays of cracks can be obtained. An identical figure is obtained if the calculations are repeated with $\Gamma_f/\Gamma_s = 0$, but the cracks can not form unless the strain in the film is 1%. (The film-to-substrate thickness ratio is 10^{-4}.)

microns deep, or 60-80 times deeper than the total film thickness.

The numerical predictions for the crack depth are very sensitive to the choice of Γ_f/Γ_s. For the results shown in Figs. 2.11 and 2.12 , this ratio was chosen to be 35, to give a relatively deep crack for illustrative purposes. However, thin metal films will have a low toughness, because of the lack of thickness in which to develop a plastic zone. A relatively tough film is required to predict crack depths that are consistent with the experimental observations, but such a toughness is not realistic for the metal films associated with these observations. This paradox can be resolved by recognizing that, in the absence of a significant constraint from a relatively stiff substrate, thin metal films can rupture by shear localization [33] upon yield at very high strains. In particular, it should be noted that the results of Figs. 2.11 and 2.12 are reproduced exactly if the calculations are repeated with the coupled assumptions that $\Gamma_f/\Gamma_s = 0$ and that cracks cannot form unless the strain in

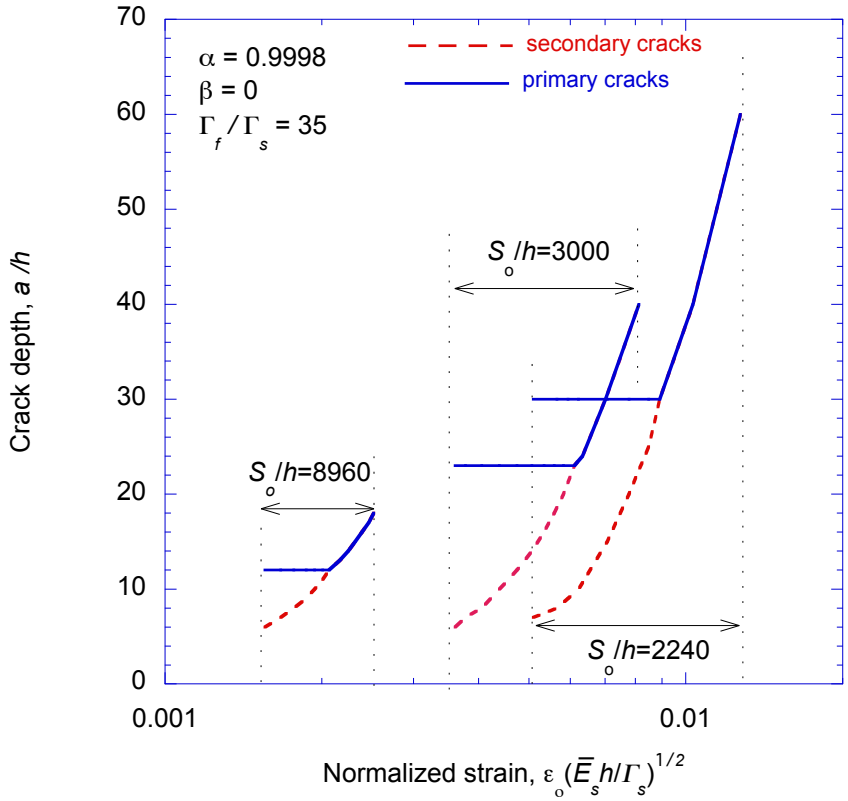

Figure 2.12: Plots of how the crack depths vary with strain within the regime for which there is a uniform crack spacing. The solid lines correspond to the primary cracks, and the dashed lines correspond to the secondary cracks formed at the beginning of each strain range. (The film-to-substrate thickness ratio is 10^{-4}.)

the film equals 1%. This would seem to be the appropriate form in which the calculations should be conducted for very thin, high-strength metal films supported on compliant substrates.

2.3 Statistical effects on crack arrays

In this section, statistical aspects are included to investigate how crack arrays are affected by the distribution of flaw sizes and density. The calculations were done by performing Monte Carlo simulations on a homogeneous system with a film of thickness h, in which cracks did not penetrate the substrate. Before investigating the effect of geometrical features on array formation, an analysis of how natural crack arrays are generated in uniform structures was done as a point of comparison, and because such a coupling between LEFM

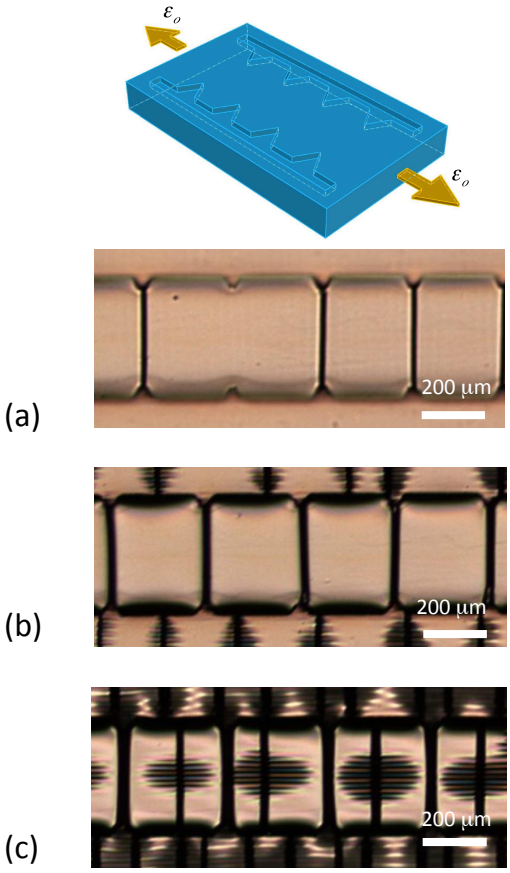

Figure 2.13: Micrographs showing the three regimes of cracking for a sample of PDMS coated with a 10 nm Cr layer (used as an adhesion layer) and 40 nm of Au: **(a)** with too few cracks, **(b)** one crack from each geometrical feature, and **(c)** too many cracks.

and flaw statistics for thin-film fracture has not been presented before. Even for flaw populations that meet the conditions usually assumed (dense, long flaws), fracture-mechanics analyses cannot predict the sequence in which crack arrays form, or what the mean spacing of an array might be. This information can only be obtained by incorporating some statistical aspects of the flaw population into the analysis, even in the case when all the flaws are so long that LEFM would predict that each individual flaw on its own would propagate at the same stress level.

2.3.1 Statistical distribution of intrinsic flaw

The intrinsic flaw sizes were approximated by truncating a Gaussian distribution with a normalized standard deviation of μ/h and centered about zero to the interval of $(0, \infty)$. This distribution results in a monotonically decreasing probability with increased flaw size. Based on the assumption of all cracks are initiated from a free edge of the structure, the defects are in one-dimensional components. The density of the defects in a fiber is often approximated by a Poisson process [34]. According to the Poisson model, the positions of flaws can be equally generated from a uniform distribution over the same length [35]. The location of the flaws was assumed to be distributed uniformly along a length of L with a uniform normalized density of ρh, where ρ is the density per unit length.

2.3.2 Energy-release rate at the tip of a crack

Three parameters determine the energy-release rate at the tip of a flaw: (i) the local strain, (ii) any shielding that may be provided by neighboring cracks, and (iii) the length of the flaw. In order to simplify the analysis, various assumptions were made about these parameters. Any flaws on the edge of geometrical features were assumed to experience a local strain, ϵ_l, elevated above the remote applied strain, ϵ_o, as given by the Inglis solution for the stress concentration at the surface of an ellipse [36]. The effect of shielding was assumed to be determined by the distance to the nearest crack (or geometrical feature) that extended beyond the tip of the crack being analyzed. Figure 2.14 shows examples of how this closest spacing was determined. The appropriate energy-release rate for an individual flaw was then calculated from the local strain and this distance, making a further approximation that the flaw was equidistant to two neighbors at this minimum spacing.[1]

In a homogeneous system, where $\alpha = \beta = 0$, the non-dimensional energy-release rate at the tip of a defect is given by $\mathcal{G}/(\bar{E}_f \epsilon_l^2 h)$, where ϵ_l is the local strain the defect is subjected to. The energy-release rate is determined by two features of a flaw including its length and any shielding that may be provided by neighboring cracks. For a single crack of length, a, the energy release rate is given by:

$$\frac{\mathcal{G}}{\bar{E}_f \epsilon_l^2 h} = \begin{cases} 1.98 & \text{if } a/h > 0.50 \\ 1.25\pi a/h & \text{if } a/h \leq 0.50 \end{cases} \tag{2.7}$$

[1] This approximation could be relaxed by doing a series of calculations for the energy-release rate of cracks not spaced symmetrically between two other cracks. However, it is not expected that this would have a significant affect on the results.

In order to find out the effect of interactions between cracks on the energy release rate, we performed finite element analysis on the energy-release rate to channel a crack across a film in the middle of a pair of cracks that have channeled. The cracks were from a free edge of a uniform structure, and the cracks were subjected to a same applied strain of ϵ_o. Mechanics analyses of thin-film cracking problems are generally predicated on the assumption of a sufficient density of long flaws, so that the crack pattern is not limited by the availability of long flaws which act as initiation sites for crack channeling. Fig. 2.2 shows that the energy-release rate of a long flaw depends on its distance from its nearest neighbors that have already channeled. It was assumed that the crack was equi-distant to its two nearest neighbors on each side. The energy-release rate decreases from the steady-state value of 1.98 at a fixed applied strain as the distance to the nearest cracks decreases. In other words, for a given level of applied strain, two cracks can be close enough to exclude a third rack from growing between them. [25]. Equivalently, any defect that is too close to a neighboring fully-developed crack will not grow, no matter how large it is [37]. This exclusion distance is the maximum distance two cracks can be separated in an array at a given strain, and half the distance is the minimum separation. We will discuss more about the exclusion distance later.

Figure 2.2 was used to determine an empirical equation for the relationship between the energy-release rate at the tip of a long crack, the strain and the distance, d, to the nearest (longer) neighbor:

$$\frac{\mathcal{G}}{\bar{E}_f \epsilon_l^2 h} = 1.98(1 - e^{-0.172 d/h}). \tag{2.8}$$

The energy-release rate for a short crack of length a was assumed to be equal to that of an edge crack [31], with the effect of crack spacing being of the same functional form as for long cracks, so that

$$\frac{\mathcal{G}}{\bar{E}_f \epsilon_l^2 h} = 1.25\pi \frac{a}{h}(1 - e^{-0.172 d/h}). \tag{2.9}$$

The calculation proceeded by seeding the geometry of interest with a statistical distribution of cracks, evaluating the distances, d, to all the nearest longer neighbors, and using this distance to calculate the energy-release rate for every crack as being the smallest of either Eqns. 2.8 or 2.9. The energy-release rate was then compared to the toughness of the film, so as to obtain information about which cracks would propagate at a given level of

strain. With a linear-elastic system, the calculations for any individual crack only needed to be performed once, since it was assumed that the energy-release rate is not affected by the growth of any nearest longer crack.

2.3.3 Determining the local strain

The local strain is determined by the geometry and the relative position of a crack on the geometry. In the following analyses, we consider two types of geometries: (i) flat edge, and (ii) flat edge with an array of elliptical structures. For both types of geometries, we consider the specimen to have a length of L, and is subjected to an applied uniaxial tensile strain of ϵ_o. The cracks are under tension. In a uniform structure, in the absence of flaws, the local strain is simply equal to the applied strain ϵ_o. In structures with elliptical features, the local strain was approximated to be the local tensile strain at the surface of an elliptical hole [36], and is given by:

$$\frac{\epsilon_l}{\epsilon_o} = \frac{\sinh 2\phi + e^{2\phi}\cos 2\theta - 1}{\cosh 2\phi - \cos 2\theta} \tag{2.10}$$

Where the ellipse is defined in the curvilinear coordinates as:

$$\begin{aligned} x &= c\cosh\phi\cos\theta \\ y &= c\sinh\phi\sin\theta \end{aligned} \tag{2.11}$$

Away from the elliptical structures, the local strain decreases to the uniform applied strain.

2.3.4 Exclusion distance

A crack, once occurred, releases the local strain and creates an exclusion distance in its vicinity within which any incipient defect is precluded from growing unless the applied strain is increased. In our analysis, in order to simplify the analysis, various assumptions were made. The effect of shielding was assumed to be caused only by cracks (or geometrical features that extended beyond the tip of the crack being considered. A second assumption was that the effect of shielding on an individual crack is determined by the distance to the nearest longer neighbor. Fig. 2.14 shows examples of how this closest spacing was determined. The appropriate energy-release rate of an individual crack was then based on this distance, making the approximation that it was equidistant from two nearest neighbors at that spacing, so that the curve of Fig. 2.2 could be directly used.

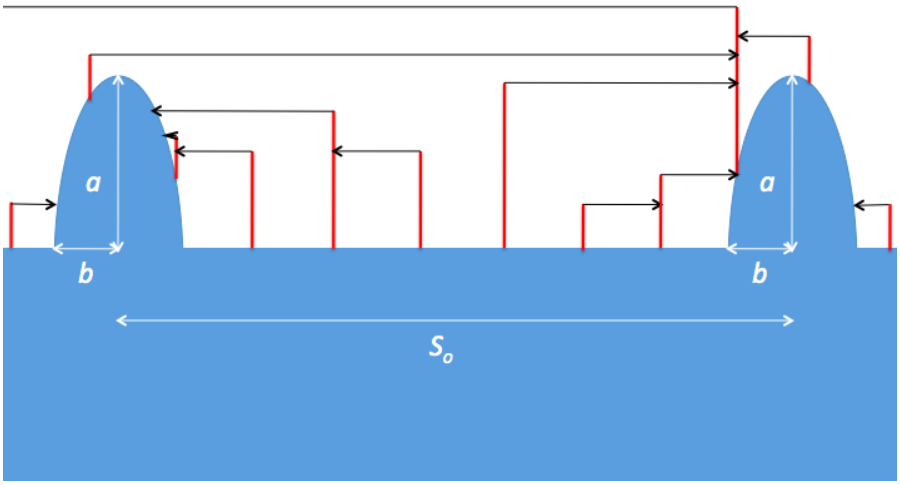

Figure 2.14: A schematic of a structure showing cracks and geometrical features. Elliptical features with major and minor axes a and b are separated by a distance S_o. Flaws are introduced along the free edge of the structure with a density ρ, with a statistical variation in crack length. The energy-release rate is based on the length of an individual crack and the distance to its nearest neighbor, as defined in this figure.

Previous studies of the statistical effects on crack arrays [18, 19] investigated the laminated composites and the fragmentation of fibers embedded in a matrix. In these studies, an exclusion zone extending either side of a pre-existing crack was derived from a shear-lag analysis. A characteristic feature of a shear-lag analysis for fracture is that once a pair of neighboring cracks are close enough to interact, it is impossible to introduce a third crack between them. Therefore, within the exclusion zone a new crack cannot form, no matter how high the applied strain on the system is. Moreover, this exclusion distance increases with increased applied strain. Conversely, if interfacial slip does not occur, the exclusion distance decreases with applied strain, so that the strain can always be increased to a level at which it is possible to introduce a third crack between two neighboring cracks. This latter type of exclusion distance is the one used in our analysis.

2.3.5 Monte Carlo Simulation

Monte Carlo simulation programs were written for simulating the cracking of a specimen of length L under an applied strain of ϵ_o. The specimen can be with or without geometrical features that act as crack initiation locations. These artificial flaws are an array of elliptical

holes spaced at S_o, with a minor radius, b, that was aligned with the flat edge, and a major radius of a. During the simulation, several tasks were performed. First, the sizes and locations of defects were generated. The flaw sizes were from the Gaussian distribution discussed above. The defects were seeded with a density of ρ, and uniformly distributed along L. When artificial defects are present, we made an assumption that the projection of flaws on the flat edge followed the same distribution. The assumption was valid when ρ was selected to be sufficient that the final crack pattern was independent from the intrinsic flaw spacing. Next, the local strain was calculated for each defect based on their locations as we discussed in the previous section. Then, the distance of each defect to its nearest longer neighbor was determined by comparing the height from the flaw tips to the flat edge. This neighbor can be either an intrinsic flaw or an artificial flaw. For the artificial flaws, the height was from each point on the surface of the features to the flat edge, which varies with the position. This distance and the flaw sizes were then used in Eqns 2.8 and 2.9 to compute the energy-release rates of each flaw. The final step was to compare the lowest of these two values to the toughness of the film, to determine whether the crack would propagate or not. It should be noted that not every crack that could have propagated from the geometrical features can channel. This is because the local strain decreases to the remote applied strain away from the geometrical features. Another remote energy-release rate was calculated for this group of cracks that can propagate from the elliptical structures using the same set of distance to the nearest longer neighbor and the applied strain. This remote energy-release rate was compared with the toughness of the film to determine the channeling cracks. The resultant crack spacing was then determined from all the flaws that were deemed to have channeled.

2.3.6 Crack arrays without geometrical features

The first set of results are presented for a geometry with no artificial features and subjected to a uniform strain of ϵ_o. Figure 2.15 shows how the cumulative distribution function for the crack spacing varies with strain for the limiting case of a relatively high density of large intrinsic flaws, with $\mu/h \to \infty$ and $\rho h \to \infty$. This is the appropriate condition for making comparisons to LEFM results for characteristic spacings. The average crack spacing decreases with increased strain. Take the case with the normalized applied strain $\varepsilon(E_f h/\Gamma_f)^{1/2} = 0.9$ as an example, the mean value of spacing, S/h is about 11.12, with a standard deviation of 4.31. The variation is considerable and the crack pattern is relatively random. The average spacing for this flaw population is shown as a function of applied

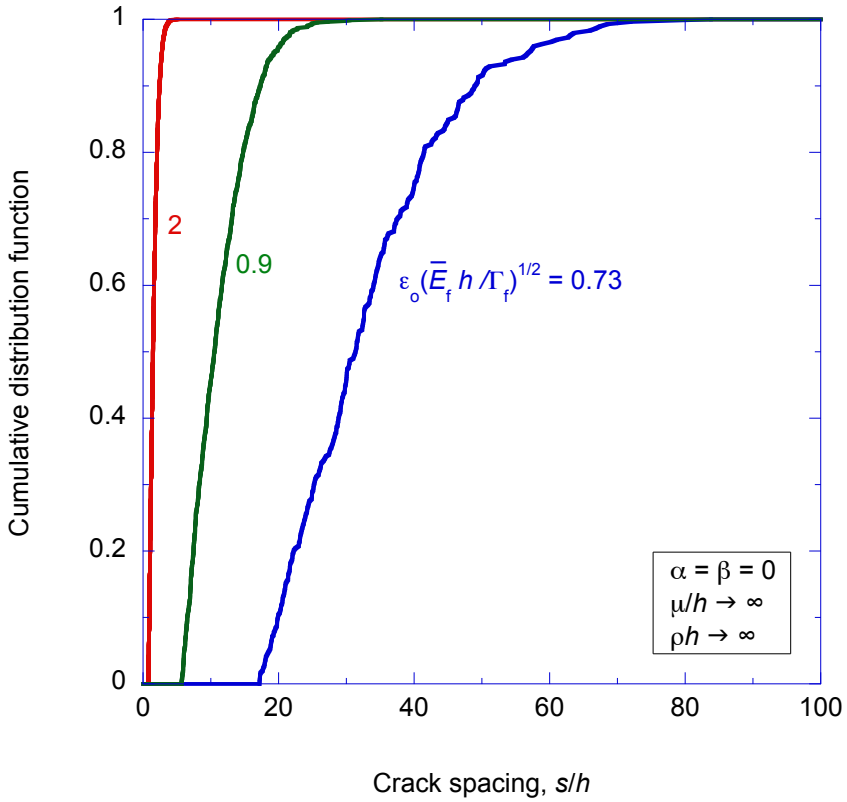

Figure 2.15: A plot showing cumulative distribution functions of the natural crack spacing in a structure with no geometrical features at different strains, for the limiting case of a very dense and long flaw population.

strain in Fig. 2.16 (solid line). Consistent with the results for the characteristic spacing from LEFM solutions, the cracks first form at a normalized strain of $\epsilon_o\sqrt{\bar{E}_f h/\Gamma_f} = 0.71$, and the crack spacing decreases with increases in applied strain. It should be emphasized that this change in spacing occurs even though the flaws are long enough for there to be no effect of size on strength. This provides a contrast to crack-spacing models based on Weibull statistics which inherently assume a locally varying coating strength dependent on the flaw size. Away from the threshold strain, the mean spacing for the statistical distribution assumed in this paper is approximately given by

$$s_{av}/h \propto \left(\epsilon_o\sqrt{\bar{E}_f h/\Gamma_f}\right)^{-2.36}. \tag{2.12}$$

This relationship appears to be valid only for relatively dense crack arrays, which may be beyond the range of practical interest for many systems. Over a more practical range, the crack spacing is given by the transition between this relationship and the threshold. It

should also be noticed that this is a steeper relationship than the inverse linear forms that result from analyses based either on the minimum spacing that just prevents an intermediate crack [25] or on a consideration of equilibrium [24, 26]. It is expected that this relationship may be sensitive to the form of the assumed flaw population, through how the distribution controls the distance to nearest longer neighbors, but this detail of the problem has not been explored.

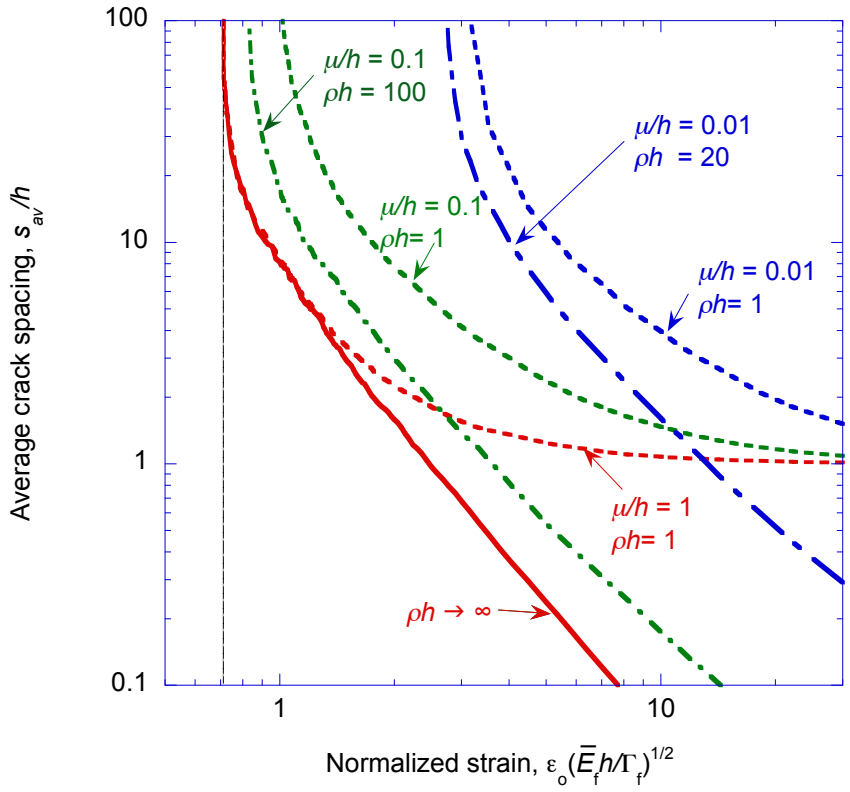

Figure 2.16: A plot showing the relationship between the mean crack spacing and the applied strain for a structure with no artificial features as a function of the flaw population (described by different values of the density and characteristic flaw size)

For systems with intrinsic flaw distribution severely skewed to the right, such as the cases with $\mu/h = 0.1$ and $\mu/h = 0.01$ in Fig. 2.16, the statistics of their size become important. The effects of flaw density and length, and of strain and toughness on the average spacing of the array are also shown in the plots of Fig. 2.16. The details of this plot will vary with different forms of the flaw distribution and on the material properties; but the general mechanics concepts will apply. While the onset of channeling always occurs at a normalized strain of 0.71 for a homogeneous system, a limited number of long flaws in-

creases the spacing for a given level of strain. The asymptotic spacing at large strains that is shown for some flaw populations is simply a consequence of an assumption that there is a finite set of flaws that can generate channel cracks.

2.3.7 The effect of geometrical features on crack arrays

The second set of results shows the effect on crack arrays of geometrical features consisting of periodic elliptical cut-outs spaced at S_o along the edge of the specimen. Each elliptical hole is assumed to have a minor radius, b, aligned with the flat edge, and a major radius of a. To simplify the process of seeding flaws in the analysis, it was assumed that the density, ρ, is given in terms of the projected length along the flat edge, rather than the actual length of the surface. The flaws were assumed to be perpendicular to the straight edge. As shown in Fig. 2.14, the distance used to calculate the energy-release rate was the distance from the tip of each flaw to the nearest intersection with either a flaw or the surface of an ellipse. The Inglis solution for an ellipse [36] as in equations 2.10 was used to calculate the local strain from which the energy-release rates for a flaw along the surface of a cut-out could be calculated. However, an additional consideration in this problem was to determine whether such a crack could continue channeling once it left the stress concentration at the tip of the ellipse. This was done by a second step in which the energy-release rate for any flaw along the surface of an ellipse that had been determined to meet the conditions of growth was recalculated with the assumption that it had reached a steady-state length but was out of the stress-concentration region. If a crack didn't meet this second growth condition, it was assumed to have propagated only a little bit from the geometrical feature, and not to have channeled across the specimen. It was, therefore, not counted as forming the crack array. (However, it was possible for these cracks to channel subsequently at higher level of applied strains.)

Cumulative distribution functions for a structure with a dense population of relatively large flaws are shown in Fig. 2.17 to 2.19. The plots are with different feature separations and aspect ratios. Figure 2.17 and 2.18 are with the same small separation of the geometrical features, $S_o/h = 10$, and different aspect ratio. It was shown that small feature separation allows a relatively wide strain range for the second regime. It should be noted from a comparison of the two plots that the effect of the aspect ratio is not particularly significant. A more detailed statistical analysis of this effect can be found in the next section.

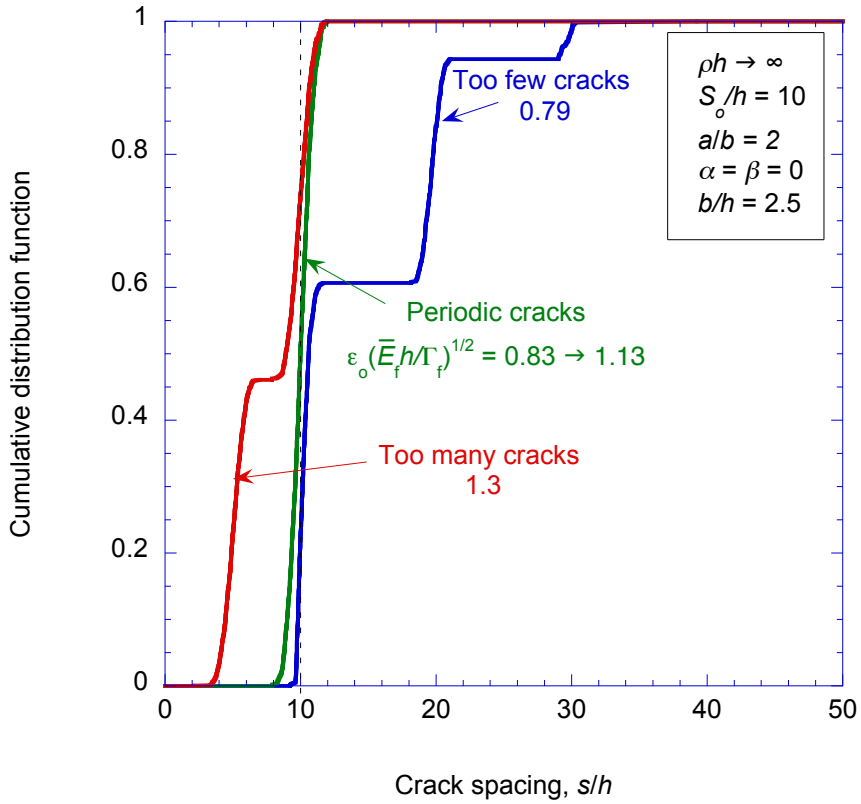

Figure 2.17: A plot showing the three regimes corresponding to Fig. 4 for systems with a sufficient density of large intrinsic defects. These plots show the effect of changing the spacing, S_o/h, and aspect ratio, a/b, of the geometrical features. $S_o/h = 10$ and $a/b = 2$.

When a big separation of the geometrical features is used, as shown in Fig. 2.19, the onset of the second regime occurs just above the critical strain for a singe crack to channel across the specimen. A very narrow strain range is allowed for the second regime. In practice, the applied strain needs to be tailored carefully to fit in this narrow range. This is again consistent with Fig. 2.7.

In conclusion, there are three points to be observed in these plots. First, consistent with the fracture-mechanics calculations of Section 2, there are three regimes of crack arrays. (i) At low strains, relatively few cracks channel across the system, and not every geometrical features initiates a crack. (ii) At intermediate strains, the distribution has a sharp and single edge corresponding to the spacing of the geometrical features. The range of strains over which this single mode of crack spacings can be obtained is very sensitive to the chosen value of S_o, becoming very restricted at large values of S_o for homogeneous systems. Conversely, the results are not very sensitive to the aspect ratio of the geometrical

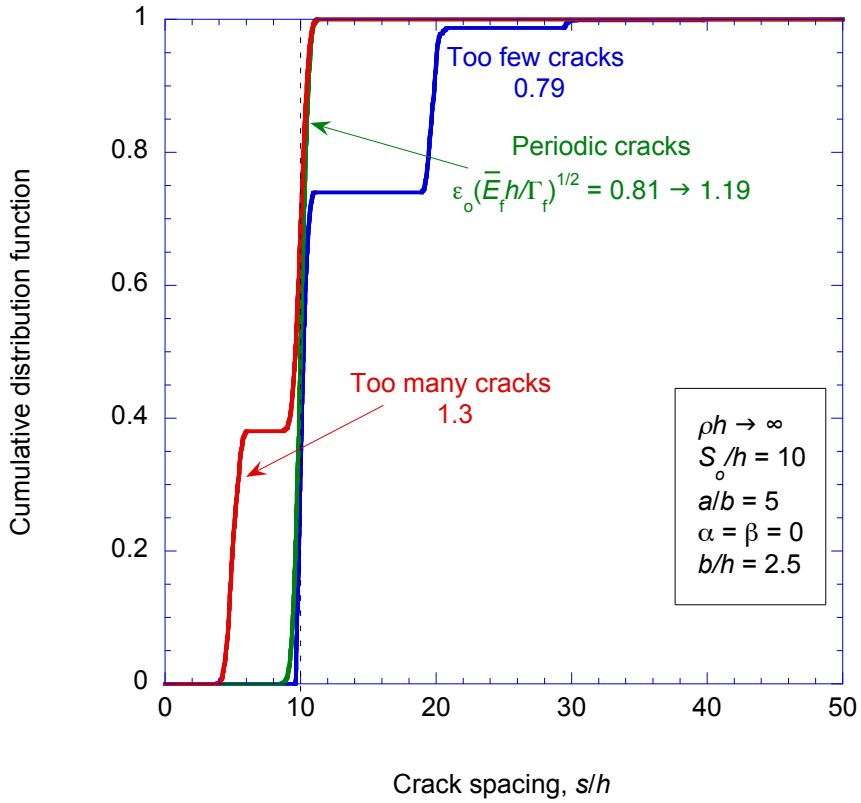

Figure 2.18: A plot showing the three regimes corresponding to Fig. 4 for systems with a sufficient density of large intrinsic defects. These plots show the effect of changing the spacing, S_o/h, and aspect ratio, a/b, of the geometrical features. $S_o/h = 10$ and $a/b = 5$.

features. (iii) At high strains, a significant number of cracks can form between the geometrical features, resulting in a non-uniform distribution again. As discussed earlier, these results are all consistent with the observations of Kim *et al.* [7] for an oxidized PDMS system, which supports the notion that this system was one with relatively large intrinsic flaws.

Figure 2.20 and 2.21 present some cumulative distribution functions for a structure with very small intrinsic flaws. A key feature to be noticed from these plots is that the strains required to ensure the initiation of a crack from every geometrical feature are greater than the strains required to channel cracks from long flaws between the geometrical features. So, the formation of uniform arrays in these systems relies on the absence of any significant flaws between the geometrical features. Since it relies on controlling the statistics of the flaw population, the approach can be considered to be rather unstable and unintended damage can trigger much finer arrays than intended. Sharper geometrical features lower the critical strains required to form periodic arrays, and, at a given strain, a uniform array

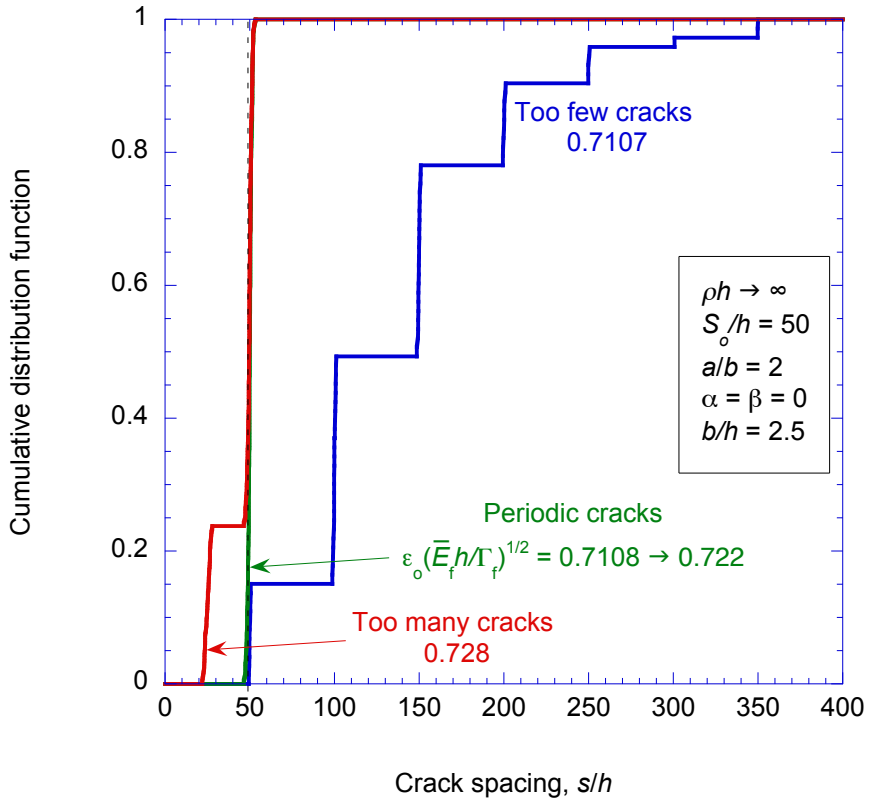

Figure 2.19: A plot showing the three regimes corresponding to Fig. 4 for systems with a sufficient density of large intrinsic defects. These plots show the effect of changing the spacing, S_o/h, and aspect ratio, a/b, of the geometrical features. $S_o/h = 50$ and $a/b = 2$.

is more likely to be formed with sharper features. Both of these conclusions, the sensitivity of array formation to the aspect ratio of the features, and the triggering of uncontrolled arrays by unintended damage, are consistent with the experimental observations presented by Nam *et al.* [4].

In Fig. 2.20 , the feature separation or the desired crack spacing is $S_o/h = 10$. The onset strain of the second regime is $\epsilon_o(\bar{E}_f h/\Gamma_f)^{1/2} = 0.9$ with sharper features ($a/b = 5$), and $\epsilon_o(\bar{E}_f h/\Gamma_f)^{1/2} = 1.8$ with blunt features ($a/b = 5$). Recall that with longer flaws, the onset strain is 0.83 and 0.81respectively.The short defects results in the requirement of a relatively high strain to get a uniform pattern. This strain is sensitive to the aspect ratio, and at low aspect ratios the required strain can be much larger than the upper-bound strain to create uniform arrays when the flaws are very long. This makes for much more unstable crack arrays, since any single relatively long flaws between the geometrical features could initiate a channel crack and break the periodicity. Sharper aspect ratios for the geometrical

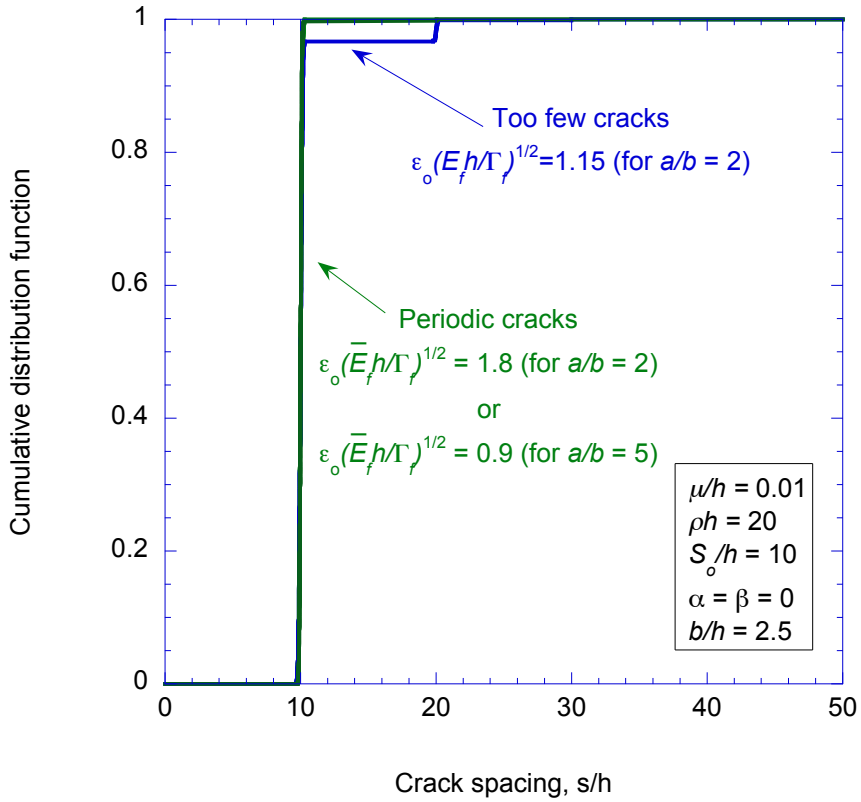

Figure 2.20: Plots showing the effects of the aspect ratio, a/b and spacing S_o/h of geometrical features on the cumulative distribution of the resultant crack arrays. The feature separation is $S_o/h = 10$. Two aspect ratios, $a/b = 2$ and 5 were used.

features lower the strain required to generate uniform flaws. In the limiting case of very sharp features, the critical strains would be reduced to the level of those in Figure 14. Plots with a larger spacing of $S_o/h = 50$ are shown in Fig.2.21. Similar to the cases with large flaws, uniform cracking occurs at lower strains.

The strategy for forming periodic patterns when there is a sufficient density of relatively large flaws is robust against damage and is not very sensitive to the nature of the geometrical features, but may require a careful matching of the strain to the desired spacing, depending on the modulus-mismatch ratio. The strategy of relying on the intrinsic flaws being very small is sensitive to the aspect ratio of the features, but may not be so sensitive to the strain. However, the strategy is vulnerable to unintended damage. A lack of strain sensitivity is useful in that it allows a range of crack spacings to be generated on a single specimen. This versatility can be obtained either by keeping the density of long flaws low, or by ensuring that the film has a much higher modulus than the substrate.

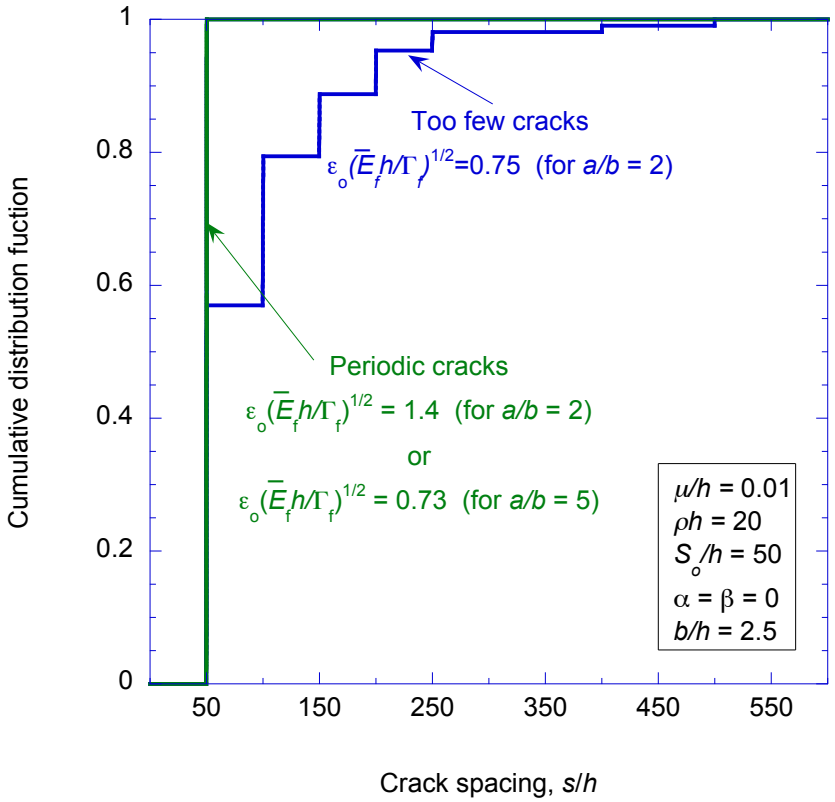

Figure 2.21: Plots showing the effects of the aspect ratio, a/b and spacing S_o/h of geometrical features on the cumulative distribution of the resultant crack arrays. The crack spacing is $S_o/h = 50$. Two aspect ratios, $a/b = 2$ and 5 were used.

2.3.8 Analysis of simulation data

The data that we will analyze are the results from 10 simulations for the systems with sufficient density of large flaws with and without geometrical features. The corresponding plots are the green line with $\rho h = \infty$ in Fig. 2.15 showing the distribution of crack spacing, and Fig. 2.17 to 2.19 . The specimen has a length of $L/h = 10^3$. The length was chosen to be long enough so that it would not affect the simulation results. This type of system with sufficient density of large flaws is comparable to materials such as oxidized PDMS. We have shown that for this type of systems, the sharpness of the geometrical feature is not critical, however, the matching of feature separation with material properties and applied strain needs to be precise. The spacing of the geometrical features was selected to be $S_o/h = 50$ and $S_o/h = 10$, to represent relatively large spacings and small spacings. Two

values were selected for the aspect ratio of the ellipses, $a/b = 2$ and 5. In the following analysis, we find that the aspect ratio doesn't have a significant effect on the crack pattern. The simulation was performed for both geometries with and without elliptical structures as crack initiation locations. We will assess the effectiveness of the crack initiating structures.

Table 2.1: Individual and aggregate results for 10 individual simulations for a uniform geometry

$\mu/h = 1$ $\rho h = \infty$ $L/h = 10^3$ $m = 10$		
i	$\bar{S}_i/h$	SD
1	10.87	4.06
2	10.87	3.85
3	11.63	5.05
4	11.36	4.71
5	10.87	3.62
6	11.11	4.13
7	11.24	3.81
8	10.99	4.04
9	10.53	4.64
10	11.90	5.04
Aggregate	11.12	4.31

Individual and aggregate results of crack spacing for a uniform geometry and geometries with elliptical structures as crack initiation location can be found in Table 2.1 to 2.3. These results are from a specific applied strain of $\epsilon(\bar{E}_f h/\Gamma_f)^{1/2} = 0.9$, which is within Regime 2 when the crack control mechanism is fully functional. From Table 2.1, we can see that the normalized average spacing is $S/h = 11.12$, with a standard deviation of 4.31. The variance of crack spacings is significant, and the crack array is considered non-uniform. With the elliptical structures as crack initiation locations, we can significantly reduce the variance. Two groups of results with different aspect ratio of the geometrical features are presented in Table 2.2 and 2.3. The aspect ratio was $a/b = 2$ and $a/b = 5$ respectively. By observing results, we can see that the average crack spacing is well defined by the geometrical features, $\bar{S}/h = S_o/h = 10$. This indicates that the choice of feature separation was proper for this specific level of applied strain. The aggregated standard deviation reduced significantly to 0.74 and 0.44. It appeared that with greater aspect ratio of geometrical features, the variance is further decreased. The significance of the geometrical features in reducing the variance of the crack spacing will be tested by one-way analysis of variance (ANOVA). The significance of the sharpness of the features will also be tested by ANOVA.

Table 2.2: Individual and aggregate results for 10 individual simulations for a geometry with an array of elliptical structures as crack initiation locations,relatively blunt tips

$\mu/h = 1$ $\rho h = \infty$ $L/h = 10^3$ $S_o/h = 10$ $m = 10$ $a/b = 2$		
i	$\bar{S}_i/h$	SD
1	10	0.67
2	10	0.77
3	10	0.78
4	10	0.67
5	10	0.74
6	10	0.82
7	10	0.77
8	10	0.74
9	10	0.75
10	10	0.75
Aggregate	10	0.74

Table 2.3: Individual and aggregate results for 10 individual simulations for a geometry with an array of elliptical structures as crack initiation locations,relatively sharp tips

$\mu/h = 1$ $\rho h = \infty$ $L/h = 10^3$ $S_o/h = 10$ $m = 10$ $a/b = 5$		
i	$\bar{S}_i/h$	SD
1	10	0.42
2	10	0.44
3	10	0.45
4	10	0.43
5	10	0.52
6	10	0.47
7	10	0.42
8	10	0.45
9	10	0.39
10	10	0.42
Aggregate	10	0.44

First, the strip plots of the three groups of results are shown in Fig. 2.22. We can see that the variance is different between the three groups. There are no outliers or skewness in the data. ANOVA is performed for the three groups of data. From the F-Statistics, we found that the p-value was very small, $< 2.2 \times 10^{-16}$, and we can conclude that there is some difference between the groups. Therefore, we can make the conclusion that the geometrical features can significantly reduce the variance of the crack spacings.

We then investigated whether the aspect ratio of the geometrical features have a significant effect on reducing the variance of the crack spacing. A similar F-statistics was performed for the two groups of data which were from the simulation of systems with elliptical structures as crack initiation locations. The aspect ratio of the elliptical structures was 2 and 5 respectively. We found that the p-value was 1, which indicated that there was no significant difference between the two groups of data. We therefore made the conclusion that for systems with sufficient density of long intrinsic defects, the aspect ratio of geometrical features is not significant in reducing the variance of the crack spacings. As long as the matching between the feature separation, material properties and the applied strain was tailored, the crack spacing can be well defined by the feature separations.

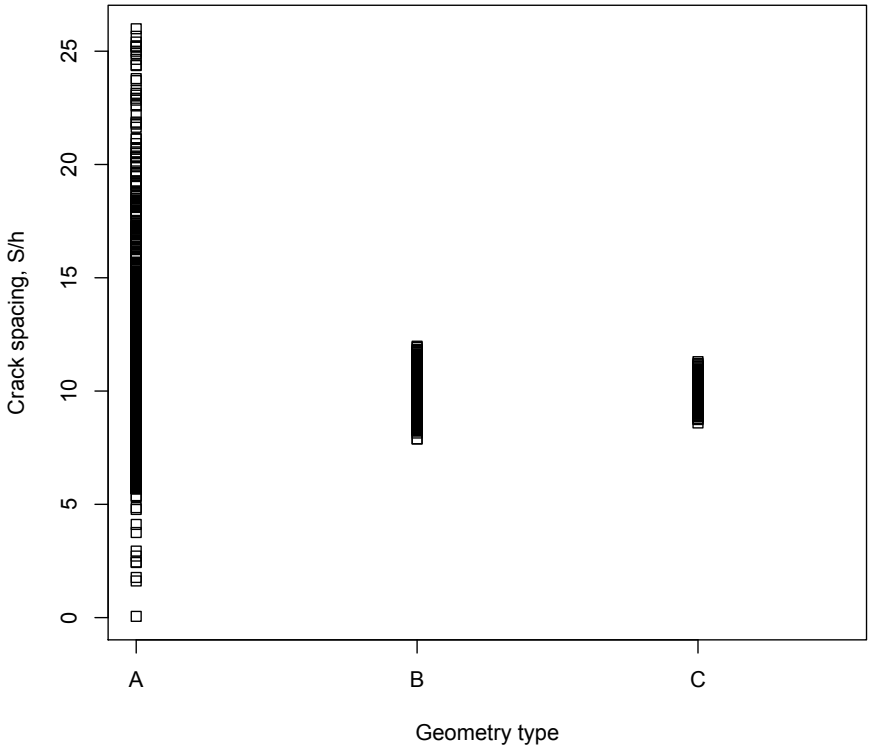

Figure 2.22: Strip plots of the simulation results of the crack spacing with different geometries. Geometry types are designated by: type A for a uniform geometry in the absence of any geometrical features as crack initiation locations; type B for a geometry with an array of elliptical structures with aspect ratio of 2 and spaced at $S_o/h = 10$; type C for a geometry with an array of elliptical structures with aspect ratio of 5 and spaced at $S_o/h = 10$.

2.4 Uniform fully-reversible micro-scale fluidic channel

As discussed in sections 2.2.1 and 2.2.2, cracks may be contained in the film or penetrate into the substrate. This is determined by the modulus mismatch between the film and substrate material. When the modulus of the film and substrate are equal, the cracks are confined to a surface layer with crack depth equate to the film thickness, h. The cracks in this case are usually with small spacings and are of small sizes. The width of cracks is around tens of nanometers [2]. If the film has a much higher modulus than the substrate, the cracks penetrate into the substrate, resulting in deep cracks with larger spacings [3]. Although this latter type of cracks can handle a wider range of biomolecules especially in the micron-scale regime, the lack of control over crack depth limits its use. It is most desirable to independently control the crack depth and crack width. We found that hard PDMS (h-PDMS) can be used to generate cracks with defined dimensions at the micron-scale.

2.4.1 Material characterization

The Young's modulus of PDMS and h-PDMS were measured using uniaxial tensile tests. The tensile specimens were prepared by casting PDMS and h-PDMS in dog-bone shaped molds, following ASTM D638-10. MTS 858 Bionix II tensile machine was used to conduct the tensile tests. The specimens were released from the mold and clamped in wedge grips. The load was applied at a constant strain rate of 0.8%/s. The load was measured using a 250N load cell and was automatically recorded. Optical images were taken to track the displacement of markers on the sample. The strains were then determined using MetaMorph software to analyze the optical images. True stress-strain curves were used to calculate the Young's modulus of each material. An example of the resulting stress-strain curve is shown in Fig. 2.23. It should be noted that PDMS displays hyperelastic properties. The modulus of PDMS was measured to be 3.7 ± 0.3 MPa. This agrees with the results previously reported by Mills *et al.* [1]. The same approach was used to measue the modulus of h-PDMS, giving a result of 9.2 ± 0.6 MPa.

Table 2.4: Mechanical characterization of materials

	PDMS	h-PDMS
Young's modulus	3.7 ± 0.3 MPa	9.2 ± 0.6 MPa
Mode I toughness	460 ± 50J/m^2	12.9 ± 2.7J/m^2

The toughness of h-PDMS was measured using a tensile specimen with an edge crack that had been introduced by razor blade following ASTM E1820-11e2. Crack growth during the tests was monitored using a CCD camera. No sub-critical crack growth was observed, so the peak load and the original crack length were used to determine the toughness. The toughness of the h-PDMS was determined to be $12.9 \pm 2.7 \text{J/m}^2$. The toughness of PDMS was reported by Mills *et al.* to be $460 \pm 50 \text{J/m}^2$. All mechanical characterization data are summarized in Table 2.4. H-PDMS is much more brittle than PDMS, this allows a thin film of h-PDMS supported on PDMS substrate to crack under applied tensile strain. The moduli of the two materials are comparable. As discussed in sections 2.2.1 and 2.2.2, the cracks in such a system are mostly localized to the h-PDMS film layer. Hence, by controlling the thickness of the h-PDMS layer, this system should afford a greater degree of control over the depth of which cracks propagate.

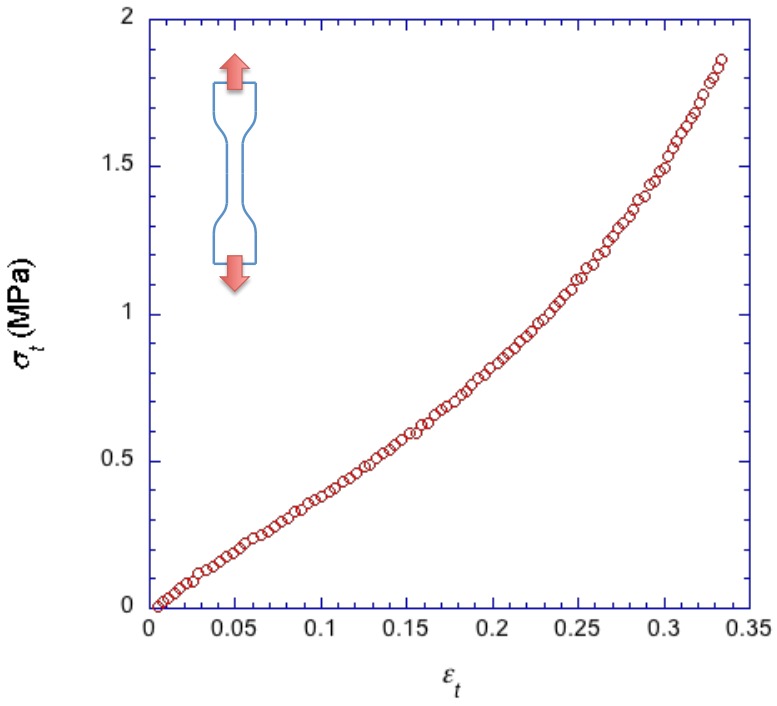

Figure 2.23: Stress-strain curve of a uniaxial tensile test for PDMS.

2.4.2 Results and Discussion

We reported the controlled cracking of thin h-PDMS film on PDMS substrate [5]. A thin film of h-PDMS of selected thickness is sandwiched between two standard PDMS layers. The multilayered structure was prepared using a sequential deposition technique. The geometrical features discussed in section 2.2 were also molded in the h-PDMS layer for crack control purposes. It was found that the cracks were only propagated from the geometrical features, with crack depth relatively stable up to an applied strain of 60%, at which the PDMS substrate failed catastrophically. The very small change in crack depth at higher strains suggest the cracks only slightly penetrate into the substrate and the crack depth has reasonably good consistency at all strain levels. The cracks were completely closed upon full release of applied strain, which suggested that no delamination at the interface occurred. The flat bottom of the crack profile suggested high levels of strain at the tip of cracks which is rooted in the hyperelastic properties of PDMS.

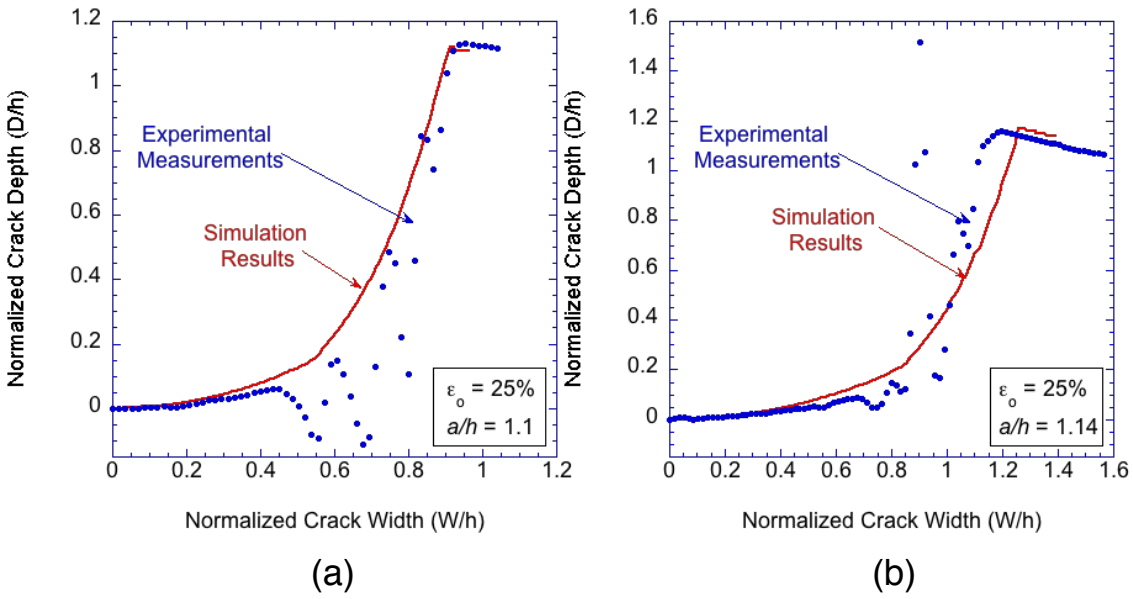

Figure 2.24: Stress-strain curve of a uniaxial tensile test for PDMS.

In order to confirm the mechanics underlying the observed crack profile, finite element analyses were conducted. The full stress-strain behavior of PDMS for large deformations of the material was used in the calculation. Given the low modulus mismatch between h-PDMS and PDMS ($E_f/E_s \approx 2.5$), and the observed experimental results, the cracks only

penetrate slightly penetrate into the substrate, with the ratio of crack depth to film thickness, a/h close to one. The simulation results confirmed that the substrate near the crack tip deforms dramatically and forms the flat bottom. The simulated penetration depth a/h was iteratively varied to most closely match the experimentally measured crack profiles. The comparison between the simulation results and experimental measurements are shown in Fig. 2.24. It was shown that $a/h = 1.1$ at 25% of applied strain and $a/h = 1.14$ at 35% applied strain. The small increase in penetration with large increase in strain is consistent with experimental observations and quantifies the close relationship between the thickness of the h-PDMS film and the depth of the generated crack.

The use of h-PDMS as the brittle layer instead of the conventional oxidized PDMS or deposited metal films provides advantages of both better defined crack depth and wider range of crack sizes. The wider range of crack sizes answers the challenges existing in defining micron-scale dimensions of cracks in bilayer material systems. Because the h-PDMS film can be prepared by spin-coating, the film thickness is better controlled compared with the oxidized PDMS. The toughness mismatch between h-PDMS and PDMS is large enough to generate stable crack arrays at relatively low strains, yet the modulus mismatch is small enough to strongly localize the cracks to the h-PDMS layer. It was reported by Mills that the modulus of oxidized PDMS is between 7 and 13 times larger than the modulus of the substrate, and that the toughness of oxidized PDMS was estimated to be approximately 60 mJ/m^2. h-PDMS is less stiff and less brittle than oxidized PDMS. This explains why the cracking behaviors are different for the two materials. It is interesting that the controlled cracking works better with the material combination of h-PDMS and PDMS. Increasing the applied strain only widens existing cracks which are propagated from the geometrical features instead of initiating more cracks. The hyperelastic deformation of substrate material is more energy favorable than initiating more cracks. This interesting interaction between the film and substrate materials suggests a broader future of controlled cracking as fabrication techniques given more new materials are discovered.

2.5 Conclusions

The stochastic nature of flaws affects the formation of crack arrays in linear-elastic systems through the fact that the energy-release rate for channeling a crack depends on its distance to nearest longer neighbors. This introduces a statistical aspect of crack lengths to the problem, even if all the flaws are long enough so that the energy-release rates are

insensitive to their lengths. This is a different effect from the more usual assumption (used in Weibull statistics, for example) that the statistics of crack lengths enter fracture problems directly through the dependence of energy-release rate on crack length. These two aspects of the effects of statistics on cracking give rise to two distinct approaches for controlling the formation of crack arrays: one relies on maintaining a sparse density of flaws, the other is more general and applies to systems with fairly extensive flaw populations.

Controlled arrays can be generated in a system with very small flaws by introducing sharp geometrical features that can trigger crack channeling from small defects at points of high stress concentrations. While there can be considerable latitude for the range of strains that can be used, this strain has to be relatively high, and the strategy is not stable against any accidental introduction of additional large defects. The control of the crack array using this strategy is very sensitive to the details of the strain enhancement. The physics behind this proposed strategy seems to be consistent with the reported observations concerning controlled crack patterns in a silicon nitride film deposited on a silicon wafer [4]. In that paper, evidence was given that the crack patterns could be controlled but the details of the stress concentrators used to trigger cracks were important. There was also evidence that the system failed occasionally, with dense random arrays being generated.

Controlled arrays can also be generated in systems with relatively large defect populations by introducing geometrical features. The role of these features is to project the tips of some flaws well beyond the others at well defined points where channeling is desired. These cracks propagate first, when the appropriate strain conditions are met. Since the features only need to project the tips of some flaws, less stringent conditions are placed on their sharpness than on the features discussed in the previous paragraph. However, the design of the system requires a tight coupling between the material properties of the system, the geometry, and the applied strain used to generate the crack arrays. A small difference in modulus between the film and substrate allows only relatively close crack spacings to be obtained reliably. A large difference in modulus mismatch, which can be accompanied by cracking of the substrate, allows a larger range of crack spacings, and a larger range of strains over which the spacings can be matched correctly.

This strategy of strain matching for both the small and large modulus mismatch is consistent with observations on the formation of controlled crack patterns on oxidized PDMS and in gold films deposited on PDMS [7]. This system has been used as the basis for fabricating tunable nano-channels used for confining DNA and chromatin [2]. It is believed that

the strategy outlined in this paper can be used to ensure uniform arrays, so that at a given strain all the channels in an array will have similar dimensions. One question that might arise is whether the cracks in an initially uniform array will close in a uniform fashion, or whether some cracks might collapse before others. In this regard, it should be noted that the appropriate toughness for healing these arrays (corresponding to a physical attraction, such as van der Waals) will be much lower than the toughness associated with crack formation. Therefore, the arrays that form are very sparse compared to the natural spacing that would correspond to the toughness appropriate for the healing process. This means that the cracks will not interact with one another until the applied strain has been relaxed to very low levels, and the closing of the nano-channels should be effectively uniform until the system is almost completely strain free. This is consistent with optical observations in these systems, and suggests that once formed, uniform crack arrays in compliant systems should provide repeated consistent opening and closing cycles if required.

CHAPTER 3

The closure of liquid-filled cracks

3.1 Introduction

Nano fluidic channels fabricated by cracking of a thin film supported on elastic substrates are used for biological applications including single DNA and chromatin analysis [1–3, 6], cell patterning [16, 38, 39], and biomimetic systems [40]. The fabrication of this type of nanochannels is fairly easy and cost-effective, where an array of parallel channels are created by applying tension to an layered structure. The channel can narrow upon subsequent relaxation of the applied tension. The reliability of the fabrication technique is greatly enhanced by recent research of controlled cracking using microstructures to precisely initiate and propagate cracks at desired locations [7, 41], enabling parallel analysis of large amount of samples in identical conditions. Narrowing the channels provide finer confinements accompanied by nano-scale squeezing flow which are especially favorable for DNA and chromatin linearization [2]. Characterization of the narrowing channels is therefore desired to better understand DNA and chromatin behaviors in the channels and to develop optimal channel operation parameters.

Because the channels are nano-scale three-dimensional structures beneath the surface, characterization is difficult. Scanning electron microscopy (SEM) and laser confocal microscopy were used in reference to measure surface cracks [1, 2, 7]. The results provide some reference for the shape and size of tunneling cracks but fail to reflect the real profile of liquid-filled nanochannels. An electrical-impedance method was used to approximate the average cross-sectional area of tunneling cracks. The accuracy of this method is greatly affected by the choice of model and ion depletion during the experiment [2, 3]. Cheng *et al.* used photoactivated localization microscopy (PALM) to perform super-resolution imaging of nanochannels [42]. While it provides higher-resolution images, the method is limited to two-dimensional and cannot track the time-dependent narrowing process, because it takes

average of signals over time. Therefore, we need to utilize computational methods to understand the time-dependent narrowing of asymmetric nanochannels in thick elastic substrate and filled with viscous substances.

The nanochannels of our interest have thick channel walls as they are embedded in thick elastic substrates with channel spacings between one to two orders of magnitude bigger than channel widths. [2, 7, 42] Fluid flow is driven by the remote compression and the deformation of the elastic channel wall. Literature of flows driven by the deformation of an elastic channel or tube can be found in the transportation of bio-fluids [43–46], and membrane-activated microfluidic pumps [47–50]. The existing analyses place more focus on the flow while the motion of the channel wall is always prescribed. In our previous analyses, we assumed uniform prescribed wall displacements and estimated the flow in narrowing cylinders to be of an elongational shear type [2]. However, it was observed by Cheng *et al.* [42] in experiments that the channels narrow first near the exit. The wall motion actually relies on the interaction between the fluid flow and the thick elastic substrate. This important aspect is neglected when deformation is prescribed. Another group of related research examine collapsible tube in artery stenosis [51–53], where the flexible tube is connected to rigid tubes at the ends and is usually modeled as a compliant thin-shell. In our problem, the wall movement is determined by the interaction between the stress field in the thick channel wall and the fluid flow. For this reason, assuming small-scale deformation, we can use theory of elasticity to solve the stress field in the channel wall and displacements at the interface between the channel and fluid.

The structure of this chapter consists of three parts. First, the channel flow under uniform prescribed radial displacements is discussed. The second part contains analyses for a thick-walled axisymmetric tube that is filled with liquid and subjected to external compression. We study the non-uniform narrowing of the tube initiated from the exit of the tube and proceeding towards the center of the tube. Optimal operation parameters to avoid partial collapses are suggested, which agree with the empirical approaches suggested by Matsuoka *et al.* [2] In the third part of this chapter we discussed how the shape and dimensions of an elliptical channel in thick substrates evolve for both cases of channel opening and channel narrowing.

3.2 Flow of a contracting liquid cylinder

As the channel narrows, the liquid is squeezed out of the channel generating a flow. A simplified model of the squeeze flow includes a slender axisymmetric liquid cylinder of fluid subjected to uniformly decreasing radius. Here we use the asymptotic procedures reported by Schultz [54] to calculate the flow rate. In the calculation, the cylinder is assumed to be of length L, outer radius A, and has a viscosity μ and density ρ. The outer radius A decreases with time, T. Depending on the details of the method to narrow the cylinder, different formulas can be used to describe the radius. In the experiment, the channels are fabricated by tunneling cracking of a thin film sandwiched between thick elastomeric substrates upon remotely applied strain as described in the previous sectors. The channels are buried in thick elastic substrate and can be closed by relaxation of the applied strain. Two different approaches were used to relax the applied strain resulting in different degree of DNA linearization. One is the stepwise quick relaxation, where the strain is released in multiple steps from 10% to 7%, 7% to 5%, 5% to 3% and 3% to 1%. We approximate this type of closing with an outer radius decreasing linearly with time. Another is the completely collapsing the nanochannel in a single step with the outer radius of the liquid better approximated with an exponential equation. Both methods are discussed below. Although the details of the flow vary, they are in general of the same type – elongational shear flow. We believe this flow facilitates the linearization of DNA and may have future applications in manipulating macromolecules in nanochannels.

3.2.1 Flow of a linearly contracting liquid cylinder

We first consider the case of quick multi-step closing used in the experiment. The channels are closed by partial relaxation of the strain and is held at the lower strain level for about 0.5 second. We approximate this closing condition with the radius decreasing at a fixed rate K which is independent of time T, so that

$$A = A_i - KT, \tag{3.1}$$

where A_i is the initial value at $T = 0$. This results in a flow with an axial velocity W and a radial velocity U, and also leads to gradients in the pressure P. The system is isothermal and gravity is ignored. The liquid is Newtonian and all fluid properties are constant. A cylindrical coordinate system (R, Θ, Z) is employed.

The axial and radial coordinates can be scaled by L and A_i respectively, so that $z =$

Z/L, and $r = R/A_i$. The nondimensional radial and axial Velocities are $u = U/K$ and $w = WA_i/KL$, respectively. Other nondimensional groups include the nondimensional time $t = TK/A_i$, the nondimensional pressure $p = P{A_i}^3/\mu KL^2$, and the nondimensional outer radius $a = A/A_i = 1 - t$. Two additional parameters that enter the calculations are the scaling parameter $\varepsilon = A_i/L$, and the Reynolds number, $\mathrm{Re} = KA_i\rho/\mu$.

Using this nondimensionalizing scheme, the continuity and Navier-Stokes equations can be expressed as:

$$\frac{\partial u}{\partial r} + \frac{1}{r}u + \frac{\partial w}{\partial z} = 0, \tag{3.2}$$

$$\varepsilon^2 \mathrm{Re}\left(\frac{\partial u}{\partial t} + u\frac{\partial u}{\partial r} + w\frac{\partial u}{\partial z}\right) = -\frac{\partial p}{\partial r} + \varepsilon^2\left(\frac{1}{r}\frac{\partial u}{\partial r} - \frac{u}{r^2} + \frac{\partial^2 u}{\partial r^2}\right) + \varepsilon^4\frac{\partial^2 u}{\partial z^2}, \tag{3.3}$$

$$\mathrm{Re}\left(\frac{\partial w}{\partial t} + \frac{\partial w}{\partial r} + w\frac{\partial w}{\partial z}\right) = -\frac{\partial p}{\partial z} + \frac{1}{r}\frac{\partial w}{\partial r} + \frac{\partial^2 w}{\partial r^2} + \varepsilon^2\frac{\partial^2 w}{\partial z^2}. \tag{3.4}$$

The boundary conditions for the problem of interest assuming symmetry about $z = 0$, are:

$$\begin{aligned} w &= 0 \quad && \text{on} \quad && r = a, \\ u &= -1 \quad && \text{on} \quad && r = a, \\ |u|, |w| &< \infty \quad && \text{on} \quad && r = 0, \\ \partial u/\partial z &= 0 \quad && \text{on} \quad && z = 0. \end{aligned} \tag{3.5}$$

Since we assumed $\varepsilon \ll 1$, we can follow the perturbation method reported by Schultz *et al.* [54] and write for all the dependent variables, ϕ,

$$\phi = \phi_o + \varepsilon^2\frac{\partial^2\phi}{\partial a^2} + \varepsilon^4\frac{\partial^4\phi}{\partial a^4} + O(\varepsilon^6). \tag{3.6}$$

Noting that in this case the scaling parameter ε only appears in even powers in the governing equations.

The inertial forces are assumed to be negligible, so that $\mathrm{Re} = 0$. We then substitute Eq.3.6 into the governing equations. Thus, to zero order in ε, equations 3.2 to 3.4 and boundary conditions 3.5 become:

$$\frac{\partial u_o}{\partial r} + \frac{1}{r}u_o + \frac{\partial w_o}{\partial z} = 0, \tag{3.7}$$

$$\frac{\partial p_o}{\partial r} = 0, \tag{3.8}$$

$$\frac{\partial p_o}{\partial z} + \frac{1}{r}\frac{\partial w_o}{\partial r} + \frac{\partial^2 w_0}{\partial r^2} = 0. \tag{3.9}$$

$$\begin{aligned} &w_o = 0 && \text{on} && r = a, \\ &u_o = -1 && \text{on} && r = a, \\ &|u_o|, |w_o| < \infty && \text{on} && r = 0, \\ &\partial u/\partial z = 0 && \text{on} && z = 0. \end{aligned} \tag{3.10}$$

Solving the partial differential equations Eq. 3.7to 3.9 with the boundary conditions 3.10, it can be shown that the solutions for zero order in ε are:

$$u_o = -a^{-3}\left(2a^2 r - r^3\right), \tag{3.11}$$

$$w_o = 4za^{-3}\left(a^2 - r^2\right). \tag{3.12}$$

We then applied the same procedures for the higher orders of ε, and found that the solutions for there were all equal to zero, so the zero-order solution is the full solution. Therefore, we can state that the flow is an elongational shear flow, and has both radial and axial velocities. From Eq. 3.12, we can see that at each axial location, the axial component of the flow has a parabolic profile. An example of the streamline of the flow is shown in Fig. 3.1

The shear rate of the flow can be expressed as $\dot{\gamma} = \partial u/\partial z + \partial w/\partial r$. Expressing the shear rate with the dimensional groups gives $|\dot{\gamma}| = 8KZR/A^3$. Averaging the shear rate along the length and the radius, the average shear rate can be shown to be given by $|\dot{\gamma}_{average}| = 2KL/A^2$. Along the centreline of the cylinder ($R = 0$), the flow is purely elongational, with an axial velocity of $w_o = 4z/a$, and a strain rate of $\dot{\epsilon} = \partial w_o/\partial z$. Expression of the strain rate with the dimensional groups is given by $\dot{\epsilon} = 4K/A$.

Although being an over simplified model of the flow in a narrowing channel, it provide a good connection to many of the experimental observations. First, we examine the shear rate and the strain rate of the flow because they affect the linearization of macromolecules in the flow. To estimate the strain rates of the flow in a narrowing channel, the dimensions

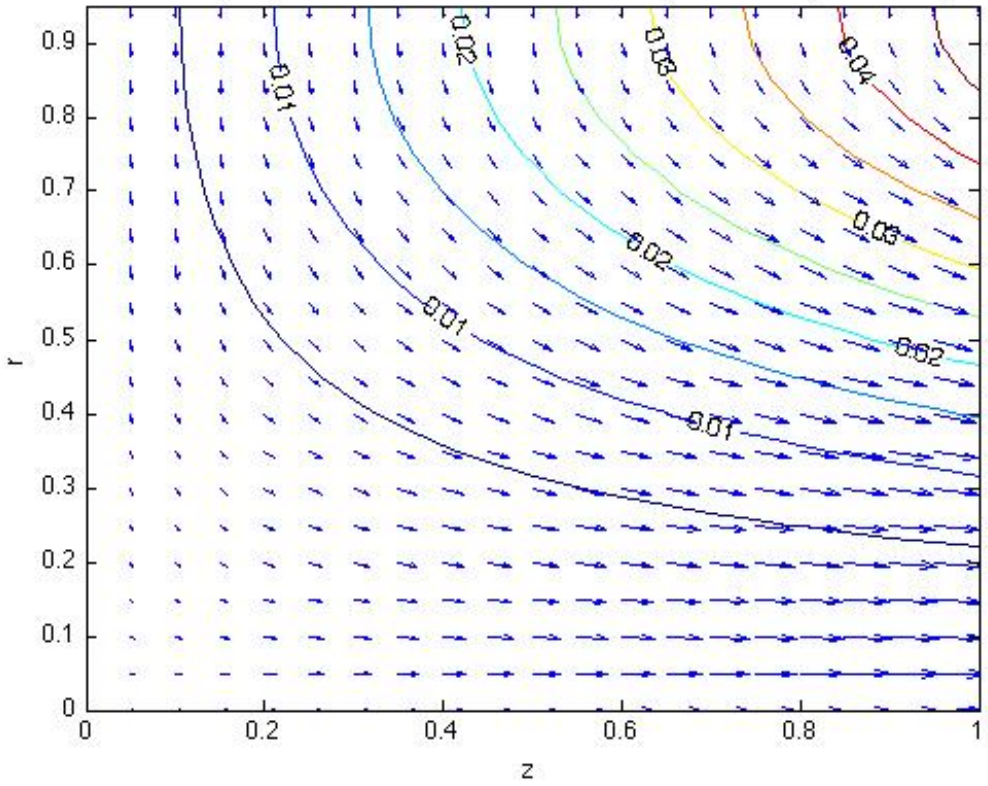

Figure 3.1: An example of streamline of the flow in a cylinder with uniformly decreasing radius.

of the channel were calculated from electrical impedance measurements taken across the nanochannel array [1]. The cross-sectional area was found at different strain levels. The equivalent radius of the channels and the strain rates are listed in Table 3.1. When the squeeze flow is used to linearize DNA, the effect is evaluated by two parameters derived from the strain rates. One is the accumulated strain (Hencky strain) which is define by multiplying the strain rate by the residency time of the molecule in the flow. The other is the Weissenberg number (Wi) which is defined as the product of the average shear rate and the DNA relaxation time [2]. The Hencky strain and Weissenberg number at different levels of strain are also listed in Table 3.1.

We found that λ-DNAs were extended up to 97% of its contour length during multiple steps of quick closing by releasing the strain from 10% to 1%, as shown in table 3.1. The nearly full linearization of DNA was due to both the confinement provided by the small sizes of the channels of around tens of nanometers and the squeeze flow. We estimated a Henckey strain of 8 which is comparable to the strains reported by Perkins *et al.* re-

Table 3.1: Values of the equivalent radius of nanochannels, strain rate, shear rate, Weissenberg number and Hencky strain during each closing conditions

Strain	A (nm)	$\dot{\varepsilon}$ (s^{-1})	$\dot{\gamma}$ (s^{-1})	Wi	Hencky Strain
10%	68.7	NA	NA	NA	NA
10% to 7%	38.5	6.26	1.22E4	4.37E4	3.13
7% to 5%	22.5	5.71	1.91E4	2.88E4	5.99
5% to 3%	17.9	2.02	8.45E3	9.03E3	7.00
3% to 1%	14.8	1.67	8.42E3	6.78E3	7.83

quired to achieve 80% extension of λ-DNA with a purely elongational flow [55]. The strain rates are strongly dependent on the details of the relaxation procedure of the applied tensile strain. Rapid relaxation of the applied tensile strain results in higher rates of the flow, which are desirable. It was also found that relaxation of the applied strain in a series of rapid increments with a brief hold between them gives higher yields of linearized DNA than completely collapsing the nanochannel in a single step. The nanoconfinement combined with the high rates of elongational shear flows enabled the DNA linearization to nearly full extent. We also estimated the fluid velocities to be around 300μm/s in the multistep quick narrowing procedure. By measuring the velocity of quantum dots in channel during the nanoscale squeezing flow, the flow velocity was estimated to be 40μm/s. The lower speed of the quantum dots may be because of the relatively large size (diameter 20nm). It is therefore expected that the fluid flow itself should have a higher speed [2].

3.2.2 Rapid collapse of liquid cylinder

In the case of full relaxation of the applied strain in single step, the outer radius is better approximated by

$$A = A_i e^{-T/T_s}. \tag{3.13}$$

The normalization is similar to that in the previous section, with the velocity scale K replaced by A_i/T_s, such that $u = U/(A_i/T_s)$, $w = WT_s/L$, and $p = PA_i^2T_s/\mu L^2$. The nondimensional outer radius $a = e^{-t}$, and the Reynolds number, $\mathrm{Re} = A_i^2\rho/\mu T_s$.

By solving the Navier-Stokes equations with the boundary conditions, we can get that

$$u = -\left(2r + e^{2t}r^3\right), \tag{3.14}$$

$$w = 4z\left(1 - e^{2t}r^2\right). \tag{3.15}$$

We can see that the flow is very similar to that in the previous section. It is an elongational shear flow with bigger flow rates. However it is not as good when used for DNA linearization. Not only the DNAs are not extended to the same high degrees, the channels are collapsed locally leaving pockets of fluid trapped in the channel. We will discuss about the liquid entrapment in latter sections.

3.3 Axisymmetric thick-walled tube

To examine the problem of an elastic thick-walled channel with a fluid core, we first neglect the details of the channel shape and consider a more general 3D axisymmetric problem of an elastic tube with an inner radius of R_1, an outer radius of R_2, and a half length of L, where the tube length is much greater than the other two dimensions. Since the problem is symmetric about the center of the tube, half of the geometry is considered, as shown in Fig. 3.2(a). The tube is held expanded by applying a uniform traction of σ_o on the external surface as shown in Fig. 3.2(b). Cylindrical coordinates of r, θ, z are employed. The radial and hoop stresses in a thick-walled tube are described by the Lamé equations:

$$\begin{aligned} \sigma_{rr} &= C_1 + C_2/r^2 \\ \sigma_{\theta\theta} &= C_1 - C_2/r^2 \end{aligned} \tag{3.16}$$

where C_1 and C_2 are constants which can be discovered from the boundary conditions, and r is the radius at the point of interest.

The tube is made of an incompressible elastic material with a modulus of E and a Poisson's ratio of $\nu = 0.5$. The fluid is incompressible, and has a viscosity of η.

While the tube is held expanded, it is filled with fluid and a static state is reached. The fluid has a reference pressure as the ambience of P_o. Then the applied tension is unloaded incrementally to zero (Fig. 3.2(c)). During unloading, the tube tends to return to its original relaxed state, with the radii decreasing and tube length elongating. However, it is impeded by the existence of the fluid core. Considering a thin slice of the cylinders, the stresses are relaxed slowly enough that fluid flow can occur in the cross-section of the tube, and equilibrium is maintained in the fluid. A uniform hydrostatic pressure of P is built up throughout the fluid at a given cross-section. The cylinders have no net axial tension at a cross-section, and plane sections remain plane, which is referred as plane the displacement condition in the following analysis. The hydrostatic pressure of P is much greater than the reference

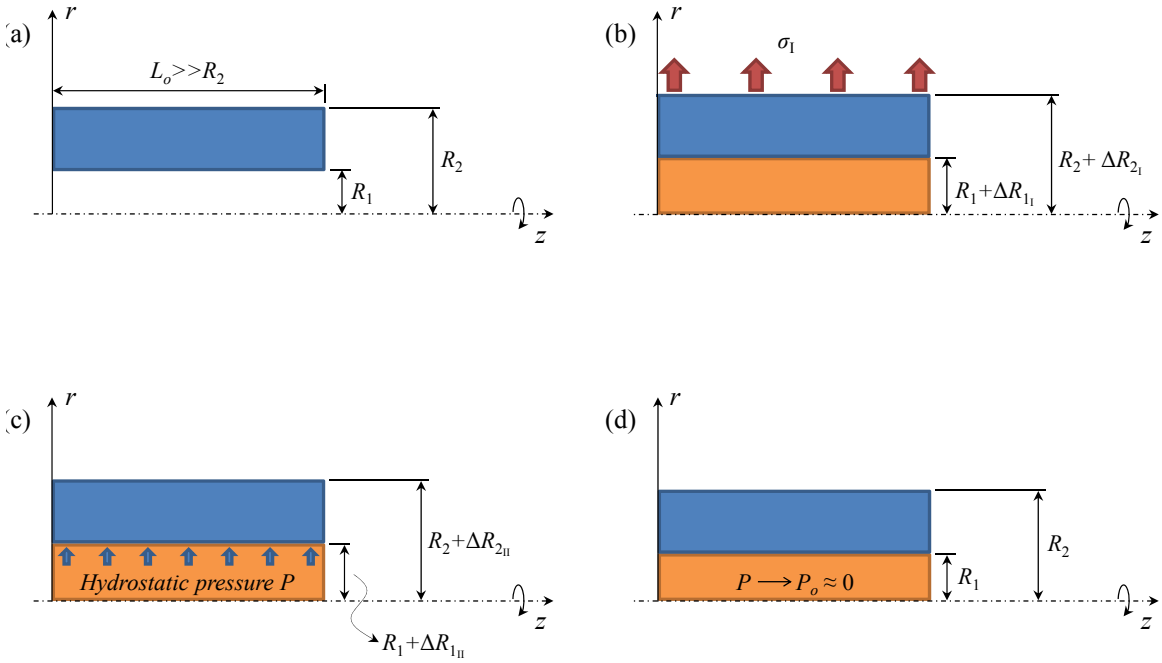

Figure 3.2: A schematic of the axisymmetric model. (a) A tube has an inner radius of R_1, an outer radius of R_2 and a half length of L. The specimen is symmetric about the center so half of the geometry is studied. The origin is located at the intersection of the z axis and the plane at the exit. (b) A uniform tensile traction σ_o is applied on the outer surface of the tube resulting in increases in the inner and outer radius. Then the tube is filled with fluid that has a reference pressure of P_o. (c) The applied traction is fully relaxed, resulting in a fluid pressure of P, which is much greater than P_o, built up in the core. (d) The fluid flows out of the tube driven by the difference between the fluid pressure and ambience. The fluid pressure P decreases during this process and its reduction accompanied by change in dimensions of the tube. The tube tends to restore its initial shape as P approaches the ambient pressure P_o.

pressure, P_o, so that P_o can be neglected. Driven by the pressure difference between within the fluid core and the ambience, the fluid flows until the stresses are fully relaxed and the tube restores its original closed shape, as shown in Fig. 3.2(d). In the following sections we discuss each stage of the process in details respectively.

3.3.1 Axisymmetric channel opening

The tube is expanded by applying a uniform tension to the outer surface of the tube. Consider a thin slice of the cylinder of length δL, with an inner radius of R_1, during the process, it is opened in the plane displacement condition. This problem can be analyzed using linear superposition of two sets of boundary conditions. The first set of boundary conditions are plane strain. The second set of boundary conditions include applying a tensile stress to satisfy the condition of zero net axial force.

The plane strain boundary conditions are:

$$\begin{aligned} \sigma_{rr} &= \sigma_o \ , \text{ at } r = R_2 \ ; \\ \sigma_{rr} &= 0 \ , \text{ at } r = R_1 \ ; \\ \varepsilon_{zz} &= 0 \ . \end{aligned} \tag{3.17}$$

Solving the Lamé equations with these boundary conditions, we can get $C_1 = k^2\sigma_o/(k^2 - 1)$ and $C_2 = -k^2\sigma_o R_1^2/(k^2 - 1)$, where $k = R_2/R_1$. Using Hooke's law in plane strain, the axial stress is solved. The stresses in plane strain are given by

$$\begin{aligned} \sigma_{rr} &= \frac{k^2}{k^2 - 1}\left(1 - \frac{R_1^2}{r^2}\right)\sigma_o \ , \\ \sigma_{\theta\theta} &= \frac{k^2}{k^2 - 1}\left(1 + \frac{R_1^2}{r^2}\right)\sigma_o \ , \\ \sigma_{zz} &= \frac{k^2}{k^2 - 1}\sigma_o \ . \end{aligned}$$

Integrating this stress over the tube cross-section area leads to a non-zero axial tension of

$$F_z = \pi R_1^2 k^2 \sigma_o \ . \tag{3.18}$$

The strains under plane strain are :

$$\begin{aligned}
\varepsilon_{rr} &= -\frac{3\sigma_o}{2E}\frac{k^2R_1^2}{(k^2-1)r^2}\,, \\
\varepsilon_{\theta\theta} &= \frac{3\sigma_o}{2E}\frac{k^2R_1^2}{(k^2-1)r^2}\,, \\
\varepsilon_{zz} &= 0\,.
\end{aligned} \tag{3.19}$$

To get the net axial force to be zero, a compression of the same magnitude as the tension calculated above is applied to the cylinder. The boundary conditions are:

$$\sigma_{zz} = -\frac{k^2}{k^2-1}\sigma_o\,, \tag{3.20}$$

and all the other stresses are zero.

Using Hooke's law, the strains in this condition are

$$\begin{aligned}
\varepsilon_{rr} &= \frac{\sigma_o}{E}\frac{k^2}{2(k^2-1)}\,, \\
\varepsilon_{\theta\theta} &= \frac{\sigma_o}{E}\frac{k^2}{2(k^2-1)}\,, \\
\varepsilon_{zz} &= -\frac{\sigma_o}{E}\frac{k^2}{k^2-1}\,,
\end{aligned} \tag{3.21}$$

By linear superposition, the final stress and strain fields during the channel opening

process are:

$$\begin{aligned}
\sigma_{rr} &= \left(\frac{k^2}{k^2-1} - \frac{k^2}{k^2-1}\frac{R_1^2}{r^2}\right)\sigma_o\,, \\
\sigma_{\theta\theta} &= \left(\frac{k^2}{k^2-1} + \frac{k^2}{k^2-1}\frac{R_1^2}{r^2}\right)\sigma_o\,, \\
\sigma_{zz} &= 0\,, \\
\varepsilon_{rr} &= \frac{\sigma_o}{E}\left(\frac{k^2}{2(k^2-1)} - \frac{3k^2}{2(k^2-1)}\frac{R_1^2}{r^2}\right), \\
\varepsilon_{\theta\theta} &= \frac{\sigma_o}{E}\left(\frac{k^2}{2(k^2-1)} + \frac{3k^2}{2(k^2-1)}\frac{R_1^2}{r^2}\right), \\
\varepsilon_{zz} &= -\frac{\sigma_o}{E}\frac{k^2}{k^2-1}\,,
\end{aligned} \tag{3.22}$$

For the thin slice of cylinder considered, the inner radius and length are changed by:

$$\begin{aligned}
\frac{\Delta R_1}{R_1} &= \frac{2k^2\sigma_o}{E(k^2-1)}\,, \\
\frac{\Delta\delta L}{\delta L} &= -\frac{\sigma_o}{E}\frac{k^2}{k^2-1}\,.
\end{aligned}$$

The core volume for a cylinder is $V = \pi R_1^2 \delta L$. Therefore change in the core volume is given by

$$\frac{\Delta V}{V} = 2\frac{\Delta R_1}{R_1} + \frac{\Delta\delta L}{\delta L}. \tag{3.23}$$

During channel opening, the change in core volume is:

$$\frac{\Delta V}{V} = \frac{4k^2\sigma_o}{E(k^2-1)} - \frac{\sigma_o}{E}\frac{k^2}{k^2-1}. \tag{3.24}$$

3.3.2 Initial narrowing during relaxation of the applied tension

At the end of channel opening (Fig. 3.2(b)), the tube is expanded uniformly in the radial direction. Fluid fills the tube and is at rest, with a reference pressure P_o as the ambience. The applied traction σ_o is then relaxed incrementally. As stated before, the increments were slow enough that fluid can flow in a cross-section of the cylinder, and an equilibrium is always maintained in the fluid. Plane sections remain plane, and no net axial tension at a section. Since the fluid is incompressible, the volume of the fluid core remains constant.

The problem can also be analyzed as a superposition of two sets of boundary conditions, of which one being plane strain, and the other being no net axial force.

The plane strain boundary conditions are:

$$\begin{aligned} \sigma_{rr} &= 0 \,, \text{ at } r = R_2 \,; \\ \sigma_{rr} &= -P \,, \text{ at } r = R_1 \,; \\ \varepsilon_{zz} &= 0 \,. \end{aligned} \tag{3.25}$$

Using Lamé equations and Hooke's law with the above boundary conditions, the stresses and strains are

$$\begin{aligned} \sigma_{rr} &= \frac{P}{k^2-1} - \frac{PR_2^2}{r^2(k^2-1)} \,, \\ \sigma_{\theta\theta} &= \frac{P}{k^2-1} + \frac{PR_2^2}{r^2(k^2-1)} \,, \\ \sigma_{zz} &= \frac{P}{k^2-1} \,, \\ \varepsilon_{rr} &= -\frac{3P}{2E}\frac{R_2^2}{r^2(k^2-1)} \,, \\ \varepsilon_{\theta\theta} &= \frac{3P}{2E}\frac{R_2^2}{r^2(k^2-1)} \,, \\ \varepsilon_{zz} &= 0 \,. \end{aligned} \tag{3.26}$$

It can be found that the axial stresses calculated from the plane strain conditions satisfy

that the axial tension in the elastic tube to be $\pi R_1^2 P$. This combined with the hydrostatic fluid pressure of P, leads to a net axial force of zero at a section. So the calculations are completed for both sets of boundary conditions. The inner radius and length of the slice of cylinder are changed by:

$$\begin{aligned} \frac{\Delta R_1}{R_1} &= \frac{3P}{2E}\frac{k^2}{k^2-1}\,, \\ \frac{\Delta \delta L}{\delta L} &= 0\,. \end{aligned} \tag{3.27}$$

And the change in core volume is

$$\frac{\Delta V}{V} = \frac{3P}{E}\frac{k^2}{k^2-1}. \tag{3.28}$$

Equating the change in volume as in Eqn. 3.24 and 3.28, the fluid pressure is solved to have the same value as σ_o. Upon full relaxation of the applied tension, the fluid cylinder core has a pressure of $P = \sigma_o$ and a radius of $R = R_1(1 + 3Pk^2/2E(k^2 - 1)$. This provides the initial condition for the following analysis of viscous flow of the core.

3.3.3 Viscous flow of the core

Now that the fluid has a uniform hydrostatic pressure of P that has an initial value of σ_o, the difference between the fluid pressure and ambience will drive the fluid to flow. Assuming a no-slip boundary condition at the interface between the inner surface of the tube and the fluid core, the stress and displacement in the radial direction are continuous across the interface between the fluid and the tube. At a cross-section of the cylinder, the net axial force is zero.

For the tube, reduction in the fluid pressure leads to further relaxation of stresses and decrease in the radius. Using Lamé equations and Hooke's law for a thick-walled cylinder with an internal pressure of P that decreases from an initial value of σ_o and no net axial force for the tube and the core, the relationship between the displacement of the inner surface of the tube and the fluid pressure is of the form:

$$\frac{\Delta R}{R_1} = \frac{3k^2}{2(k^2-1)} \frac{P-\sigma_o}{E} , \tag{3.29}$$

where ΔR designates the change of the inner radius of the tube.

Fluid flow will first initiate at the ends of the tube, where it is driven by the difference between the pressure within the tube and the ambience. Assuming a very long tube, when the flow is first initiated, the fluid located close to the center of the tube is without a pressure gradient and is still static. Once the fluid flows, the local pressure decreases and the local interface radius decreases according to Eqn. 3.29. Thus, the fluid pressure P is a function of location and time. Correspondingly, the interface radius is also a function of location and time. A continuous pressure gradient is built up gradually along the length of the tube. As a result, the tube narrows gradually from the exit towards the center.

Within a small length of the tube, the change in the inner radius is negligible, thus the local flow driven by the pressure difference can be described by a Poiseulle flow, whose volumetric flow rate follows:

$$\dot{Q}(z) = -\frac{\pi R_1^4}{8\eta} \frac{\partial P}{\partial z} , \tag{3.30}$$

where z is the axial distance along the cylinder measured from the end of tube, and $\dot{Q}(z)$ is the volumetric flow rate.

By mass conservation we have

$$2\pi R_1 dR dz = -\dot{Q}(z) dt \tag{3.31}$$

Substituting Eqn. 3.30 and 3.31 into Eqn. 3.29, with the variables normalized as: $\tau = Et/\eta$, $\psi = R/R_1, \zeta = z/R_1$, where R designates the current inner radius of the tube. With $\zeta = 0$ at the exit of the tube, we can get

$$\frac{\partial \psi}{\partial \tau} = \frac{k^*}{16} \frac{\partial^2 \psi}{\partial \zeta^2}, \tag{3.32}$$

where $k^* = 2(k^2-1)/3k^2$. The radius of inner surface is a function of axial location and time, $\psi = \psi(\zeta, \tau)$. The equation has the form of a diffusion equation. Assuming an infinitely long

tube, by separation of variables, the general solution for the inner radius is in the form of:

$$\psi(\zeta,\tau) = 1 + K_1 \,\mathrm{erf}\left(\frac{2\zeta}{\sqrt{k^*\tau}}\right), \tag{3.33}$$

where K_1 is the maximum collapse of the interface when the fluid is fully relaxed and the flow completely ceases, which is given by $K_1 = \Delta\psi_{max} = 3\sigma_o k^2/2E(k^2-1)$.

An equivalent form of Eqn. 3.33 is:

$$\frac{\Delta\psi}{\Delta\psi_{max}} = \mathrm{erfc}\left(\frac{2\zeta}{\sqrt{k^*\tau}}\right), \tag{3.34}$$

where erfc is the complimentary error function, and $\Delta\psi/\Delta\psi_{max}$ is the degree of interface collapse. At the exit of the cylinder, the interface very quickly collapses by a significant amount. Then the interface gradually narrows with the front of the interface collapse moving from the exit to the center.

If we define a front of collapse as $\Delta\psi/\Delta\psi_{max} = 50\%$ after the initial uniform collapse. From equation 3.34, we can get

$$\zeta = 0.238\sqrt{k^*\tau}\,, \tag{3.35}$$

showing the distance that the collapse front travel as a function of time. This front travels faster in a system with a thicker elastic wall. For a system with an infinitely large outer radius, the factor k^* approaches $2/3$.

The analytical solution of the profile of inner surface of the tube can be obtained from Eqn. 3.35. However it should be noted that the derivation of this equation is based on the assumption of an infinitely long tube. For a tube with finite length, Eqn. 3.35 is no longer valid, while Eqn. 3.29, 3.30, and 3.31 provide a non-closed form solution. Numerical calculation on the basis of this non-closed form solution is used to predict the real-time channel profiles for tubes with finite lengths. The channel is segmented into thin slices of small length δL as shown in Fig. 3.3. It is approximated that the j-th element has a uniform pressure of P_j and a radius of R_j, where P_j and R_j are related by Eqn. 3.29. The pressure gradient at the exit of the channel is calculated by dividing the pressure of the first element by δL. Inside the channel, the pressure gradient in the j-th element is $(P_{j+1} - P_j)/\delta L$. The volumetric flow rate at each element driven by pressure gradient can be determined using Poiseuille equation. The corresponding deformation at each time step is then calculated by Eqn. 3.31 and iterated over time.

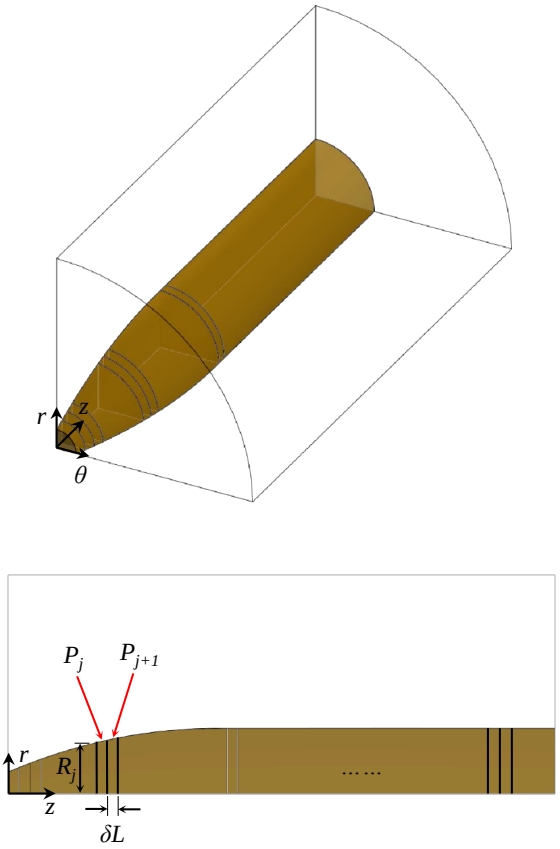

Figure 3.3: A schematic showing the model used in the numerical calculation for channel narrowing, where a long concentric cylinder is segmented into thin slices. Each slice has a length of δL,and a radius of R_j, which has an initial value $R_j(0) = R_{1_o} + \Delta R_{1_I} + \Delta R_{1_{II}}$ calculated in the previous section. The pressure in each slice, P_j has an initial value of σ_o. Equation 3.29, 3.30, and 3.31 are used to calculate the time-dependent profile of the inner surface of the tube.

Fig. 3.4 shows the channel profile calculated analytically for an infinitely long tube within a length of $z/R_1 = 1000$, and numerically for the case of $L/R_1 = 1000$. In both cases, $k^* = 2/3$ and $\sigma_o/E = 0.01$. It can be found that before the center of the tube starts to close, the analytical results and numerical results display excellent agreement. However, after the center of the tube starts to narrow, only the numerical solution is valid for a tube with finite length. For example, the numerical solution satisfies the zero pressure gradient at the center of the tube which is required by the boundary condition of symmetry. The results also show that a tube with finite length can close almost fully within finite time. A cartoon based on the calculated channel profile is shown in Fig. 3.5 demonstrating the gradual narrowing process.

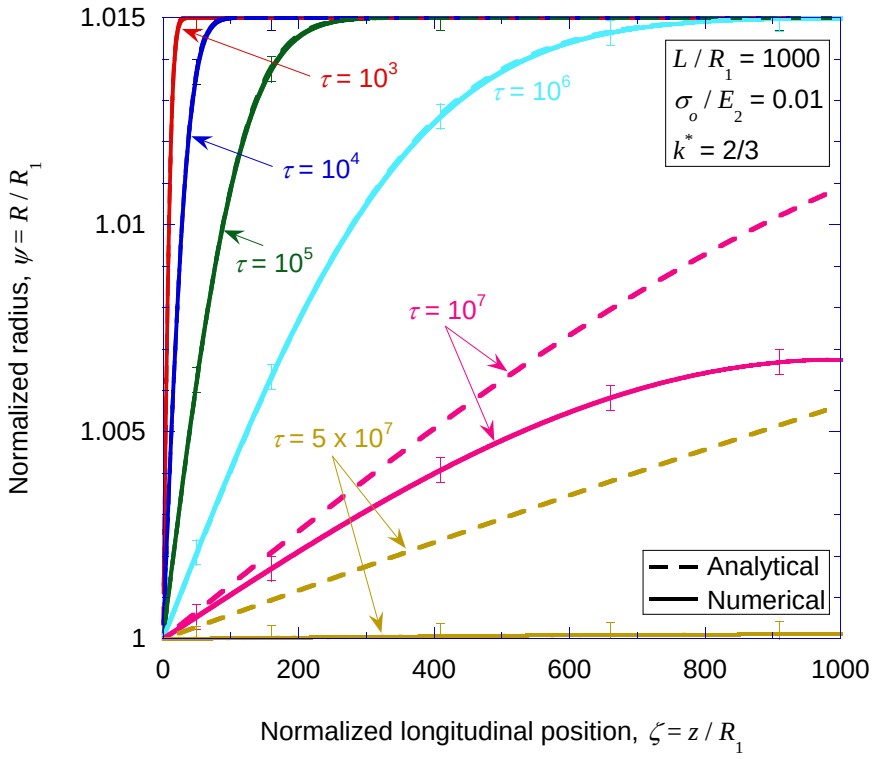

Figure 3.4: Profile of the inner surface of a circular channel with infinite wall-thickness at different times. The analytical solution for an infinitely long tube agrees with the numerical solutions prior to the center of the tube starts to collapse. To predict the gradual collapse, especially the complete collapse of tubes with finite lengths, numerical calculation based on the non-closed form solution is needed.

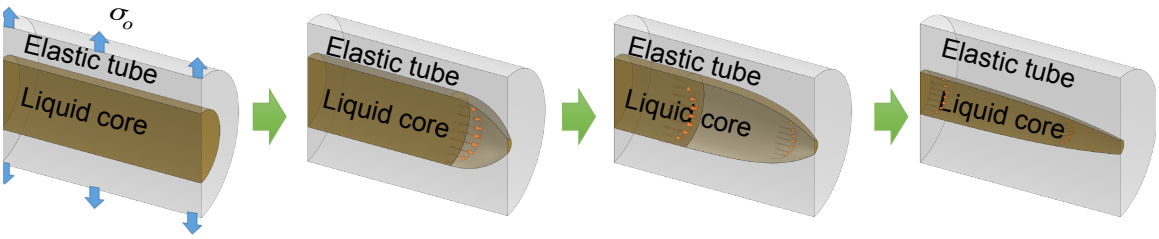

Figure 3.5: A cartoon based on the numerical calculation showing liquid-filled thick-walled tube narrows gradually from the exit towards the center upon applied remote compression. Local Poiseuille flow is driven by the pressure gradient. The shape change and dimensions are exaggerated and do not reflect real data.

3.4 Elliptic channel in thick substrates

The channels fabricated by tunneling cracking of layered structures can be modeled by elliptic channels in infinite elastic body, since the channel width and depth are much smaller than the crack spacing and the thickness of the substrate [2,7]. We assume that a channel in the closed state has an elliptic cross-section with a major radius of a_o, a minor radius of b_o, and a half length of L_o, where L_o is much larger than a_o and b_o. The process is very similar to the previous case of axisymmetric tube, except that the channel is opened by applying a remote uniaxial tension of σ_o in the direction of the minor radius instead of a uniform traction in all directions. While the channel is held in the opened state, it is filled with fluid. Then the applied tension is relaxed in increments to narrow the channel, resulting in a pressure built up in the fluid, which will later drive the fluid to flow until the channel returns to the original closed state. The process is depicted in Fig. 3.6, where a quarter of the model is shown given the symmetry of the geometry.

The same notations as in the previous section of axisymmetric problem are used in this section. The elastic body is made of an incompressible elastic material with a modulus of E and a Poisson's ratio of $\nu = 0.5$. The fluid is incompressible and has a viscosity of η.

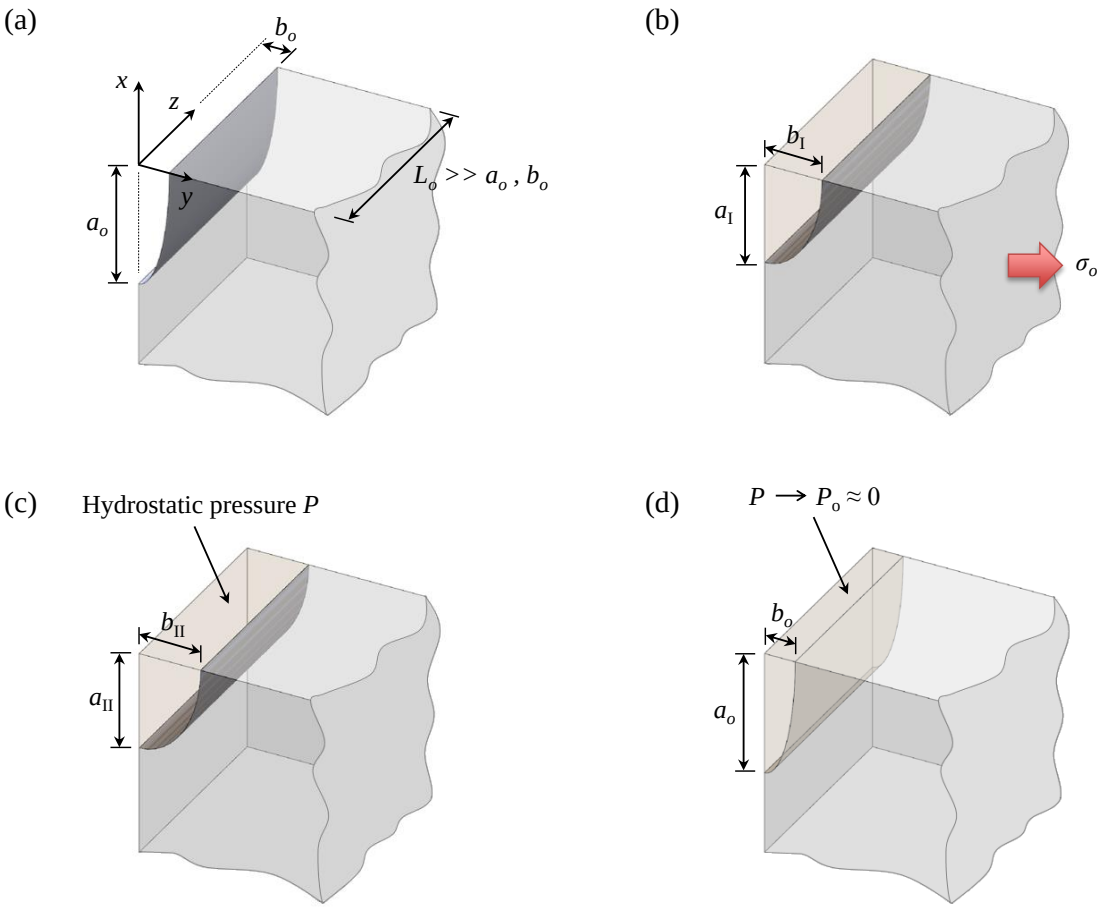

Figure 3.6: (a) The elliptic channel has initial sizes of a_o and b_o. (b) A remote tension of σ_o is applied to open the channel to sizes of a_I and b_I. While the channel is held open, it is filled with fluid that is static with a reference pressure as the ambience of P_o. (c) The applied tension is relaxed in increments to zero, resulting in a fluid pressure of P. The cross-sectional area remains the same satisfying mass conservation, while the two radii change to a_{II} and b_{II}. This is the initial state from which flow occurs. The dimensions in the schematics are exaggerated for ease of visualization and do not reflect the real dimension changes.(d) The fluid pressure is fully relaxed and the channel restore the initial shape as (a) while it is filled with fluid.

The general solution for stresses in an infinite plate with an elliptic hole was provided by Inglis [36], where the stresses were expressed in the form of infinite series with parameters A_n and B_n. Cartesian coordinates with x and y aligned with the major and minor radius

respectively are transformed to curvilinear coordinates α, β by:

$$x = \sqrt{{a_o}^2 - {b_o}^2}\cosh\alpha\cos\beta\,,$$
$$y = \sqrt{{a_o}^2 - {b_o}^2}\sinh\alpha\sin\beta\,, \tag{3.36}$$

The surface of an elliptic hole is defined by $\alpha = \alpha_o = \tanh^{-1}(b_o/a_o)$. The z-axis is in the longitudinal direction pointing from the exit to the center. The stress and displacement fields and the correspondent shape changes can be calculated based on different boundary conditions. Comparing with the case of axisymmetric channels, the opening and narrowing of elliptical channels are complicated by the shape change, which are addressed in the following sections.

3.4.1 Elliptic channel opening

The first set of calculations were conducted for channel opening when the elastic body is subjected to a uniaxial tension as shown in Fig. 3.6 (a)–(b). The boundary conditions are remote tension of σ_o in the direction of the minor radius, zero stress in the longitudinal direction and free surface at the surface of the ellipse. The parameters A_n and B_n for the stress field in this condition were provided by Inglis [36], based on which the in-plane stresses are:

$$\begin{aligned}
\sigma_{\alpha\alpha} =& \frac{-\sigma_o}{8(\cosh 2\alpha - \cos 2\beta)^2}\{2e^{2\alpha_0}[1-\cosh(2\alpha-2\alpha_0)]\cos(4\beta)\\
&+2e^{2\alpha_0}[\cosh(4\alpha-2\alpha_0)+3\cosh(2\alpha_0)-4\cosh(2\alpha)]\cos(2\beta)\\
&+4\cosh(2\alpha_0)\sinh(2\alpha)-2\sinh(4\alpha)-3e^{-2\alpha+4\alpha_0}-e^{2\alpha}+4e^{2\alpha_0}\\
&-e^{2\alpha}-2e^{-2\alpha}-4e^{2\alpha_0}\}\,,\\
\sigma_{\beta\beta} =& \frac{\sigma_o}{8(\cosh 2\alpha - \cos 2\beta)^2}\{-2e^{2\alpha_0}[1+\cosh(2\alpha-2\alpha_0)]\cos(4\beta)\\
&+2e^{2\alpha_0}\left[\cosh(4\alpha-2\alpha_0)+3\cosh(2\alpha_0)+8e^{-2\alpha}-4e^{2\alpha-2\alpha_0}+4e^{-2\alpha-2\alpha_0}\right]\cos(2\beta)\\
&+4\cosh(2\alpha_0)\sinh(2\alpha)-2\sinh(4\alpha)-3e^{-2\alpha+4\alpha_0}-2e^{2\alpha_0-4\alpha}\\
&-2e^{-2\alpha}+2e^{2\alpha_0-4\alpha}\}\,,
\end{aligned} \tag{3.37}$$

Similar to the axisymmetric problem, the opening process of an elliptic channel in an infinite body can also be analyzed by the superposition of plane strain conditions and no net axial force. A thin slice of the elliptic channel of length δL, with the major and minor axis of the ellipse being a_o and b_o respectively is in an infinite elastic body. The first set of calculations are with plane strain boundary conditions. Using Hooke's law with the above in-plane stresses, the axial stress is

$$\sigma_{zz} = \frac{\sigma_o}{2}\left(-e^{2\alpha_o} + \frac{\left(e^{2\alpha_o}+1\right)\sinh 2\alpha}{\cosh 2\alpha - \cos 2\beta}\right). \tag{3.38}$$

In order to evaluate the change in dimensions of the channel, displacements are calculated using the equations for strains provided by Inglis [36] as

$$\varepsilon_{\alpha\alpha} = h^2\frac{\partial u}{\partial \alpha} + \frac{u}{2}\frac{\partial h^2}{\partial \alpha} - \frac{v}{2}\frac{\partial h^2}{\partial \beta}, \tag{3.39}$$

$$\varepsilon_{\beta\beta} = h^2\frac{\partial v}{\partial \beta} + \frac{v}{2}\frac{\partial h^2}{\partial \beta} - \frac{u}{2}\frac{\partial h^2}{\partial \alpha}, \tag{3.40}$$

where h is the scaling factor with

$$h^2 = \frac{2}{c^2\left(\cosh 2\alpha - \cos 2\beta\right)}. \tag{3.41}$$

u and v are defined as

$$u = X_n[(n+p)e^{-(n-1)\alpha}\cos(n+1)\beta + (n-p)e^{-(n+1)\alpha}\cos(n-1)\beta] + Y_n e^{-n\alpha}\cos n\beta, \tag{3.42}$$

$$v = X_n[(n-p)e^{-(n-1)\alpha}\sin(n+1)\beta + (n+p)e^{-(n+1)\alpha}\sin(n-1)\beta] + Y_n e^{-n\alpha}\sin n\beta, \tag{3.43}$$

where p is related to the Poisson's ratio ν, with $p = 3-4\nu$ in plane strain and $p = (3-\nu)/(\nu+1)$ in plane stress. Their relationships with the displacements in the normal and tangential directions are:

$$u = \frac{u_\alpha}{h}, \text{ and } v = \frac{u_\beta}{h}. \tag{3.44}$$

By Hooke's law, we can relate X_n and Y_n with A_n and B_n, with

$$A_n = 2nX_n \frac{E}{3c^2}, \tag{3.45}$$

$$B_n = \frac{2E}{3c^2} Y_{n+1}. \tag{3.46}$$

Substituting in the stresses in plane strain, the change in the major and minor radii in plane strain are

$$\begin{aligned} \Delta a &= -\frac{3\sigma_o}{4E} a_o \ , \\ \Delta b &= \frac{3\sigma_o}{4E} \left(2a_o + b_o\right) \ . \end{aligned} \tag{3.47}$$

The average stress at any α can be obtained by integrating the axial stress derived above in the interval of $0 \le \beta \le \pi/2$, and from the standard integral of

$$\int_o^\pi \frac{dx}{m_1 + m_2 \cos x} = \frac{\pi}{\sqrt{m_1^2 - m_2^2}} \ , \left(m_1^2 > m_2^2\right) \ . \tag{3.48}$$

Thus the average axial stress under plane strain is

$$\begin{aligned} \bar{\sigma}_{zz} &= \frac{1}{\pi/2} \int_0^{\pi/2} \sigma_{zz} d\beta \\ &= \frac{1}{\pi/2} \frac{\sigma_o}{2} \int_0^{\pi/2} \left(-e^{2\alpha_o} + \frac{\left(e^{2\alpha_o} + 1\right) \sinh 2\alpha}{\cosh 2\alpha - \cos 2\beta} \right) d\beta \\ &= \frac{\sigma_o}{2} \ . \end{aligned} \tag{3.49}$$

Since the average axial stress is constant at any α, the average stress in the cross-section of the elastic body in the plane strain condition is $\sigma_o/2$. Now apply a uniform compression of $\sigma_a = -\sigma_o/2$ to get no net axial force. It should be noted that although the final axial stress in the elastic body is dependent on β and α, the net force is zero, and the displacements will

be plane. Using Hooke's law, the strains resulted from the uniform compression are:

$$\varepsilon_{\alpha\alpha} = \varepsilon_{\beta\beta} = \frac{\sigma_o}{4E} ,$$
$$\varepsilon_{zz} = -\frac{\sigma_o}{2E} . \tag{3.50}$$

Thus in this condition, the changes in the major and minor radii of the elliptic channel are

$$\Delta a = \frac{\sigma_o}{4E} a_o ,$$
$$\Delta b = \frac{\sigma_o}{4E} b_o . \tag{3.51}$$

Combining the results from both conditions, the displacements are

$$\Delta a = -\frac{\sigma_o}{2E} a_o ,$$
$$\Delta b = \frac{3\sigma_o}{2E} a_o + \frac{\sigma_o}{E} b_o , \tag{3.52}$$

and

$$\varepsilon_{zz} = -\frac{\sigma_o}{2E} . \tag{3.53}$$

Now we calculate the volume change of the core. For a slice of elliptical core of length δL, with major and minor radius of a_o and b_o, the volume is $V = \pi a_o b_o \delta L$. Therefore the change in volume is given by

$$\frac{\Delta V}{V} = \frac{\Delta a}{a_o} + \frac{\Delta b}{b_o} + \frac{\Delta \delta L}{\delta L} . \tag{3.54}$$

During channel opening, using the displacements calculated above, the change in core volume is

$$\frac{\Delta V}{V} = \frac{3\sigma_o}{2E} \phi_o , \tag{3.55}$$

where ϕ_o is the aspect ratio of the channel, with $\phi_o = a_o / b_o$.

3.4.2 Initial narrowing upon relaxation of the applied tension

Similar to the axisymmetric case, while the channel is held open, it is filled with fluid. Then the applied tension is relaxed in increments, tending to narrow the channel to a smaller cross-sectional area. The same assumptions are made for the fluid, that is the fluid can flow in a cross-section, and an equilibrium is maintained in the fluid. The fluid has a uniform hydrostatic pressure, and the volume of the fluid core remains constant.

The first set of calculations are for plane strain condition when an infinite elastic body is subjected to an internal pressure of P

$$\begin{aligned}
&\sigma_{\alpha\alpha} = -P\,, \tau_{\alpha\beta} = 0\,, \text{at } \alpha = \alpha_o\,; \\
&\sigma_{\alpha\alpha} = 0\,, \text{at } \alpha = \infty\,; \\
&\sigma_{\beta\beta} = 0\,, \text{at } \alpha = \infty\,; \\
&\tau_{\alpha\beta} = 0\,, \text{at } \alpha = \infty\,; \\
&\varepsilon_{zz} = 0\,.
\end{aligned} \tag{3.56}$$

Using the equations for the stress and displacement field provided by Inglis [36] and the above boundary conditions, the stresses are solved as:

$$\begin{aligned}
\sigma_{\alpha\alpha} &= -\frac{P}{4(\cosh 2\alpha - \cos 2\beta)^2}\left(2\cos 4\beta - 8\cos 2\beta\cosh 2\alpha + 4 + 2e^{-4\alpha} + \frac{\sinh 4\alpha_o}{\sinh 2\alpha_o}2\sinh 2\alpha\right), \\
\sigma_{\beta\beta} &= -\frac{P}{4(\cosh 2\alpha - \cos 2\beta)^2}\left(2\cos 4\beta - 8e^{-2\alpha}\cos 2\beta + 4 + 2e^{-4\alpha} + \frac{\sinh 4\alpha_o}{\sinh 2\alpha_o}2\sinh 2\alpha\right), \\
\tau_{\alpha\beta} &= \frac{P}{2(\cosh 2\alpha - \cos 2\beta)^2}\left(2\sin 2\beta\cosh 2\alpha + \frac{\sinh 4\alpha_o}{\sinh 2\alpha_o}2\sin 2\beta\right), \\
\sigma_{zz} &= -P\left(1 - \frac{\sinh 2\alpha}{\cosh 2\alpha - \cos\beta}\right).
\end{aligned} \tag{3.57}$$

The change in major and minor radii of the channel are:

$$\Delta a = \frac{3P}{2E} b_o \,,$$
$$\Delta b = \frac{3P}{2E} a_o \,. \tag{3.58}$$

Using the same method as in the previous section, the average axial stress at any α is

$$\begin{aligned}\bar{\sigma}_{zz} &= \frac{1}{\pi/2}\int_0^{\pi/2} \sigma_{zz} d\beta \\ &= \frac{-P}{\pi/2}\int_0^{\pi/2} \left(1 - \frac{\sinh 2\alpha}{\cosh 2\alpha - \cos 2\beta}\right) d\beta \\ &= 0 \,. \end{aligned} \tag{3.59}$$

The axial stress on the surface due to the internal pressure in the plane strain condition is zero. To get the net load at a section be zero a stress of σ_a should be applied, which is given by

$$\sigma_a = 0 + \frac{P\pi a_o b_o}{A_{sub}} \,, \tag{3.60}$$

where A_{sub} is the cross-section area of the elastic body which approaches infinity. Therefore this applied stress is negligible, and the solutions are plane strain.

The change in the core volume is given by

$$\frac{\Delta V}{V} = \frac{3P}{2E}\left(\phi_o + \frac{1}{\phi_o}\right) . \tag{3.61}$$

Equating the volume change in Eqn. 3.61 and 3.55, the fluid pressure is related to the applied tension by

$$P = \frac{3\phi_o^2}{3\phi_o^2 + 1}\sigma_o. \tag{3.62}$$

Upon full relaxation of the applied tension, the fluid pressure P approaches the value of σ_o in channels with very high initial aspect ratios, and P approaches the value of $3\sigma_o/4$ in channels whose aspect ratio approaches one.

After the fluid pressure is built up, the major and minor radii of the channel are:

$$\begin{aligned} a_{\mathrm{II}} &= a_o + \frac{3P}{2E} b_o \,, \\ b_{\mathrm{II}} &= b_o + \frac{3P}{2E} a_o \,. \end{aligned} \tag{3.63}$$

3.4.3 Viscous elliptic cylinder flow

Att the end of last stage, a pressure of P is built up within the fluid. Driven by the pressure difference between within the fluid and the ambience, fluid begins to flow out of the channel, relaxing the stresses while enabling the channel to close.

The fluid pressure P has an initial value of P_i that is given by Eqn. 3.62. Using the above stress field, and the relationship between displacements and stresses provided by Inglis [36], the change in major and minor radii of the channel are related to the fluid pressure by:

$$\begin{aligned} \Delta a &= -\frac{3P_i - 3P}{2E} b \,, \\ \Delta b &= -\frac{3P_i - 3P}{2E} a \,. \end{aligned} \tag{3.64}$$

Similar to the axisymmetric problem, flow in an elliptic pipe has a flow rate of

$$\dot{Q}(z) = -\frac{\pi}{4\eta} \frac{\partial P}{\partial z} \frac{(a_o b_o)^3}{a_o^2 + b_o^2} \,. \tag{3.65}$$

By mass conservation, we have

$$dAdz = \dot{Q}dt \,. \tag{3.66}$$

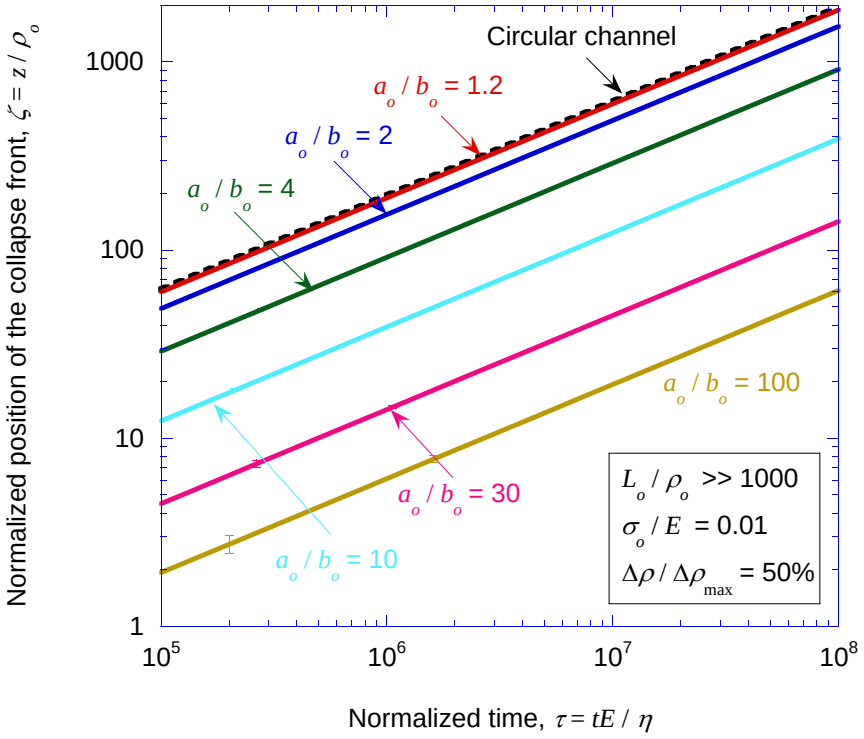

Figure 3.7: A collapse front defined by $\Delta\rho/\Delta\rho_{\max} = 50\%$ travels from the exit of the channel towards the center. The collapse fronts are before the center of the channel starts to collapse, such that they model the collapse front in an infinitely long channel. The collapse front in an elliptic channel travels to the same order of time as in the circular channel. As the original aspect ratio of the elliptic channel approaches one (indicating the elliptical channel approaching a circular channel), the curve approaches the analytical solution for an infinite axisymmetric tube. The narrowing of channels with higher aspect ratios is slower.

Unlike the axisymmetric case where we can get the analytical solution for the narrowing process, the elliptic problem is complicated by the shape change. We adapted the numerical model described in section 3.3.3 to the elliptic channel flow problem by incorporating all the elements discussed above. The average radius of an ellipse is defined as $\rho = \sqrt{ab}$. This is the equivalent for the radius in the axisymmetric case. The front of channel narrowing

is defined by the relative change in the average radius as $\Delta\rho/\Delta\rho_{\max}$. As discussed in the previous section, the collapse front of a finite channel travels at the same speed as that of an infinitely long channel before the center of the channel starts to narrow. Figure 3.7 shows that in an elliptic channel the collapse front travels to the same order of time as in the circular channel. The elliptic channels used in the analysis were long enough so that the tracked collapse fronts resemble those in infinitely long channels. Although the plot in Fig. 3.7 was for a specific collapse front defined by $\Delta\rho/\Delta\rho_{\max} = 50\%$, it was found that any arbitrary collapse front travels to the same order of time. Thus, a generalized form of Eqn. 3.35 for the collapse front traveling in an infinitely long channel is in the form of

$$\zeta = f_1\left(\phi_o, \frac{\Delta\rho}{\Delta\rho_{\max}}, \frac{\sigma_o}{E}\right)\sqrt{\tau}\,, \tag{3.67}$$

Because the shape of an elliptic channel changes with the applied tension, an extra term of σ_o/E is introduced. In the axisymmetric case, σ_o/E does not affect the collapse front because the channel shape is preserved. Representative values for f_1 are plotted in Fig. 3.8. As ϕ_o approaches 1, the curves approaches the analytical solution for circular channels with infinite outer radius which is given by $\sqrt{1/6}\,\mathrm{erfc}^{-1}(\Delta\rho/\Delta\rho_{\max})$. The value of f_1 decreases as the aspect ratio increases, indicating the narrowing of channels with higher aspect ratios is slower.

Figure 3.9 show the profiles of a channel with an initial aspect ratios of 100 at different times. Both major and minor radii decrease as the fluid pressure decreases during the viscous flow. The aspect ratio of the channel increases, while the cross-sectional area decreases as the fluid pressure decreases. An elliptic channel narrows towards a more crack-like shape with a smaller cross-section during the viscous flow.

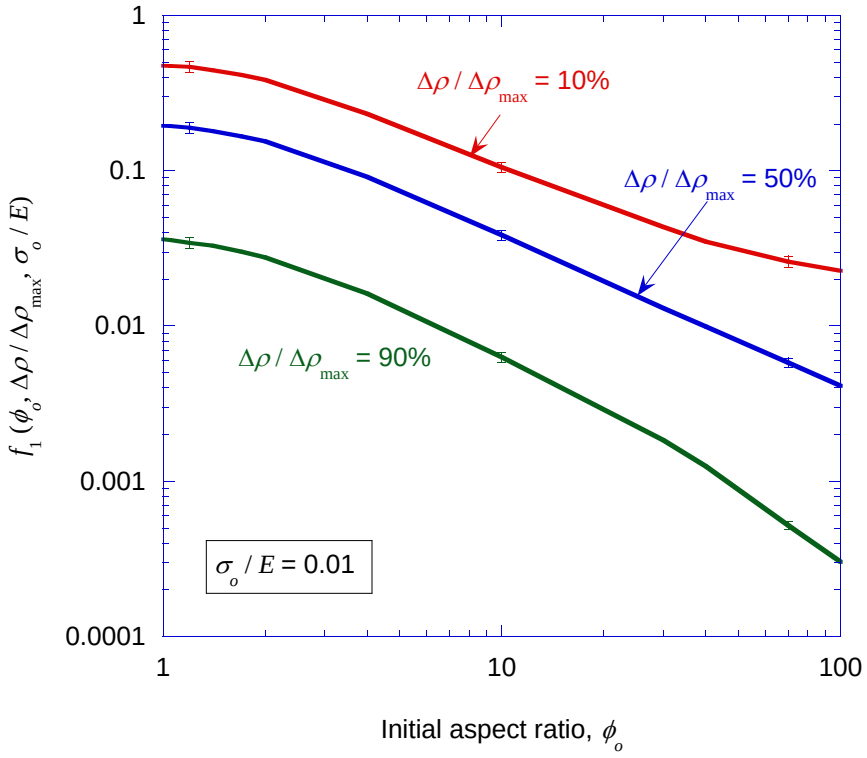

Figure 3.8: Representative values of f_1 as in Eqn. 3.67. The value of f_1 decreases as ϕ_o increases when the other to parameters are fixed, showing that the collapse front travels more slowly in a channel with higher aspect ratio. The error bars on these plots correspond to the numerical uncertainties associated with mesh size.

3.5 Discussion

The nonuniform narrowing of channels initiates from the exit of the channel and proceeds towards the center of the channel. The degree of channel narrowing can be evaluated by the percentage of channel narrowing of $\Delta\rho/\Delta\rho_{\max}$. Since the channel was originally expanded or opened by an applied tension, it will return to its original state upon full relaxation of the applied tension assuming all deformations are elastic. The degree of narrowing is a function of time and longitudinal location. The analytical solution for an infinitely long axisymmetric tube was given by Eqn. 3.34. The numerical method introduced in the pervious sections enabled us to analyze the collapse of a channel with arbitrary cross-sectional shape and length.

The motivation of the analyses was to understand the effect of nonuniform narrowing

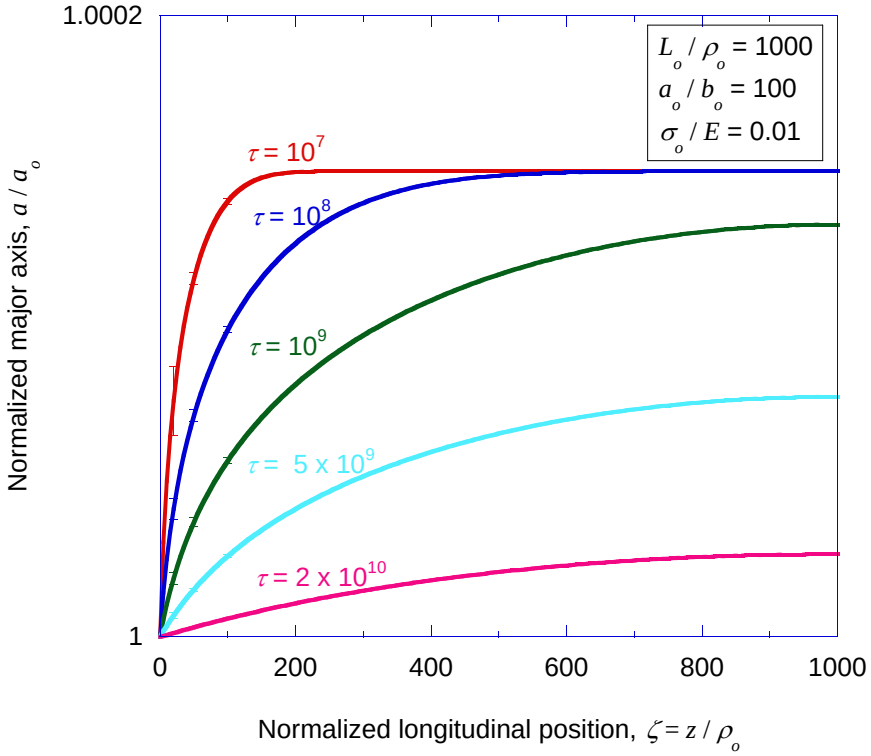

Figure 3.9 (a)

on the application of linearization of DNA and chromosome in the narrowing nannochannels [2]. The channel used were fabricated by tunneling cracking of layered structures of oxidized PDMS film between PDMS substrates. The channels have a half length of 500 μm and were opened by different values of applied tension up to 10%. It was believed that the linearization of DNA was facilitated by the nanoconfinement and the nanosqueeze flow generated during the narrowing process. It was measured by electrical-impedance experiment that the most widely opened channels (at 10%) have an equivalent radius of 0.1μm [2]. The channel length is much bigger than the equivalent radius. By different assumptions of original channel shape in the closed state, we can calculate the time required for the center of such a channel to close by any given degree upon full relaxation of the applied tension as shown in Fig. 3.10. It was shown that if the channels in the closed state are more crack-like which is of higher aspect ratios, the time to reach full closure is longer. Assuming the channel being in a homogeneous substrate of PDMS, which has a modulus of $E = 3$ MPa, and the fluid being a water-based solution, the time constant $\eta/E = 3\times10^{-10}$ s, the time required for the center of a channel to reach 99% of closure can be as long as 0.6 hr. The difference of narrowing between the ends and the center of the channel can be significant. Especially, when a high applied tension was fully relaxed, the significant

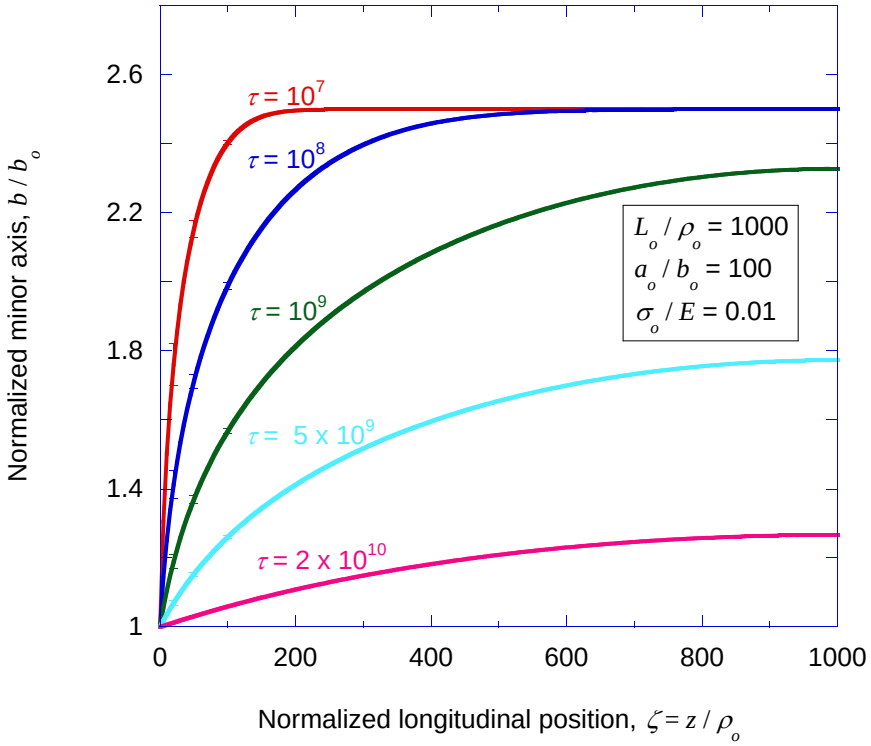

Figure 3.9 (b)

dimension difference between the ends and the center may exhibit as partial collapse of the channel with significant amount of fluid trapped in the channel [2].

Equation 3.35 shows that for an infinitely long channel, and a defined collapse front of $\Delta\rho/\Delta\rho_{\max}$, the distance that the collapse front travels and the time has a quadratic relationship. This solution is not applicable for a channel with finite length or of different cross-sections. By conducting the numerical calculations for channels with varied lengths, the times required for the center of each channel to reach a defined degree of closure of $\Delta\rho/\Delta\rho_{\max}$ = 50% were plotted as functions of channel length as shown in Fig. 3.11. It was found that the time and channel length also have a quadratic relationship with the time related to the square of channel length.

3.6 Conclusions

In this study, we proposed a model for the time-dependent narrowing process of liquid-filled channels. The narrowing is a result of relaxation of the applied tension that opened

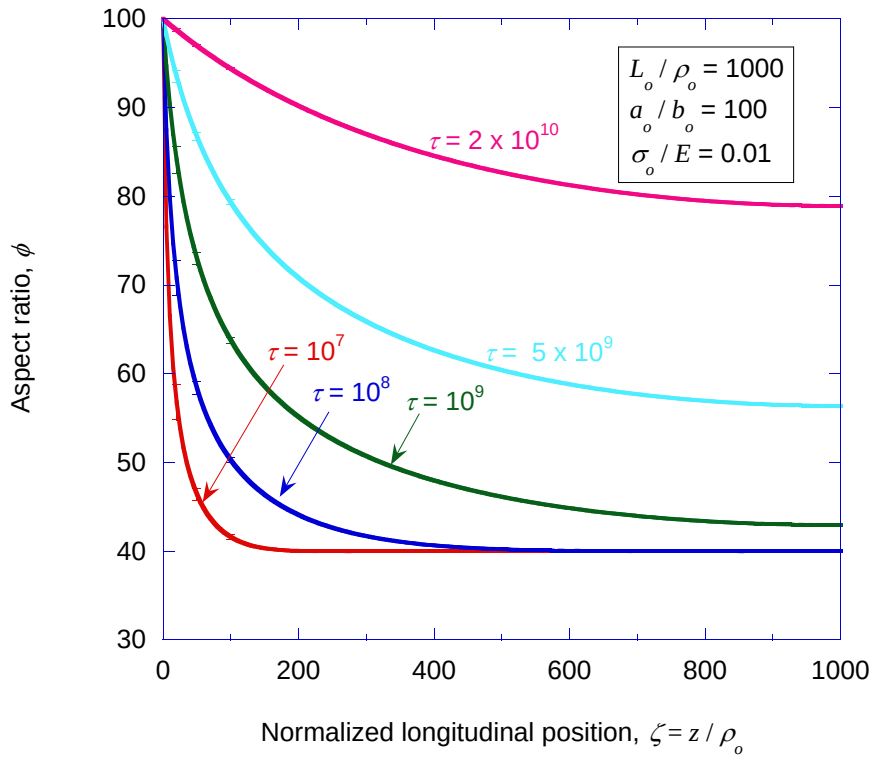

Figure 3.9 (c)

the channel. The non-uniform narrowing initiates from the ends of the channel and proceeds towards the center. The profile of the inner surface of the channel is dependent on the longitudinal location and time. We first analyzed the general case of an axisymmetric thick-walled tube and found an analytical solution for an infinitely long axisymmetric thick-walled tube. The solution showed a quadratic relationship between the location and time for a certain degree of channel narrowing to be observed in the form of Eqn. 3.33. A numerical method was developed to discover the closure of a channel with finite length. It was shown that a finite tube can close almost fully within finite time.

Elliptic channels in infinite elastic body were analyzed as a better approximation for the channels fabricated by tunneling cracking used in the literature [1, 2, 7]. The stress and displacement fields in the elastic body with an elliptic hole were analyzed, and a numerical method was developed to determine the time-dependent closure of an elliptic channel with finite length. It was found that channels that are more crack-like and with higher aspect ratios in the closed state require longer time to close. The time required for the center of a channel to close by a certain degree is related to the square of channel length.

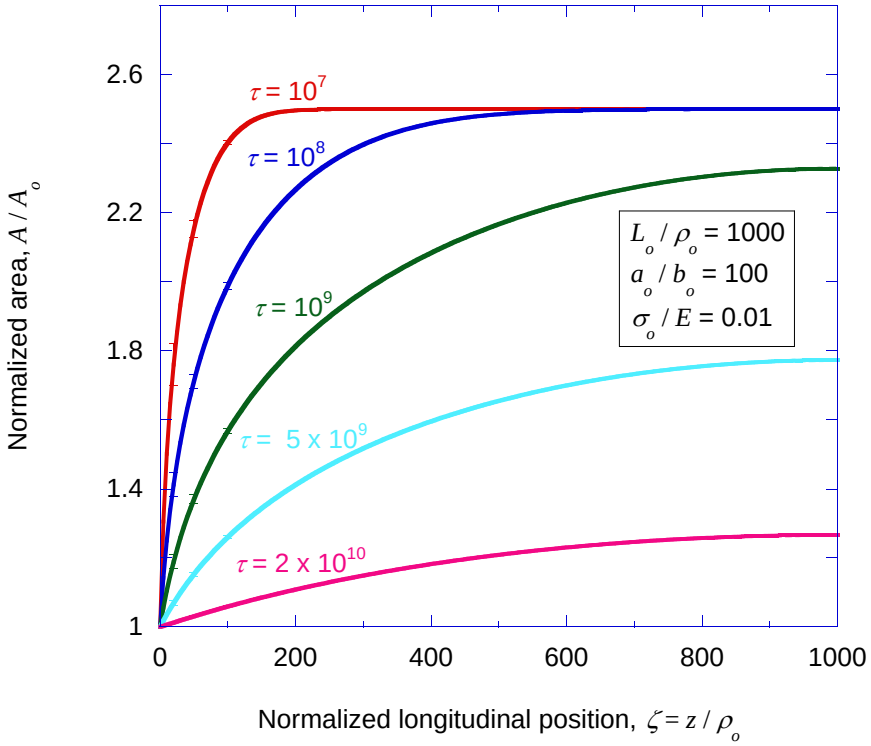

(d)

Figure 3.9: Profiles of channel with an initial aspect ratio of 100 at different times, showing the channel restoring its original closed shape. The major radius (as in (a)) and minor radius (as in (b)) decreases as the fluid flows. They are both smaller near the channel exit. (c) The aspect ratio increases as the fluid flows. (d) The cross-sectional area decreases.

The time scale for a cylindrical or elliptical channel in elastic body to close upon full relaxation of the applied tension was estimated. While the ends of the channel close almost instantaneously, the center of the channel requires much longer time to close given the relatively long length of the channel compared with the other two dimensions. This could be one of the limitations to use extensively long channels for applications of DNA linearization. The analyses and numerical method described in this paper will be appropriate for optimizing the operations to narrow a liquid-filled channel in elastic substrates.

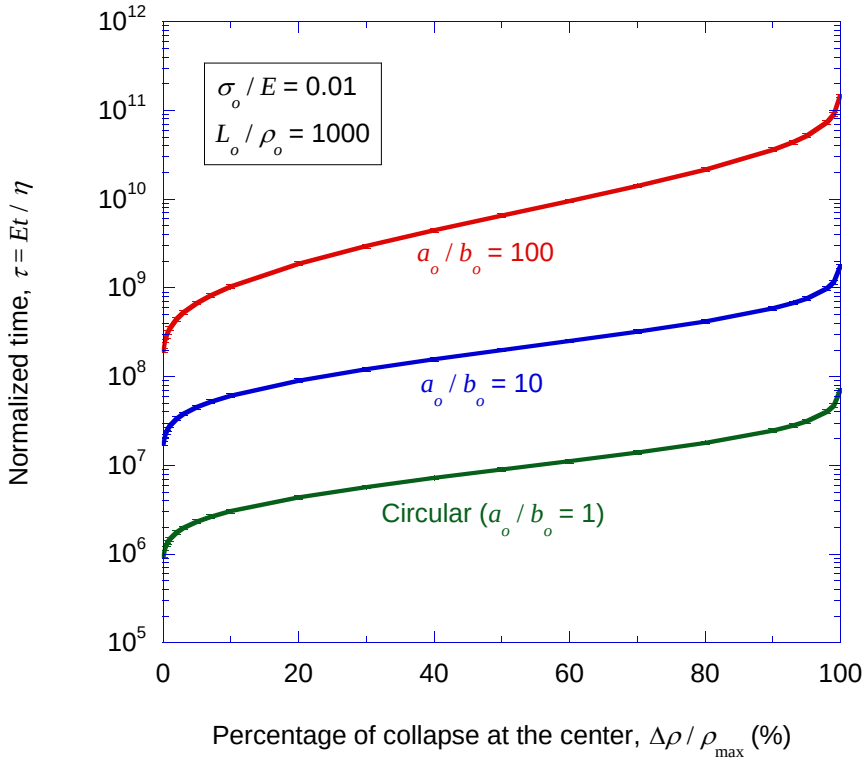

Figure 3.10: Time required for the center of a channel to collapse by certain percentage. Channels with higher initial aspect ratio in the closed state requires longer time for the center to collapse.

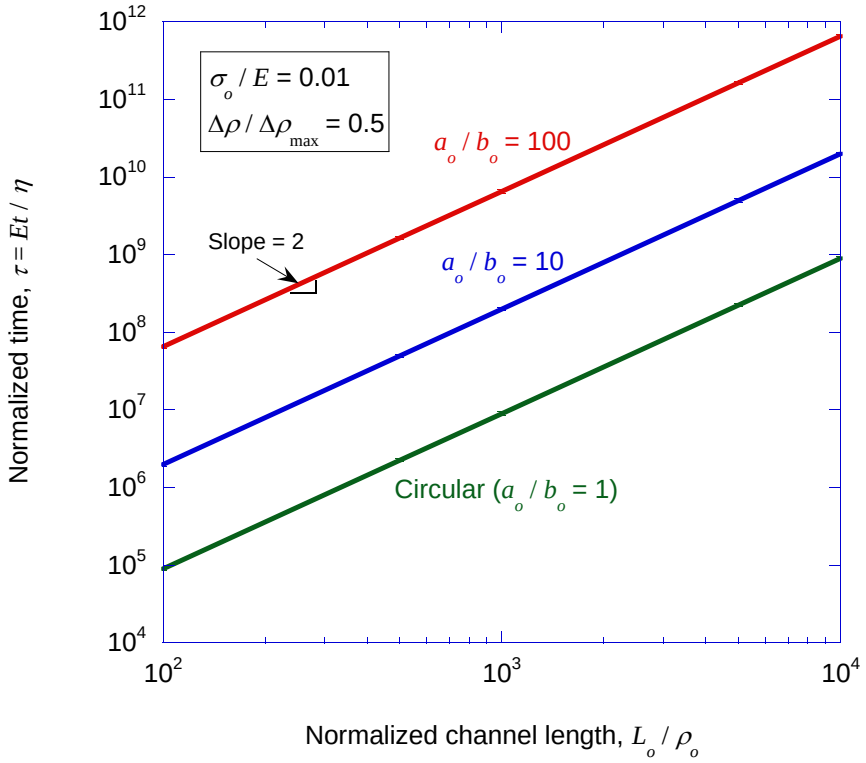

Figure 3.11: Time required for the center of a channel to collapse by $\Delta\rho/\Delta\rho_{\max}$ = 50% given different length of the channel. The time for the center of a channel to collapse is related to the square of length of the channel.

CHAPTER 4

Healing of pores in polymer films

4.1 Introduction

The analyses in this chapter is motivated by the self-healing of Poly(lactic-co-glycolic acids) (PLGAs). PLGA is one of the most used biomaterials today. Since they were first patented in the 1960s, they have been approved by the Federal Drug Administration for use in sutures [56], cardiovascular stents [57–59], skin implants [60, 61] and a plethora of drug delivery devices such as microparticals [9, 10, 12], patches [62], and *in situ* forming gels [11]. Several characteristics make PLGAs attractive for medical applications. They have excellent biocompatibility and their degradation kinetics and mechanical strength along can be easily tailored by altering molecular weight and monomer ratios. In addition, glass-transition temperatures near body temperature result in desirable release behavior of drug-delivery systems, and in enhanced shelf-lives. Despite the prevalent use of PLGAs, the associated scholarly literature rarely includes analyses of their material properties. There have been reports on the moduli of PLGA products, but very little work has been reported on the underlying physics and mechanics of the deformation behavior. Therefore, in the present work, we explore the constitutive properties of PLGA, with a focus on developing a model of the self-healing process in polymers.

Autonomous healing in polymers can be achieved by several different strategies. For example, methods have been developed that rely on an encapsulated healing/filling agent, either in pores or in micro-vascular networks [63–66]. Alternatively, in the absence of significant tensile stresses, voids and cracks in many materials can heal as a result of creep / viscous flow driven by surface tension. This process requires no chemical modification of the material, and relies only on the temperature being sufficiently elevated to ensure flow. This phenomenon can occurs in many different applications from self-healing automotive paints [63], to erasable data storage [67]. The major use of self-healing in PLGAs, is as an

aqueous-based micro-encapsulation method for bio-macromolecules [12].

Porosity can be introduced in PLGAs as a result of phase transitions and associated density changes during curing [68]. In particular, pore networks in PLGA micro-particles can be created by the control of osmotic pressure differences induced by changes in the internal and external environments. Healing of these pores is critical for the quality of the encapsulation and release of drugs and peptides [12,69]. The healing process was explored in a series of model experiments by Mazzara et al. [14] using controlled pores that had been artificially introduced into the surface of PLGA films by blunt-tip micro-needle arrays. These experiments showed empirically that the healing times were controlled by the visco-elastic properties of the PLGA. In this present paper, we extend this work by developing a finite-element model for pore healing. This model assumes that healing proceeds by viscous flow that occurs in response to a deviatoric stress field induced by the surface tension and curvature of the pores. This model can be used to describe pore healing in terms of the temperature and geometry.

4.2 Constitutive models for a linear polymer

The simplest representation of a linear visco-elastic material is known as a Maxwell model. The constitutive behavior corresponding to such a model can be represented by a spring (with a modulus of E_m) in series with a dashpot (with a viscosity of η_m). The dashpot represents a single thermally-activated mechanism for flow, so the viscosity is of the form

$$\eta_m = \eta_{m_o} e^{Q_m/RT} \tag{4.1}$$

where Q_m is the activation energy of the relaxation mechanism leading to flow, R is the molar gas constant, T is the absolute temperature, and η_{m_o} is a material constant. The characteristic relaxation time of a Maxwell model is given by

$$\tau_m = \eta_m / E_m = \tau_{m_o} e^{Q_m/RT} \tag{4.2}$$

A time-dependent modulus, $E(t)$ can be defined for a polymer as the ratio of the stress at a given time t that results from a fixed strain:

$$E(t) = E_m e^{-t/\tau_m} \tag{4.3}$$

The fully-relaxed modulus, which is the time-dependent modulus as $t \to \infty$, of a Maxwell solid is zero. This is important in the present context, because pore healing can only occur when the fully-relaxed modulus is very small.

While a Maxwell model describes some important characteristics of a polymer that exhibits pore healing, polymers generally exhibit more than one relaxation mechanism. Some of these mechanisms may allow for complete relaxation of polymer, others may allow only partial relaxation. Each mechanism will have its own activation energy and characteristic relaxation time, and can be represented by an assembly of elements consisting of linear springs and dashpots. The time-dependent deformation of a polymer can then be modeled as the resultant of such an assembly. The individual moduli and viscosities that go into such a model are determined by fits to the observed response of the polymer at different time scales through experiments such as dynamic mechanical analyses (DMA) and stress-relaxation tests, as described below.

4.3 Role of surface energy and curvature

The chemical potential of an atom or molecule at the surface of a material depends on the product of the surface energy (surface tension) and the local surface curvature. Gradients in this potential provide a driving force for the material to change its shape, either by diffusion of atoms or molecules along the surface, or by bulk deformation in response to deviatoric (shear) stresses established within the body of the material. In the present work, we assume that bulk flow is the dominant mechanism; this is consistent with the experimental results presented later.

The internal stress field associated with a surface (or interface) is established by the change in normal stress across a curved surface, as given by the Young-Laplace equation:

$$\sigma_n = \gamma(\kappa_1 + \kappa_2) \tag{4.4}$$

where γ is the surface tension of the material, and κ_1 and κ_1 are the local principal curvatures. A convex surface results in a compressive normal stress at the surface and a concave surface results in a tensile stress at the surface. The internal stress field induced by surface curvature is exactly equivalent to the stress field induced by applied surface tractions that are normal to the surface and have a magnitude given by Eqn. 4.1. This equivalence

between the stresses induced by surface curvatures and those induced by applied surface tractions forms the basis for the analysis used in this paper.

4.4 Pore healing

The healing of a surface indent is illustrated in Fig. 4.1. The indent is initially formed by the application of a localized external pressure during indentation. This creates large deviatoric stresses to which the polymer responds by rapidly flowing and forming an indent. The effects of surface energy at this stage are relatively small compared to the effects of the indentation stress field, so surface features such as a lip around the indent can often be retained, as shown by microscopy images. (Even when the indentations are square, the surrounding lip is approximately circular). When the indenter is removed, deformation is driven by the deviatoric stress field that is established by the surface tension and curvatures. (A residual stress field resulting from the indentation can also contribute to this deformation; in the present work, we assume this is relaxed by flow during the indentation process.) The resulting stress field can be visualized and modeled by considering equivalent surface tractions, as shown in the schematic of Fig. 4.1. Provided the fully-relaxed modulus is significantly smaller than the stresses induced by the surface curvature, the material can flow to smooth out any surface curvatures. Both the depth of the indent, and the amplitude of any lip formed around the indent will decay over time.

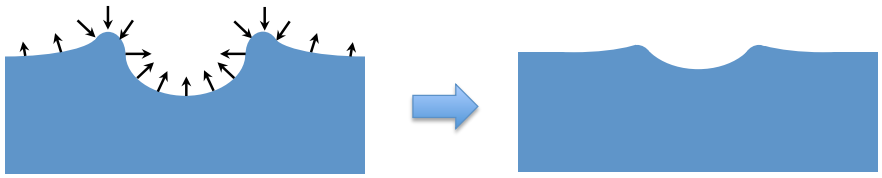

Figure 4.1: A schematic of the healing process showing the shape-recovery of a surface indentation when the entire surface is subjected to stress fields arising from surface tension. The amplitude and direction of surface tension is decided by local curvatures.

For an incompressible linear-viscous material, the deformation field that results from a

deviatoric stress field can be calculated using the Levy-Mises flow rule [70]:

$$\frac{\dot{\varepsilon}_1}{\sigma_1 - 0.5(\sigma_2+\sigma_3)} + \frac{\dot{\varepsilon}_2}{\sigma_2 - 0.5(\sigma_1+\sigma_3)} + \frac{\dot{\varepsilon}_3}{\sigma_3 - 0.5(\sigma_1+\sigma_2)} = \frac{\dot{\tilde{\varepsilon}}}{\tilde{\sigma}} = \frac{1}{3\eta} \tag{4.5}$$

where $\dot{\tilde{\varepsilon}}$ and $\tilde{\sigma}$ are the von-Mises effective strain rate and stress, and and (i = 1,2,3) are the principal strain rates and stresses. In Mazarra et al. [14], this approach was used to develop a simple analytical result for healing an isolated spherical pore in the middle of a viscous material. The Lamé equations [70] for a spherical pore of radius a with an internal pressure of $p = -2\gamma/a$, give principal stresses at a distance r from the center of the pore of

$$\sigma_{rr} = 2\gamma a^2/r^3 \; ; \; \sigma_{\theta\theta} = \sigma_{\phi\phi} = -\gamma a^2/r^3. \tag{4.6}$$

The corresponding principal strain rates are given by

$$\varepsilon_{rr} = \frac{\partial u}{\partial r} \; ; \; \varepsilon_{\theta\theta} = \varepsilon_{\phi\phi} = \frac{u}{r}, \tag{4.7}$$

where u is the radial displacement at a distance r from the center of the pore. Recognizing that at $r = a_o$, $\dot{u}(a) = \dot{a}$, and that at time $t = 0$ the initial pore radius is a_o, it was shown that the pore size is given by

$$a = a_o - \frac{\gamma t}{2\eta} \tag{4.8}$$

So, the time to heal a spherical pore is $2\eta a_o/\gamma$.

4.5 Numerical implementation

In the numerical simulation, the initial pores were assumed to be ellipsoidal, with a depth of b_o, and a half width of a_o on the surface of a film of thickness H_o (Fig. 4.2). The radius of the external boundaries, S_o, were set to a value of $S_o/a_o = 10$ in all simulations. It was demonstrated numerically that this value was always large enough to that its effect was limited to less than a 2% error in the calculated pore depth. The bottom of the film was assumed to be attached to a rigid substrate, but free to expand. The assumption of axisymmetric geometries allowed the calculations to be simplified, while retaining the essential elements of the experimental studies. Furthermore, since the stresses are dependent on local curvatures, there is a very large driving force for any sharp corners to be rounded out. This results in a transition to axisymmetric shapes early in the healing process, so that details of the initial geometry have only a limited effect on the healing time. Indeed, Mazzara et al. [14] reported that their initially square pores quickly became circular. We

used our numerical method to analyze cylindrical pores, and they evolved fairly quickly into ellipsoidal shapes. However, the initial sharp corners in a cylindrical void required a very dense mesh. Therefore, ellipsoidal geometries were used to model the pores.

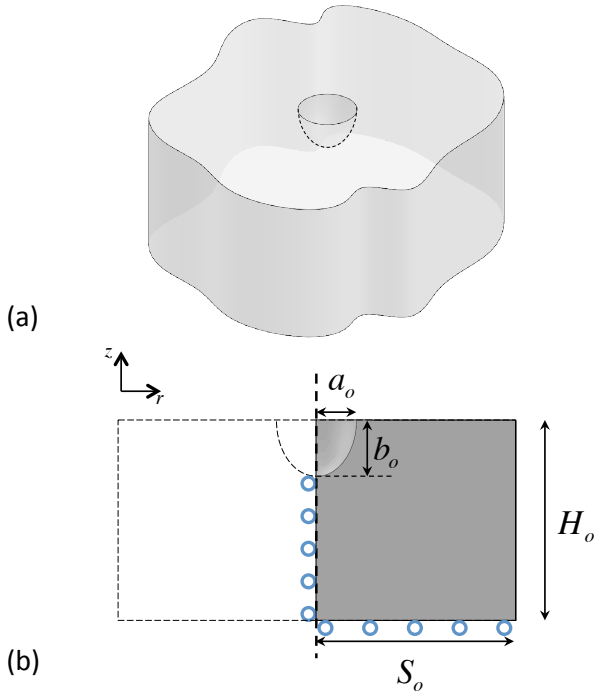

Figure 4.2: a) A schematic illustration of an axisymmetric ellipsoidal surface pore. b) The geometry of the axisymmetric specimen used in the numerical simulations. The boundaries are located at an outer radius of S_o, which is big enough so that the pore can be considered as an isolated pore. The thickness of the substrate is H_o. The bottom symmetry plane models free sliding on a rigid substrate.

Finite-element analyses were conducted using the commercial package ABAQUS. The stress fields resulting from the surface tension were induced in the finite-element model by applying tractions to the surface proportional to the sum of the principal curvatures (Eqn. 4.4). A numerical technique for calculating the curvatures has been described by Henann et al. [71]. We used a similar approach to calculate the curvatures of the axisymmetric surfaces. Such a surface can be described by $z = Z(r)$, where z is the height above an arbitrary reference value, and r is the distance from the axis of symmetry. The sum of the

two principal curvatures (twice the mean curvature) at any point on the surface is given by

$$2\kappa = \kappa_1 + \kappa_2 = \frac{\partial^2 Z/\partial r^2}{(1+(\partial Z/\partial r)^2))^{3/2}} + \frac{\partial Z/\partial r}{r(1+(\partial Z/\partial r)^2)^{1/2}}. \tag{4.9}$$

Thus, the calculation is reduced to a two-dimensional problem. The coordinates of an integration point A (r_A, z_A), and the coordinates of its two nearest neighboring integration points, B (r_B, z_B) and C (r_C, z_C), can be fitted to a parabola ($y'/y_o = x'^2$) in terms of a local coordinate system with an origin located at point A and aligned with the local normal direction. The sum of the principal curvatures at A is then given by

$$2\kappa = 2y_o - n_r/r \tag{4.10}$$

where n_r is the radial component of the outward normal vector at A. This procedure was used to calculate the mean curvature at all points on a surface, and then corresponding surface tractions. A DLOAD user-subroutine was developed accordingly and was incorporated in ABAQUS/Standard. The user-subroutine code can be found in Appendix A. The user-subroutine was verified using the simple geometries of a sphere and a cylinder. Mesh and boundary sensitivity studies were conducted empirically by changing the size of the mesh and distance to remote boundaries, and verifying that any influence on the results was significantly less than uncertainty associated with the measurements of the material parameters.

4.6 Material preparation

PLGA 50:50 with lauryl-ester-terminated chains, with a weight-averaged molecular weight of 55.3 kDa, and average inherent viscosity of 0.61 dL/g was provided by Lactel Inc. Details of the preparation of the PLGA films are reported by Mazzara et al. [14]. Briefly, the polymer was dissolved in acetone (27% w/w) and spin-coated onto a Teflon-coated glass substrate. The films were then dried for one day in a fume-hood, and then for an additional day under vacuum to remove excess solvent. When the films were separated from the glass substrate they had a final thickness of 16 ± 3 μm.

4.7 Material characterization

4.7.1 Stress relaxation tests

Dry films were cut into rectangular specimens of approximately 10 mm in width and 30 mm in length. Stress-relaxation tests were conducted in a temperature range of 40 °C to 65 °C using a TA Instruments RSA3 dynamic mechanical analyzer. The samples were placed in the grips at room temperature and heated to the desired temperature at 100 °C/min. One minute was allowed for the temperature to stabilize before a strain of 3 % was applied within 5 ms. The strain was held constant, and the corresponding stress was then measured every 0.01 second.

4.7.2 Dynamic mechanical analysis

The same instrument was used to measure the visco-elastic properties of the PLGA films by dynamic mechanical analysis (DMA). Samples were tested in uniaxial tension at a frequency of 1 Hz, with a strain amplitude of 0.1% and an initial mean force of 0.01 N. The storage modulus, E', loss modulus, E'', and loss tangent, $\tan\delta$, were measured over a temperature range of 25 °C to 70 °C, with a temperature ramp-up rate of 3 °C /min and a soak time of 30 seconds to reach steady state at each temperature. Three identical samples were analyzed to determine representative values and uncertainties.

Frequency sweep tests in the range of 0.001 Hz to 99 Hz with a strain amplitude of 0.1% were then conducted in a temperature range of 25 °C to 65 °C. The mean strains in these cyclic tests were set to be 25 % greater than the strain amplitudes to ensure that the specimen never went into compression. The storage modulus, loss modulus and $\tan\delta$ were determined as functions of frequency.

4.7.3 Measurement of interfacial tension

The interfacial tensions of the PLGA films were determined by placing a drop of miliQ ultrapure water on the films and using a goniometer to measure the polymer-water contact angle. Contact angles for each film were measured in three distinct locations, and a minimum of two films were used for each sample. The contact angles were converted to

interfacial tensions using Berthelot's combining rule [72]

$$\cos\theta = -1 + 2\sqrt{\frac{\gamma_{sv}}{\gamma_{lv}}} \tag{4.11}$$

where θ is the contact angle, and γ is the interfacial tension between solid (s) and vapor (v).

4.7.4 The effects of annealing and solvent escape kinetics

To investigate the effects of annealing and annealing time on the visco-elastic properties of the PLGA, films were incubated at three temperatures (50 °C, 55 °C and 65 °C) above the glass-transition temperature, T_g. for various times. The properties of these films were tested using DMA and relaxation tests, as described above.

To quantify the kinetics of annealing and solvent escape, the films were subjected to thermo-gravimetric analysis (TGA). Approximately 20 mg of PLGA was placed on platinum pans and quickly heated (50 °C/min) to 50 °C, 55 °C and 65 °C. The films were held isothermally for 8 hours and the percent change in mass was recorded.

4.8 Validation of finite-element model

Equation 4.8 gives the analytical solution for the radius of a spherical pore in an infinite body of an incompressible Maxwell solid as a function of time. As a check on the validity of our numerical technique, we repeated this calculation numerically, using the finite-element model discussed above. A comparison between the simulation and the analytical results is presented in Fig. 4.3, showing that the finite-element model gives the expected result. It should be noted that, in this case, the numerical calculations suffer from excessive distortion of the mesh when the pore is very small, owing to the huge normal stresses acting at the surface. For this reason, the numerical calculations shown in Fig. 4.3 could not be taken all the way to complete pore healing.

4.9 Numerical results for surface pores

Figure 4.4 shows how the depth of an initially ellipsoidal surface pore evolves with time for a Maxwell material. Figure 4.5 shows representative snapshots of the mesh during healing corresponding to the case with $a_o/b_o = 1$ in Fig. 4.4. It should be noted that, in contrast

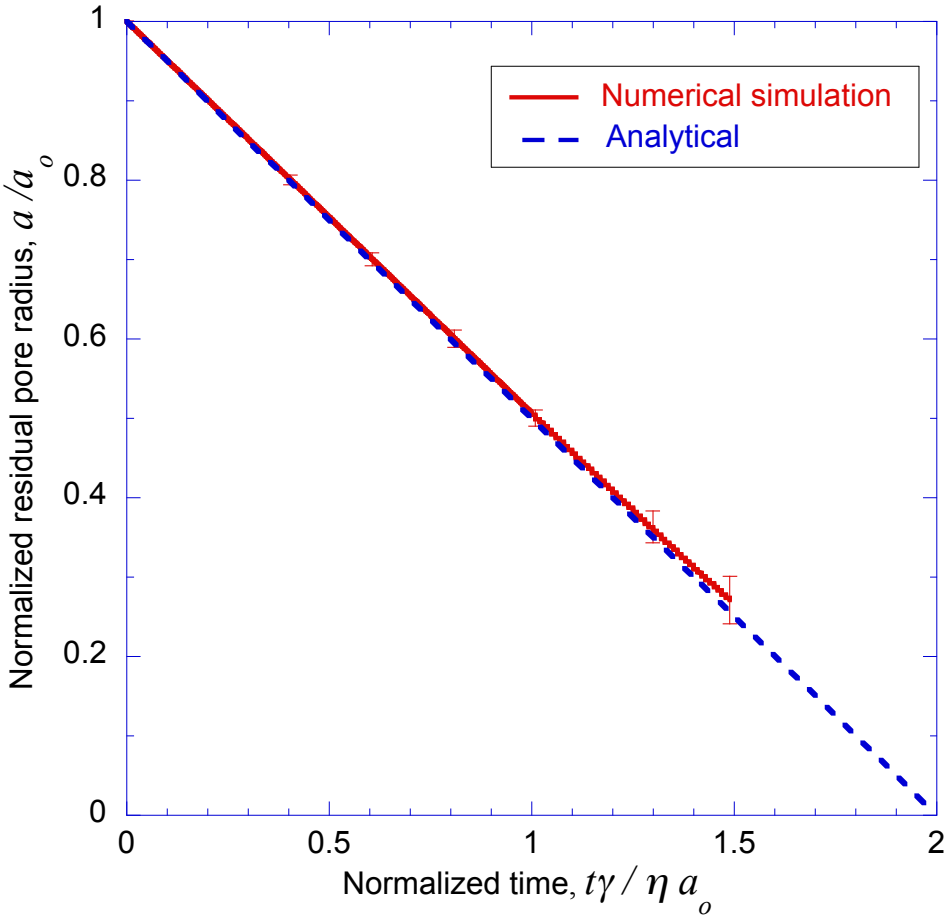

Figure 4.3: The results of a numerical calculation of the healing time of a spherical pore in infinite visco-elastic body agree with the analytical results. The numerical results are affected by the excessive distortion when the residual radius of the pore is small, resulting in larger uncertainties, as represented by the error bars.

to the healing of a spherical pore inside a polymer, the depth of the pore goes to zero only asymptotically. There is no well-described healing time. Instead, the healing time has to be defined in terms of how long a pore takes to heal to a given percentage of its original depth. Experimentally, this will be the depth at which the pore can no longer be distinguished. We use a fixed percentage of 85% to define healing in the numerical simulations, since this corresponds to the point at which the healing rate starts to decay markedly. This arbitrary definition introduces a systematic error into absolute comparisons with experimental data

for healing times; however, it is expected that relative comparisons will be unaffected.

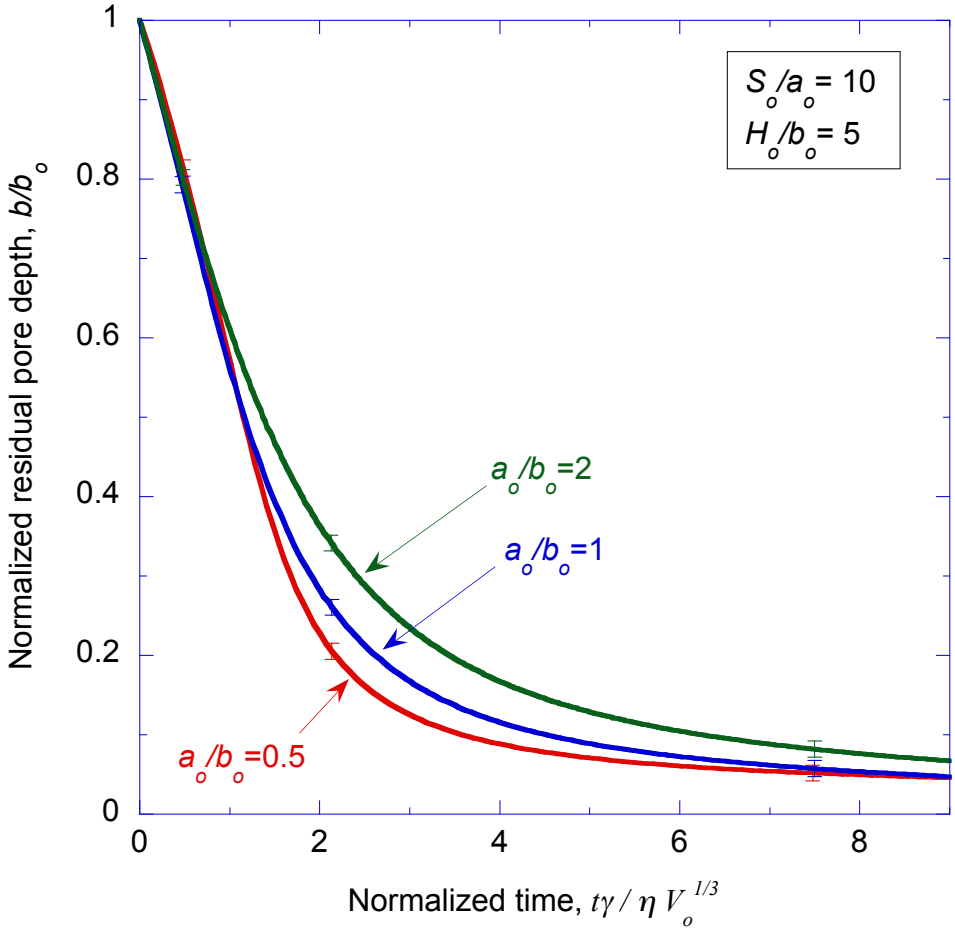

Figure 4.4: Numerical results for how the residual depth of an ellipsoidal surface pore in a Maxwell material varies as a function of time show that healing slows down as the pore depth decreases. In this plot, the time, t, has been normalized by the surface tension, γ, the viscosity, η, and the initial volume of the pore, V_o. At very long times, the normalized curves collapse and approach zero asymptotically. Wider and shallower pores, of the same initial volume require longer times to reach the same level of healing. The error bars on these plots correspond to numerical uncertainties associated with mesh size.

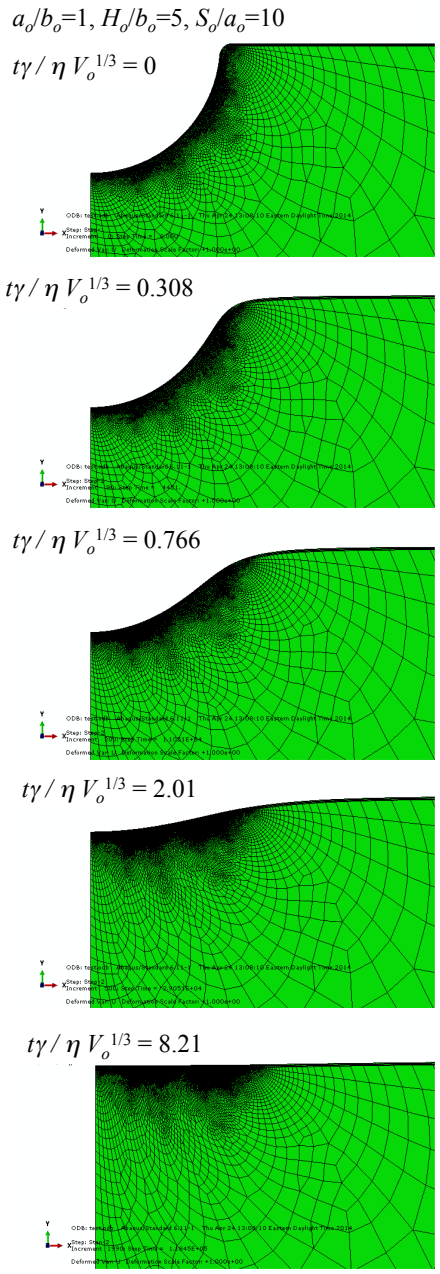

Figure 4.5: The mesh of finite element analysis showing the evolving profile of a surface pore during healing. These pictures correspond to the case with $a_o/b_o = 1$ in Fig. 4.4

4.10 Effect of temperature on healing of wet films

We did not have the capability to do DMA and stress-relaxation tests in an aqueous environment. However, the results presented by Mazzara et al. [14] for the healing of pores in wet films as a function of temperature were used as a preliminary validation of the physics

of the model. An activation energy of 193 kJ/mol for the viscosity of the wet PLGA films was found by fitting the healing data to an Arrhenius plot in Ref. [14]. This value of activation energy was then used in the finite-element calculations, with a representative value of Young's modulus $E = 1$ GPa. (This choice of modulus was not important for the calculations, but it is consistent with the measured value for a dry PLGA film, as described later.)

The pores in the wet PLGA had an initially square cross section, and an initial width to depth ratio of $a_o/b_o = 5/14$. By fitting the observed healing time for these pores at 53 °C to the numerical predictions for elliptical pores with the same aspect ratio to heal to 85%, and using the activation energy of 193 kJ/mol for the viscosity, a value for γ/η_o could be determined as $7.9 \pm 2.3 \times 10^{21}$ m/s. This fitted value of γ/η_o was then used in conjunction with the activation energy of 193 kJ/mol for the viscosity to calculate the healing time for identical pores over a range of temperatures. A comparison between the predicted healing times and the temperature are shown in Fig. 4.6.

The role of the initial aspect ratio and volume on healing time was also investigated in Ref. [14]. The material parameters described above, were incorporated into a finite-element calculation and used to predict the healing time (again, defined as an 85% reduction in depth) for different shaped pores. These predictions are shown in Fig. 4.7, and compared with the experimental observations. It should be emphasized that this comparison, unlike that of Fig. 4.6, does not reflect any fits to the data. Therefore, the reasonable agreement between the predictions and experimental results provides support to the modeling.

4.11 Measurement of properties for dry PLGA films

4.11.1 Stress relaxation

In the study described above, the material properties for wet PLGA films were determined from fits to experimentally observed data, and then used to calculate pore healing. While this shows consistency between the model and the experimental observations, a much more important question is whether it is possible to measure the material properties independently of the pore healing experiments, use these properties in a numerical model and predict the behavior. This was the goal of the studies on the dry PLGA films for which it was possible to measure the properties.

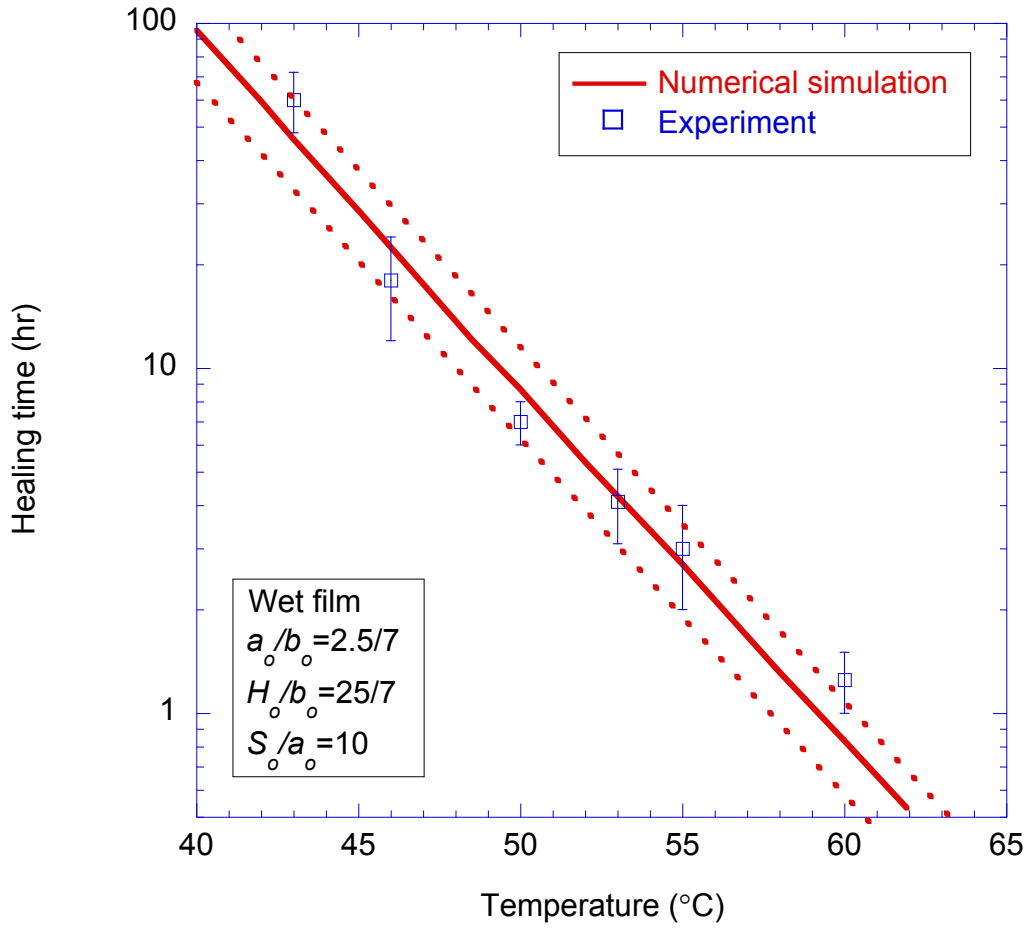

Figure 4.6: A comparison between the calculated time to heal pores in a wet PLGA film and the experimental observations of Mazzara et al. [19], as a function of temperature. The time to heal a surface pore in a wet film above the glass transition temperature of T_g = 23.4 ± 0.4 °C by viscous flow depends on the temperature. The geometrical parameters of the ellipsoidal pore used in the numerical calculations were $a_o/b_o = 5/14$, $S_o/a_o = 10$, and $H_o/b_o = 25/7$. These were consistent with the experimental geometries which had pores with an initially square cross section. The material properties were chosen to fit the experimental results at 53 °C, and an activation energy of 193 kJ/mol for the viscosity had been estimated from an Arrhenius fit to this data [14]. The uncertainty in the numerical simulations (represented by the dashed lines) match the uncertainty from the experimental results at 53 °C.

An initial assumption that the PLGA behaves as a simple Maxwell solid with a time-dependent modulus as in Eqn. 4.3, where the time constant τ_m was defined in Eqn. 4.2. A

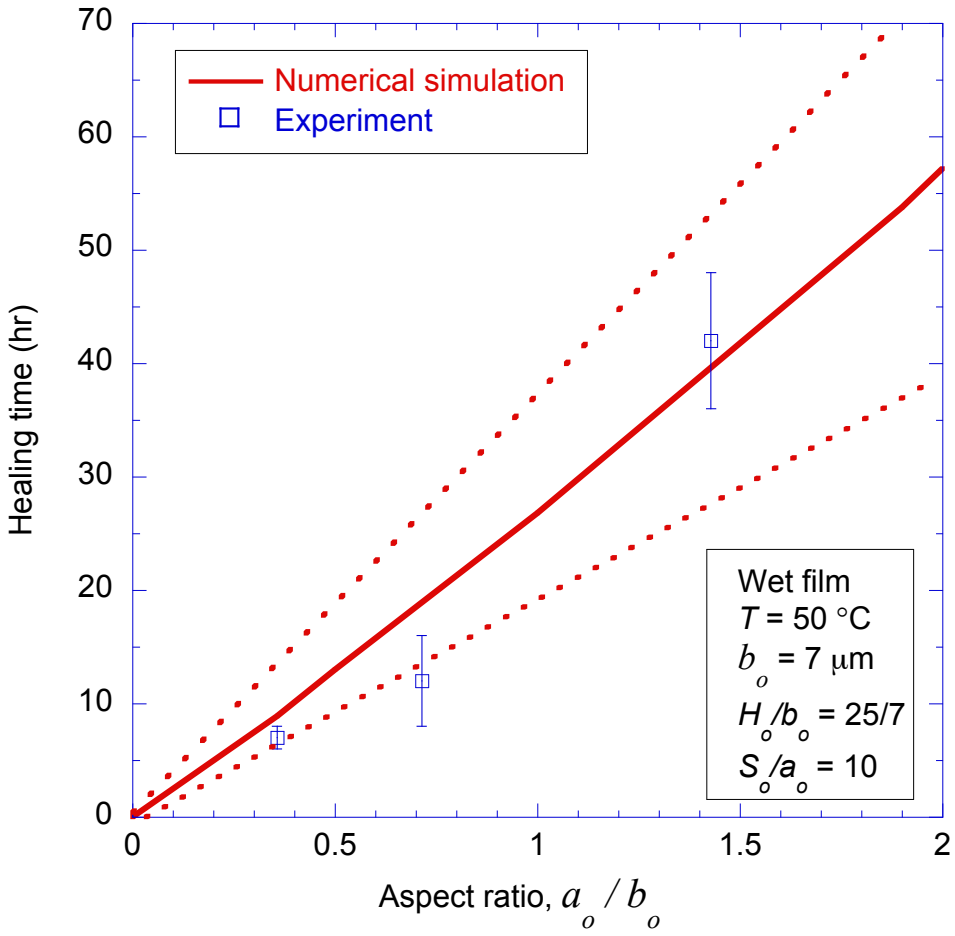

Figure 4.7: A comparison between the predicted effects of pore volume and aspect ratio on healing time, and the observed effects. The comparison shows quite good agreement. The experimental data were presented in Mazzara et al. [14], and the parameters for the numerical studies were identical to those used for Fig. 4.6. The uncertainty in the numerical simulations (represented by the dashed lines) comes from the uncertainties to the fit in Fig. 4.6.

log-linear plot of stress against time, from stress-relaxation experiments should then be of the form of a single line with a slope of $-\tau$.

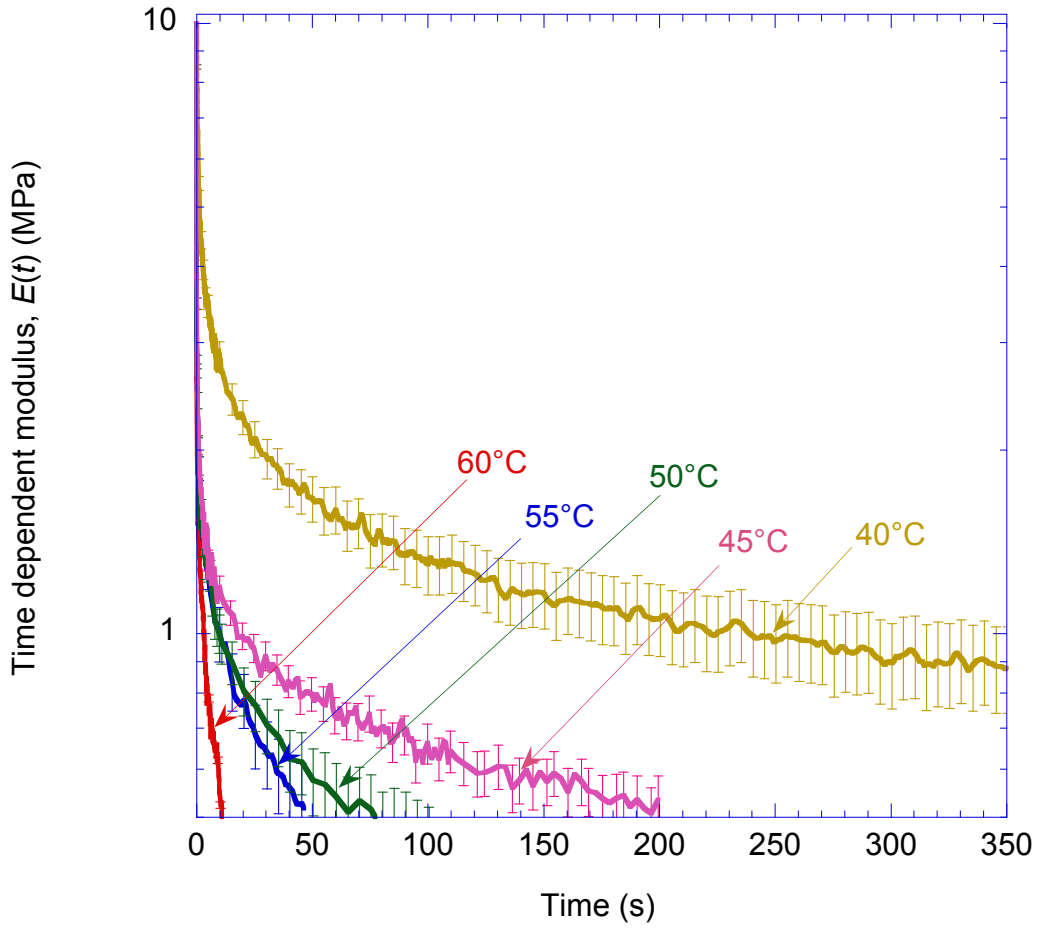

Figure 4.8: Sample data of stress relaxation tests for dry PLGA films at different temperatures for an initial strain of 3%, using a TA Instruments RSA3 dynamic mechanical analyzer. While a single thermally-activated relaxation should exhibit a single slope, the initial rapid drop indicates an additional rapid relaxation mechanisms. These stress relaxation data were used to measure the slower relaxation occurring at longer time scales. The accuracy of modulus below 0.5 MPa is limited by the resolution of the machine. The constant slope at longer time scales starts when the time-dependent modulus reaches 1.5 ± 0.5 MPa.

The results from the stress-relaxation experiments are shown in Fig. 4.8 for a temperature range of 40 °C to 65 °C. These plots show a very fast initial relaxation of modulus followed by a slower decrease. This indicates more than one relaxation mechanism. If we assume that the PLGA is a linear polymer, then this initial rapid drop indicates at least one

additional relaxation mechanism with a relatively short time constant. The time constant for this fast relaxation is too small to be extracted reliably from the stress-relaxation data in Fig. 4.8; however, it was explored by means of DMA, as described later. At longer time scales, there appears to be one dominant mechanism that gives a constant slope to the stress-relaxation curves. The slopes of these lines corresponding to different temperatures were determined by a least-squares fit process, and plotted on an Arrhenius plot in the form of $\log(\tau)$ against $1/T$ in Fig. 4.9. The slope of this line indicates an activation energy of $Q_m = 206 \pm 6$ kJ/mol and a pre-exponential term of $\tau_{m_o} = \eta_{m_o}/E_m = 6.4 \pm 0.2 \times 10^{-32}$ s. It can be observed that at all temperatures, the constant slope at long time scales starts when the time dependent modulus is in the range of 1 to 2 MPa with an average value of 1.5 ± 0.5 MPa. If we model this dominant mechanism at long time scales with a Maxwell model, the initial modulus is $E_m = 1.5 \pm 0.5$ MPa, and the Maxwell dashpot has $\eta_{m_o} = 9.6 \pm 3.5 \times 10^{-32}$ MPa s and $Q_m = 206 \pm 6$ kJ/mol.

4.11.2 Dynamic mechanical analysis

The storage modulus and loss tangent for dry PLGA films computed from DMA temperature-sweep tests at 1 Hz are plotted in Fig. 4.10. From this plot, the instantaneous modulus is estimated to be 1.6 ± 0.3 GPa, which is the asymptotic level that the storage modulus tends to at low temperatures. It will be noted from Fig. 4.10 that the peak in $\tan\delta$ is a double peak. The first peak is at about 38 °C, which is consistent with the estimate of Mazzara et al. [14] for a glass-transition temperature of between 35 °C and 40 °C. In this paper, we will neglect the fine details of the relaxation peak, and assume a single relaxation mechanism that operates at 1 Hz over the temperature range of 38 °C to 48 °C.

To extract the visco-elastic properties of the relaxation mechanisms that caused the fast initial relaxations observed in the stress relaxation tests, we conducted frequency sweep tests. Representative frequency sweep test results can be found in Fig. 4.11. The frequency sweep tests shows a single peak in loss modulus and can be interpreted based on a standard linear solid (SLS). An SLS has a Maxwell arm in parallel with a spring, and has a time-dependent modulus in the form of [73]

$$E(t) = E_r + E_s e^{-t/\tau_s} \,. \tag{4.12}$$

In this equation, the fully-relaxed modulus $E(\infty)$ is given by E_r, and the unrelaxed modulus, $E(0) = E_r + E_s$. The temperature-sweep tests gave a value for this unrelaxed modulus

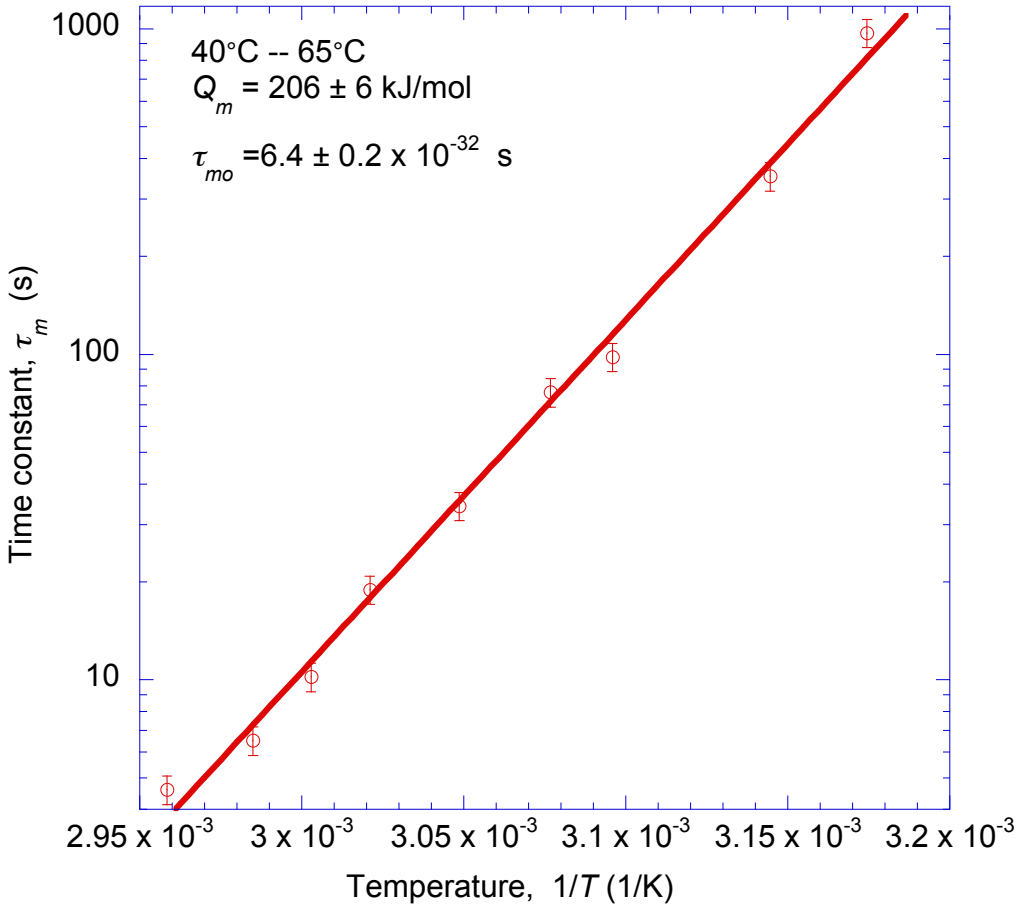

Figure 4.9: The time constant, τ_m, decreases as the temperature, T, increases. An Arrhenius plot of relaxation time against $1/T$ shows an activation energy of 206 ± 6 kJ/mol for the viscosity term responsible for the slow relaxation in the temperature range of 40 to 65 °C. The data also indicate that the pre-exponent for the time constant (Eqn. 4.2) is given by $\tau_{m_o} = 6.4 \pm 0.2 \times 10^{-32}$ s.

of $E(0) = 1.6 \pm 0.3$ GPa.

A standard-linear solid also has a viscosity of the form $\eta_s = \eta_{s_o} \exp(Q_s/RT)$, where Q_s is the activation energy and η_{s_o} is a material constant. The storage modulus, $E'(\omega)$, and

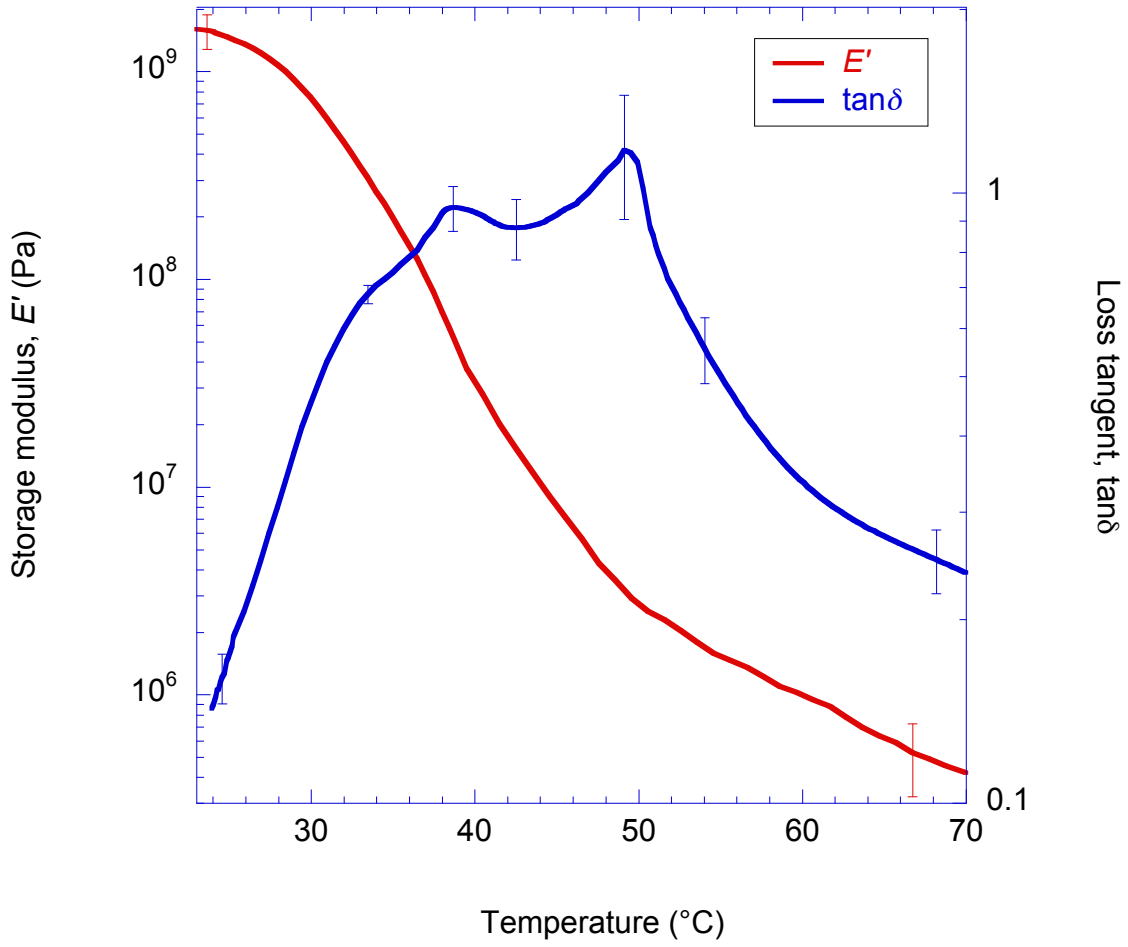

Figure 4.10: Results from DMA showing the storage modulus and loss tangent as functions of temperature for dry PLGA films. The tests were conducted at a constant frequency of 1 Hz. Three samples were tested, and the average value has been plotted. The double peaks in $\tan\delta$ indicate at least two relaxation mechanisms with similar time constants in the temperature range, which can be approximated by one equivalent dashpot. The unrelaxed storage modulus is estimated to be 1.6 ± 0.3 GPa.

loss modulus, $E''(\omega)$ of an SLS are in the form [73]:

$$E'(\omega) = E_r + E_s \frac{\omega^2 \tau_s^2}{1 + \omega^2 \tau_s^2} \tag{4.13}$$

$$E''(\omega) = E_s \frac{\omega \tau_s}{1 + \omega^2 \tau_s^2} \tag{4.14}$$

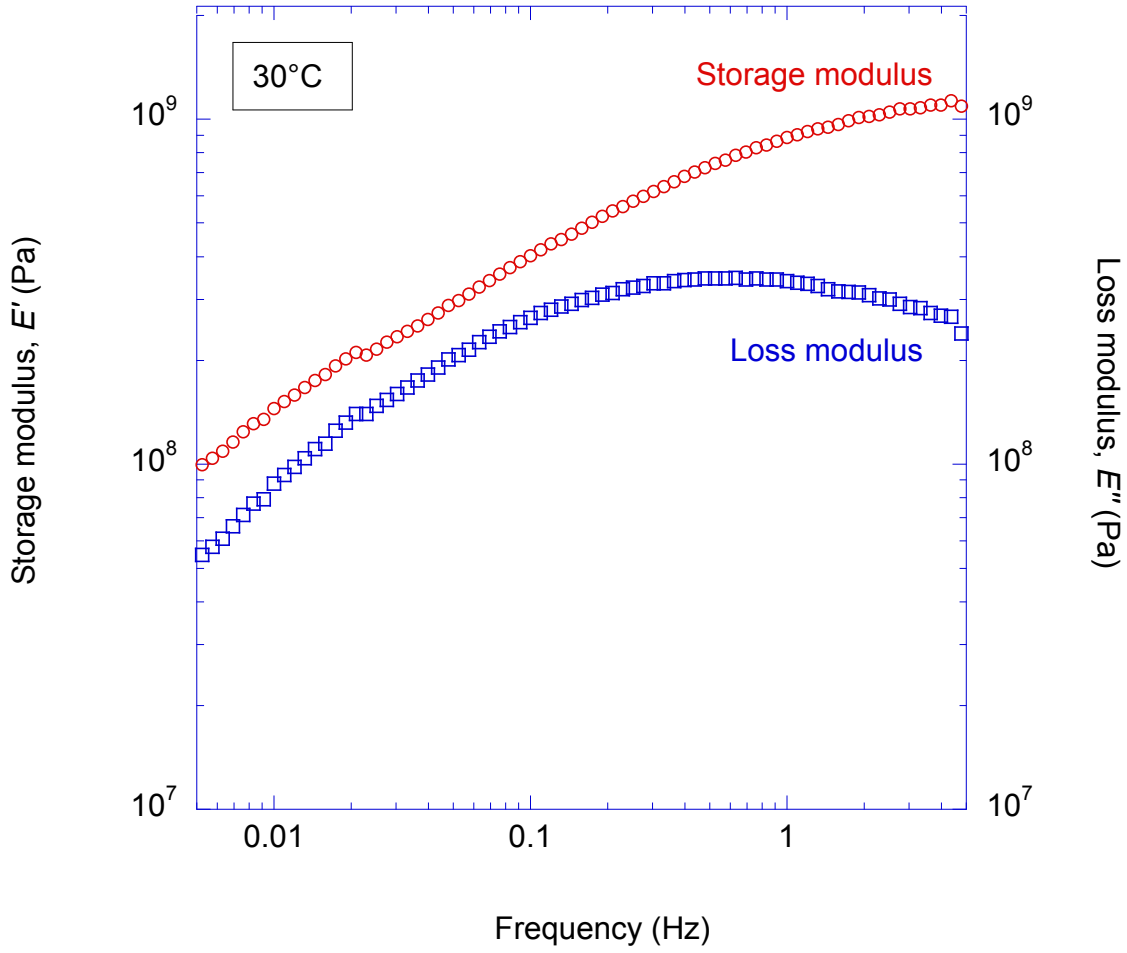

Figure 4.11: Representative results from DMA frequency sweep test showing the storage and loss modulus as functions of frequency for dry PLGA films at 30 °C. The loss modulus presents with a single peak within the range of frequency analyzed, and can be interpreted based on a standard linear solid model. The time constant can be calculated from the peak in the loss modulus.

where ω is the angular frequency of the input strain, and the time constant $\tau_s = \eta_s / E_s$. The loss modulus is a maximum at $\omega = 1/\tau_s$, so the time constants at different temperatures can be extracted from the peaks in the loss modulus and plotted on an Arrhenius plot in Fig. 4.12. The activation energy of the SLS dashpot was estimated to be $Q_s = 250 \pm 29$ kJ/mol and the pre-exponential term was $\tau_{s_o} = 6.6 \pm 0.8 \times 10^{-44}$ s.

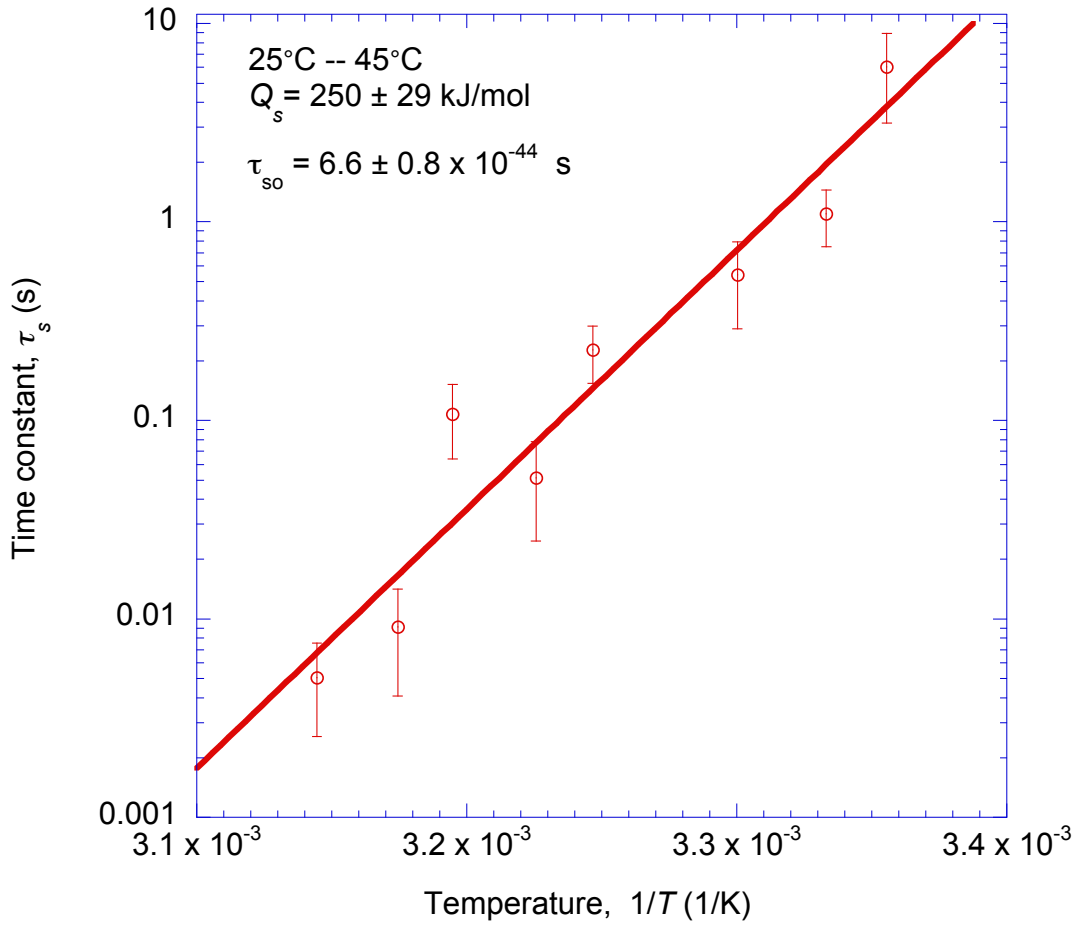

Figure 4.12: The time constant of standard linear solid decreases as the temperature, T, increases. An Arrhenius plot shows an activation energy of 250 ± 29 kJ/mol for the fast relaxation. The pre-exponent for the time constant (Eqn. 4.2) is given by $\tau_{m_o} = 6.4 \pm 0.2 \times 10^{-32}$ s.

The fully-relaxed modulus, E_r, of an standard-linear solid can be determined from the difference between the storage and loss modulus at the frequency corresponding to the maximum loss modulus (Eqn.4.14). In the present cases, there was a slight dependence of the relaxed modulus on temperature, as shown in Fig 4.13. This indicates the presence of additional fast relaxation mechanisms, which are ignored in the present analysis. However, the relaxed moduli measured from the peaks in the loss modulus are consistent with the value of 1.5 ± 0.5 MPa determined from the stress-relaxation experiments for E_m.

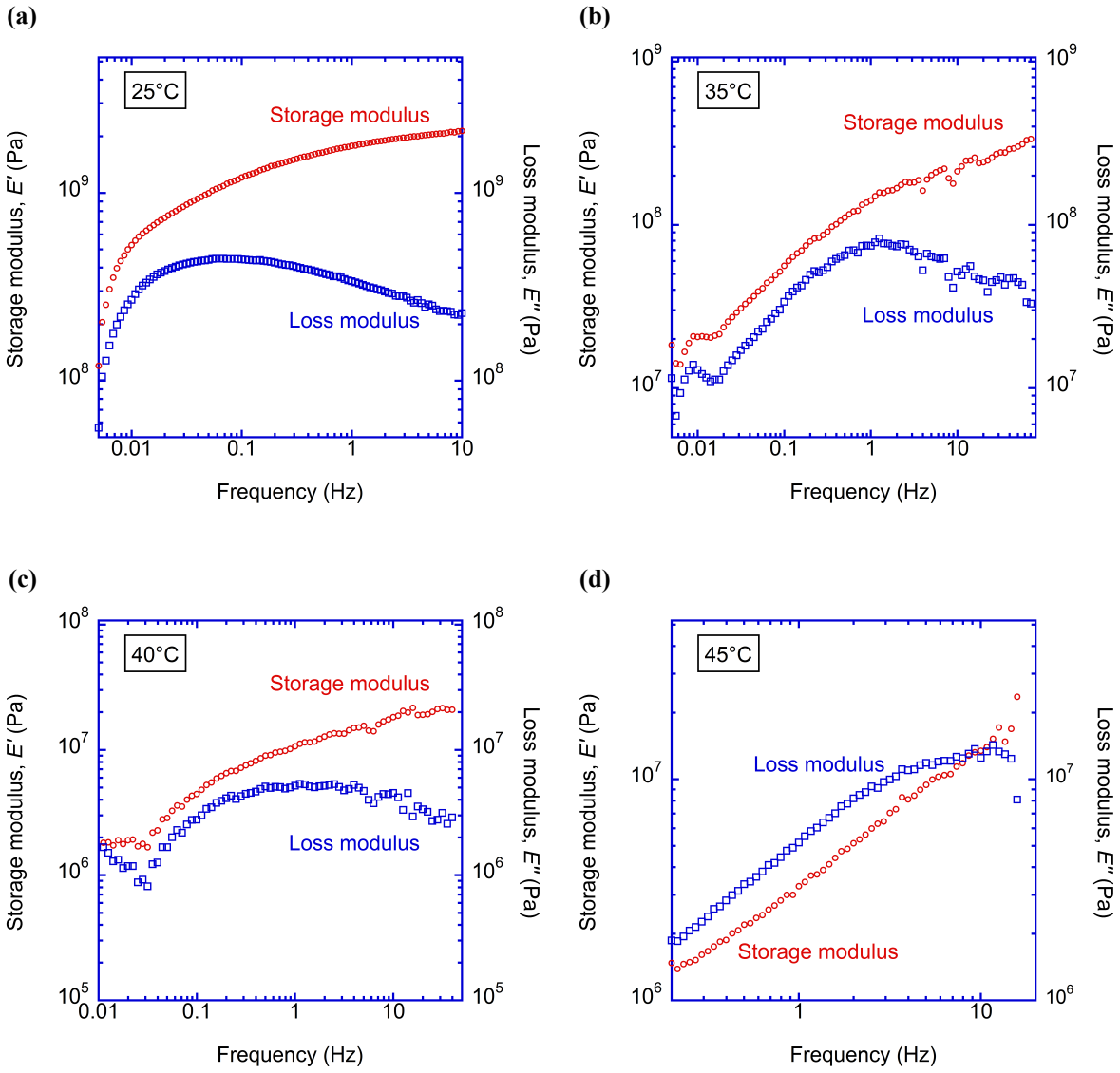

Figure 4.13: Representative results from DMA frequency sweep test showing the storage and loss modulus as functions of frequency for dry PLGA films at 25, 35, 40 and 45 °C. Time constant can be extracted from the peaks in the loss modulus at each temperature. There was a slight dependence of the relaxed modulus on temperature.

Combining the results from the stress relaxation tests and the frequency sweep tests, we propose a material model for dry PLGA film as shown in Fig. 4.14(a). The model consists of a standard linear solid in series with a dashpot, and has a time-dependent modulus of

$$E(t) = (E_r + E_s e^{-t/\tau_s}) e^{-t/\tau_m} \,. \tag{4.15}$$

In this model, the standard-linear solid provides a time-dependent initial modulus for the Maxwell dashpot. The instantaneous modulus is $E(0) = E_r + E_s$ which has a value of 1.6 ± 0.3 GPa from the frequency sweep test. The fully-relaxed modulus E_r of the SLS was chosen to be the initial modulus for the Maxwell dashpot estimated from the stress relaxation results. The parameters are summarized in Table 1. The Maxwell dashpot with a viscosity of η_m dominates the healing process and is the one we are particularly interested in when analyzing the healing process. The SLS dashpot with a viscosity, η_s is associated with relaxing 99.9% of the instantaneous modulus, however has no significant effect on healing.

Table 4.1: Values of parameters of the unannealed dry PLGA (see Fig. 4.14)

E_s (MPa)	$(1.6 \pm 0.3) \times 10^3$
E_r (MPa)	1.5 ± 0.5

	η_o (MPa s)	Q (kJ/mol)
η_s	$(1.1 \pm 0.3) \times 10^{-40}$	250 ± 29
η_m	$(9.6 \pm 3.5) \times 10^{-32}$	206 ± 6

When the model is used in a finite-element code, it needs to be converted to the form shown in Fig. 4.14(b), which is the equivalent Prony-series representation. In this figure, $E_1 = E_s$, $E_2 = E_m$, $\eta_1 = (1/\eta_s + 1/\eta_m)^{-1}$, and $\eta_2 = \eta_m$. A Prony series representation requires a non-zero fully-relaxed modulus. Therefore, an arbitrary value of E_3 was chosen sufficiently low that would it not impede the healing to any level of completeness that were we interested in.

4.11.3 Interfacial tension for dry PLGA

The contact angle was measured to be 71.8 ± 1.4 °. Using the Berthelot's combining rule and a water-air interfacial tension of 72.7 mN/m , the surface energy of dry PLGA films were calculated to be $\gamma_{sv} = 31.0 \pm 2.0$ mN/m.

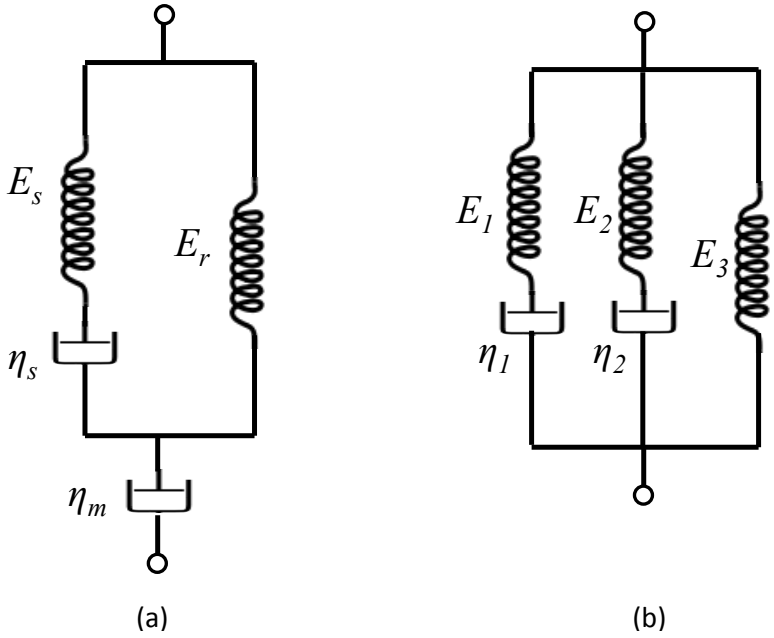

Figure 4.14: Proposed material model for PLGA. (a) The model consists of a standard linear solid in series with a dashpot. The standard linear solid series provide a time-dependent initial modulus for the lower dashpot. The material has a fully-relaxed modulus of zero, ensuring complete healing to occur. The lower dashpot is the dominant relaxation mechanism at longer time scales. (b) The equivalent model used as a Prony series for finite element calculations in ABAQUS, with $E_1 = E_s$, $E_2 = E_r$, $\eta 1 = (1/\eta_s + 1/\eta_m) - 1$, and $\eta_2 = \eta_m$. E_3 was arbitrarily chosen for the implementation of the Prony series, and was sufficiently small so as not to impede complete healing.

4.12 Prediction on healing times for pores in dry PLGA fims

Finite-element calculations of pore healing in dry PLGA films using the material properties described above were performed assuming axisymmetric ellipsoidal pores with an aspect ratio, $a_o/b_o = 2.5/7$, and a pore volume of 91.6 μm^3. This aspect ratio and volume are appropriate for the values used in the experimental study [14]. The predicted healing times are plotted as a function of temperature in Fig. 4.15, along with the experimental results. Three different contours of different healing levels are plotted in Fig. 4.15, showing the effect of small changes in the amount of pore closure used as a measure of healing.

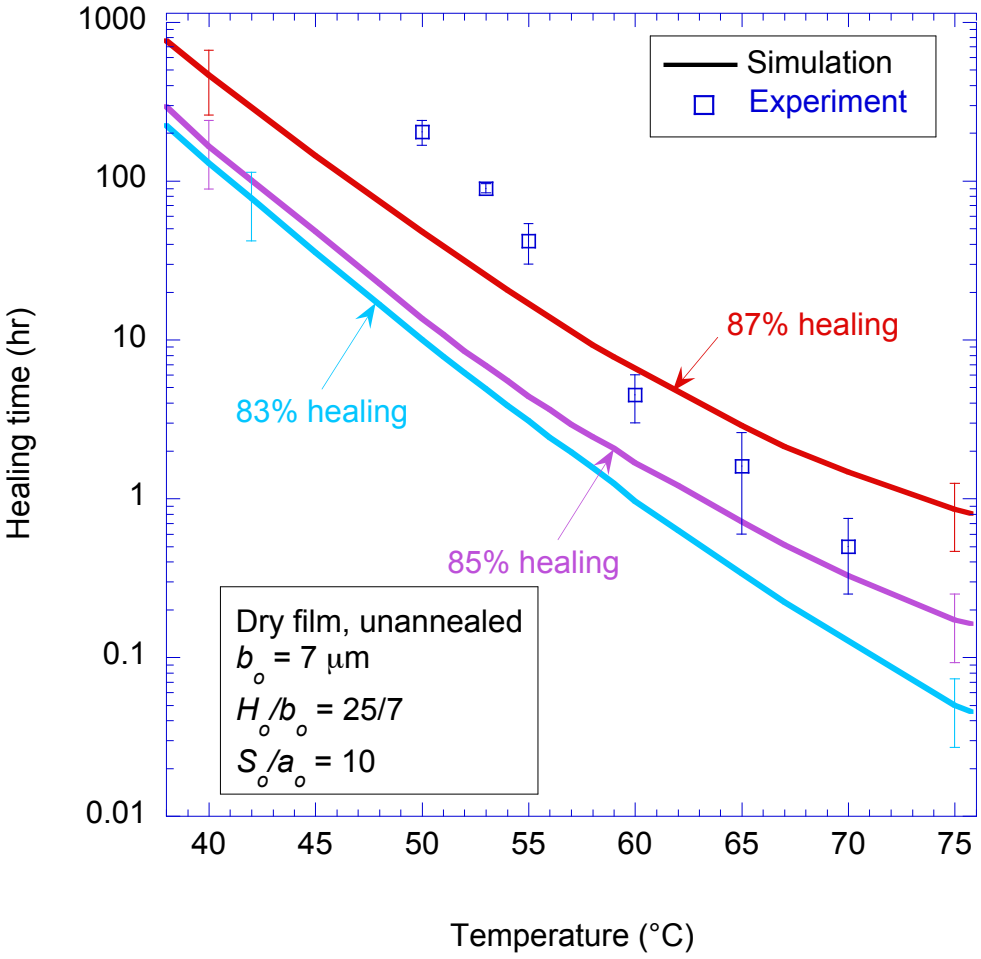

Figure 4.15: The time to heal a surface pore in dry films. Material properties of dry PLGA films are used in the simulated results. Three levels of healing from finite element analysis show a decelerating healing process. The observed healing time at low temperatures fit between 85% and 87% of healing predicted by simulation.

4.13 Discussion

While Fig. 4.15 shows that the numerical predictions are generally consistent with the experimental observations, the experimental healing times appear to be significantly longer than expected at lower temperatures. It is conjectured that this is a result of changes in material properties associated with annealing, as a result of relatively long healing times at low temperatures.

When different samples of the dry PLGA were held isothermally in a TGA experiment for 8 hours at temperatures above T_g (50 °C – 65 °C), the kinetics of solvent escape were remarkably similar. During the first 20 minutes, the amount of solvent that had left the films at a given time increased with increasing temperature. However, after 2 hours the values stabilized or were following similar trends towards a final value of 98.3%, consistent with a residual solvent content of about 1.7%. Residual solvent acts as a plasticizer to the polymer, and effectively decreases the viscosity.

To elucidate the effects of annealing, samples of the PLGA were held isothermally in a TGA experiment for 8 hours at temperatures varying from 50 °C to 65 °C. The initial rate of solvent evaporation increased with temperature. However, after two hours, there was no further evaporation, and the final weight loss indicated that the initial residual solvent content had been about 1.7%. This residual solvent acts as a plasticizer to the polymer, and effectively decreases the viscosity [74]. It is conjectured that it was this effect that led to the longer-than expected healing times.

The most important visco-elastic property of the films, from the perspective of pore healing, is the viscosity represented by the second dashpot (η_m) in Fig. 4.14(a). The effects of annealing on this viscosity were investigated by holding the film isothermally at 65 °C for up to two hours. DMA was then used to measure the glass-transition temperature, and stress-relaxation measurements were used to determine the viscosity. These results showed that annealing raised the glass-transition temperature, increased the viscosity and dropped the activation energy. But the instantaneous modulus was not affected much. These changes are summarized in Table 4.2 for different annealing times 65 °C.It should be noted that the time scales over which the relaxation data were obtained (see Fig.4.8, for example) were much smaller than the time scales over which significant annealing might occur. Therefore, it is believed that annealing did not occur while the relaxation data were being collected.

Table 4.2: Effect of annealing on the dry PLGA parameters at 65°

Annealing Time (hr)	T_g(°C)	η_{m_0}(MPa s)	Q_m (kJ/mol)
0	38.4 ± 0.3	1.5E-30 ±6.9E-32	198 ±9
0.5	47± 0.3	2.0E-20±2.1E-21	136 ±13
1	49.5± 0.3	2.0E-22±1.9E-23	150 ±13
2	50.8± 0.3	2.8E-22±2.1E-23	149 ±11

In addition to the changes in the bulk properties of the PLGA, measurements of the contact angle strongly suggest that the polymer-air interfacial tension may also change significantly during incubation. Annealing at 65 °C reduced the interfacial tension to 25 ± 3 mN/m from 31 ± 2 mN/m.

Finite-element simulations of pore healing were performed using the most extreme values of the material properties given in Table 4.2 (to provide an upper bound on the healing time). These results are presented in Fig. 4.16. As can be seen from this figure, while the use of the unannealed properties provide excellent predictions for the behavior at high temperatures, the use of annealed properties provide better predictions at the lower temperatures. At the higher temperatures, the total time required to heal the film is comparable to the annealing time, so most of the healing occurs before full annealing. However, at lower temperatures, the time scales for annealing are smaller than the time scales for healing, so the results are more affected by the annealing. This is expected since the activation energy for solvent evaporation of 43 ± 6 kJ/mol is smaller than the activation energy for viscous flow.

In many materials, surface pores can also heal by surface diffusion; for example, this is the mechanism often ascribed to the healing of pores in high-temperature ceramics [75–77]. However, this does not appear to be the case for PLGA. First, the healing data does seem to be quite well described by the visco-elastic properties of the PLGA. Second, surface diffusion tends to have a lower activation energy than the bulk diffusive processes responsible for flow. This would decrease the healing time at low temperatures below that predicted from viscous flow. The opposite trend was observed, so the discrepancy in healing times is not a result of surface diffusion; rather it is a result of solvent evaporation, as discussed above.

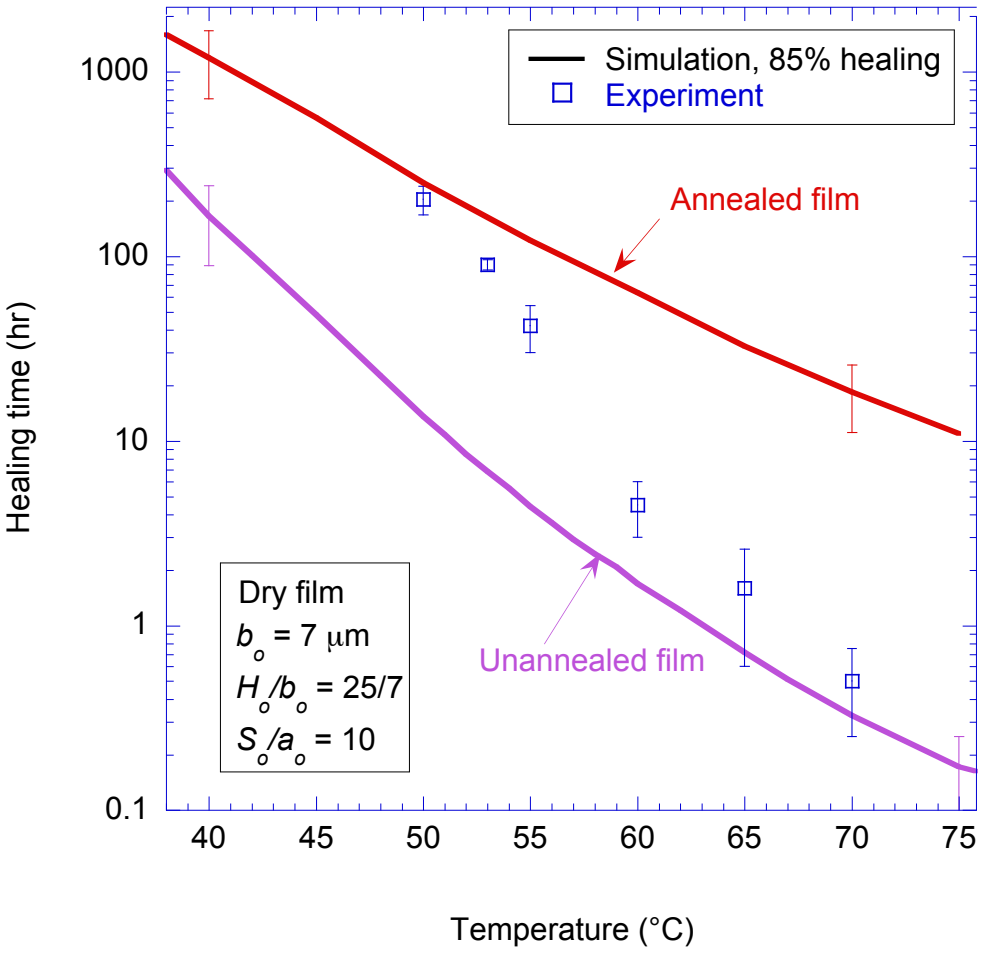

Figure 4.16: Healing of PLGA with annealing of dry films at elevated temperatures considered. The annealed films have higher glass transition temperatures, lower interfacial tension, and are more viscous. Therefore, healing in annealed films require longer time. While simulation of healing of unannealed films agrees with healing at high temperatures, annealing affects healing at long times more significantly.

4.14 Conclusions

Self-healing in PLGA can be modeled by flow driven by internal stress fields established by surface-tension effects. A finite-element model incorporating a numerical method to calculate the evolution of surface curvatures was developed to analyze indent healing in visco-elastic materials. The rate of healing surface pores decreases as the pores heal, with the pore depth approaches zero asymptotically. The visco-elastic properties of PLGA films were characterized using a combination of DMA and stress-relaxation tests. The dry PLGA films used in this study had a relatively high instantaneous modulus of 1.6 ± 0.3 GPa, and a glass transition temperature of 38.4 ± 0.3 °C. The PLGA displayed relaxation mechanisms with at least two distinct time scales. The first mechanism is a fast one with a very short time constant; this reduced the modulus by 99.9% at a time scale of less than a minute at temperatures above glass transition temperature, leaving the film with a partially-relaxed modulus of 1.5 ± 0.5 MPa. This modulus, although being much smaller than the instantaneous modulus, is still too big for healing to occur. A second relaxation mechanism with a much longer time constant was responsible for viscous flow that could accommodate pore healing.

Finite-element simulations of indent healing using material properties that had been independently measured were broadly consistent with earlier experimental observations reported by Mazzara et al. [14]. It was noted that annealing of the films, which is associated with solvent evaporation, resulting in longer healing times than expected at lower temperatures.

Since the healing mechanism is thermally activated, temperature is one of the most important factors in self-healing of PLGA. The temperature needs to be high enough for viscous flow to occur during the time scales of interest. In addition to the temperature, the indent geometry also affects healing time, with larger indents requiring longer time to heal. While this present study has focused on the healing of indents as a model for surface pores in PLGA films, we believe that the numerical tools used to analyze the process and the experimental techniques used to deduce the relevant material properties will be appropriate for predicting the pore-healing processes of significance for pharmaceutical use of these materials.

CHAPTER 5

Conclusions

In this dissertation, some of the aspects of the formation and healing of cracks and pores in polymeric materials have been studied. These two types of features are easy to obtain and are of nano-sizes. Therefore they have been used as functional nanostructures. Cracks can be introduced by applying a tensile strain to a layered structure of a brittle thin film of oxidized PDMS or hPDMS on a compliant PDMS substrate, and can be used for nanofabrication purposes [1, 2, 7, 16]. The nanochannels fabricated by tunneling cracking are normally closed and adjustable, with applications in biological research of DNA linearization [2]. Polymeric materials are usually intrinsically porous [68]. Healing of pores in PLGA microparticles is critical for the quality of the encapsulation and release of drugs and peptides [12, 69]. The extensive experimental results in literature showed great potentials of these techniques. However, to use these techniques to their full capacity, the underlying physics and mechanics need to be studied for the purpose of prediction and control of the behaviors. These have been the focus of this dissertation.

Cracks are initiated from flaws in material. Therefore, cracking is usually considered a stochastic process. The statistic aspect of defect lengths affect the formation of crack arrays in linear-elastic systems through the dependence of energy-release rate for channeling a crack on its crack length and the distance to its nearest longer neighbors. These two aspects need to be addressed differently to control the formation of crack arrays. In Chapter 2, different control strategies have been developed for systems with sufficient long flaws and with only small defects respectively. Finite element analyses were used for the energy-based approach, while Monte Carlo simulation was used to study the effect of statistics of the flaw population. In the statistical model, LEFM was used as the criterion for crack channeling. Thus the statistical model has the capability to study the interaction between LEFM, the statistics of a flaw population and the artificial geometrical features in producing uniform crack arrays. In a system with only small flaws, sharp geometrical features and high levels of applied strain are required to create controlled arrays. This approach

is suitable for materials that have few flaws such as silicon and silicon nitride. However, it is vulnerable to accidental damage to the material. For a system with sufficient long flaws, controlled crack arrays require careful matching the spacing of geometrical features, applied strain and the material properties. This is a more robust approach, and has lower requirement on the sharpness of the geometrical features. The crack control strategies were implemented in different combinations of materials and was shown to be effective [5, 7]. The analyses for controlled cracking in silicon and silicon nitride films were consistent with the experimental observations reported by Nam *et al.* [4].

Nanochannels fabricated by tunneling cracking are normally closed, and are completely reversible by application and relaxation of the remote tension. The adjustable channels can be applied to mechanically linearize DNA and chromatin [2] utilizing the nanoconfinement provided by the closed channel resulted from relaxation of the applied tension. The existence of fluid in the channels make the channel narrowing process to be time-dependent. In Chapter 3, this time-dependent narrowing of nanochannels is studied. The narrowing process involves the coupling of the stress field in the elastic channel wall, the fluid pressure, the pressure driven flow and the displacements of the inner surface of the channel. Analytical solution for an infinitely long axisymmetric thick-walled tube showed a gradual narrowing initiating from the ends of the tube. The normalized distance of collapse front traveling z/R_1 and normalize time tE/η has a quadratic relationship. A numerical method was developed to study the complete closure of a channel with finite length and elliptic cross-section. This provides a good approximation for the tunneling cracks. It was shown that a longer channel with higher initial aspect ratio in the closed state requires longer time to completely close. The time for the center of a channel to close is related to the square of channel length.

In Chapter 3, the time-dependency of the channel narrowing process was due to the viscosity of the fluid, while the channel wall was entirely elastic. In Chapter 4, the time-dependent healing of pores in a visco-elastic material was studied. Self-healing in PLGA was modeled by flow driven by internal stress fields established by surface-tension effects. The visco-elastic properties of dry PLGA films were characterized by means of DMA and stress relaxation tests. The PLGA displayed at least two distinct relaxation mechanisms. The first mechanism is active at short time scales, reducing the modulus from a relatively high instantaneous value of 1.6 ± 0.3 GPa to 1.5 ± 0.5 MPa. This partially-relaxed modulus is still too big for healing to occur. The second relaxation mechanism at long time scales was responsible to achieve pore healing in PLGA above glass transition temperatures.

A finite element model with the capability to calculate the evolution of surface curvatures was developed to analyze the healing of surface pores. Finite-element simulations using the independently measured material properties were consistent with earlier experimental observations reported by Mazzara *et al.* [14]. The healing of dry PLGA films exhibits additional temperature dependency besides the thermally activated viscosity. This is associated with solvent evaporation, which results in longer healing times than expected at low temperatures. The visco-elastic properties of annealed dry PLGA films were measured. Numerical calculation results using the properties of annealed PLGA were consistent with the experimental observations.

APPENDIX A

Appendix to Chapter 4

ABAQUS user-subroutine

```
C-------------------------------------
C Manipulate user exernal files
C-------------------------------------
      SUBROUTINE UEXTERNALDB(LOP,LRESTART,TIME,DTIME,KSTEP,KINC)
C
      INCLUDE 'ABA_PARAM.INC'
C
      CHARACTER xoutdir*255, xfname*80
      CHARACTER dmkname*255, FNAMEX*80
C
      DIMENSION TIME(2)
C
      lxfname = 0
      lxoutdir = 0
      xfname  =' '
      xoutdir  =' '
      call getjobname(xfname,lxfname)     !input file name
      call getoutdir(xoutdir,lxoutdir)    !output directory
C
      IF(LOP.EQ.0) THEN
C LOP=0, SUBROUTINE IS BEING CALLED AT START OF ANALYSIS
        fnamex=dmkname(xfname(1:lxfname),xoutdir(1:lxoutdir),'.96')
        OPEN(UNIT=96,FILE=FNAMEX,STATUS='UNKNOWN',FORM='FORMATTED')
C
C
      ELSE IF(LOP .EQ. 3) THEN
        CLOSE(UNIT=96)
```

```
C
      END IF
C
C
      RETURN
      END
c
c  Compose a filename directory/jobname.exten

      character*(*) function dmkname(fname,dname,exten)
C
      character*(*) fname,dname,exten
C     fname  I   jobname
C     dname  I   directory
C     exten  I   extension
C     dmkname O directory/jobname.exten

      ltot = len(fname)
      lf = 0
      do k1 = ltot,2,-1
        if (lf.eq.0.and.fname(k1:k1).ne.' ')  lf = k1
      end do

      ltot = len(dname)
      ld = 0
      do k1 = ltot,2,-1
        if (ld.eq.0.and.dname(k1:k1).ne.' ')  ld = k1
      end do

      ltot = len(exten)
      le = 0
      do k1 = ltot,2,-1
        if (le.eq.0.and.exten(k1:k1).ne.' ')  le = k1
      end do

      if ((lf + ld + le) .le. len(dmkname)) then
        dmkname = dname(1:ld)//'/'//fname(1:lf)
        ltot = ld + lf + 1
```

```
        if ( le.gt.0) then
           dmkname = dmkname(1:ltot)//exten(1:le)
        end if
      end if
C
      return
      end
C-------------------------------------------------------
C URDFIL -- User subroutine to read the results file -
C      called at the end of any increment in which new
C      information is written to the results file.
C-------------------------------------------------------
      SUBROUTINE URDFIL(LSTOP,LOVRWRT,KSTEP,KINC,DTIME,TIME)
C
      INCLUDE 'ABA_PARAM.INC'
C
      DIMENSION ARRAY(513),JRRAY(NPRECD,513),TIME(2)
      EQUIVALENCE (ARRAY(1),JRRAY(1,1))
C     Variables
      REAL OLDDSP(1000,2),CRD(1000,2),ELCRDEQ(1000,2)
      REAL F(1000), MAG(1000), KAPPA(1000),T(1000,2)
      INTEGER ENDOFSTEP, ENDOFINC, I, J, K, NNDT,NELT,NND,NEL,NINFTY,
     1  ALLELN(10000),ALLELNDN(10000,4),NONUM(1000),NNUM(1000),
     2  ELNUM(1000),ELNDN(1000,4),K1,K2,K3
        DOUBLE PRECISION X1L,Y1L,X2L,Y2L,NX,NY,X0,Y0,X1,Y1,X2,Y2,
     1  DZDR,D2ZDR2,A
C     Set common variables
      COMMON /coordinates/CRD /elementinfo/NEL,ELNUM /load/MAG,T
C     Set gamma (GAMMA1) as the surface energy
      REAL GAMMA1
      GAMMA1= 6.0D-5 !MPa mm
C     Initialize total number of elements and nodes
      NNDT=100000
      NELT=100000
      NINFTY=100000000 ! An extremely large number
      I=0
      J=0
      K=0
```

```
      K1=1
      K2=1
      K3=1
      ENDOFSTEP=0
      ENDOFINC=0
      NNOD=0
      NNEL=0
      DO 110 I=1,NINFY
        CALL DBFILE(0,ARRAY,JRCD)
        IF(JRCD .NE. 0) THEN
            END0FSTEP=1
            CALL DBFILE(2,ARRAY,JRCD)
            GOTO 111
        ENDIF
        IF(ENDOFSTEP .NE. 1) THEN
            KEY=JRRAY(1,2)
            IF (KEY .EQ. 1900) THEN
                 ALLELN(K1)=JRRAY(1,3)
                 DO 120 J=1,4
                     ALLELNDN(K1,J)=JRRAY(1,(J+4))
120              CONTINUE
C WRITE(96,3000) ALLELN(K1),ALLELNDN(K1,:)
C3000 FORMAT(2X,'EL#',I5,5X,I8,2X,I8,2X,I8,2X,I8,2X
C     1                  ,I8,2X,I8,2X,I8,2X,I8,2X)
                 J=0
                 K1=K1+1
            ENDIF
        ENDIF
110   CONTINUE
111   CONTINUE
      NELT=K1-1
      WRITE (96,3010) NELT
3010  FORMAT(2X,'Total number of elements: 'I5)
      I=0
      K1=1
      ENDOFSTEP=0
C=======================================================
C     Set the position in the results file to be the current
```

```
C     step and increment
C     ARRAY here returns key 2000 only, increment start record.
C=======================================================
C
      CALL POSFIL(KSTEP,KINC,ARRAY,JRCD)
C
      ENDOFSTEP=0
      IF(JRCD .NE. 0) THEN
        ENDOFSTEP=1
      ENDIF
      IF(ENDOFSTEP .NE. 1)THEN
C        WRITE(96,3020) JRRAY(1,8), JRRAY(1,9)
C3020    FORMAT(1X,'**STEP',I2,'INCREMENT',I3)
        DO 130 K=1,NINFTY
            CALL DBFILE(0,ARRAY,JRCD)
            ENDOFINC=0
            IF(JRCD .NE. 0) THEN
                ENDOFINC=1
                GOTO 131
            ENDIF
            IF(ENDOFINC .NE. 1)THEN
                KEY=JRRAY(1,2)
C--Node Displacement-----------------------------------------
                IF(KEY .EQ. 101) THEN
                    NONUM(K1)=JRRAY(1,3)  !Node number
                    DO 140 I=1,2
                         OLDDSP(K1,I)=ARRAY(I+3)
140                 CONTINUE
                    I=0
                     K1=K1+1
                ENDIF
C--End Node Displacement-------------------------------------
C--Node Coordinate-------------------------------------------
                IF(KEY .EQ. 107) THEN
                    NNUM(K2)=JRRAY(1,3)
                    DO 150 I=1,2
C                      CRDLIN(K2,I)=ARRAY(I+3)
                        CRD(K2,I)=ARRAY(I+3)
```

```
150                 CONTINUE
                    I=0
C                    WRITE( 96, 3040) NNUM(K2),CRD(K2,:)
C3040                FORMAT(2X,'Node'I4,5X,'X_OLD'ES12.5E2,5X,
C     1                     'Y_OLD'ES12.5E2,5X)
                    K2=K2+1
                ENDIF
C--End Node Coordinate-----------------------------------------
C--Element Header----------------------------------------------
                IF(KEY .EQ. 1) THEN
                    ELNUM(K3)=JRRAY(1,3)
C                    WRITE(96,3050) ELNUM(K3),K3
C3050               FORMAT(2X,'Element',I8,2X,'Counter(K3)=',I8)
                     K3=K3+1
                ENDIF
C--End Element Header------------------------------------------
            ENDIF !(ENDOFINC .NE. 1)
130     CONTINUE
131     CONTINUE
        K=0
        NNOD=K1-1
        NEL=(K3-1)/2
C        WRITE(96,3060) NNOD,NEL
C3060    FORMAT(2X,'#NODE',I8,2X,'#EL',I8)
C        DO 160 I=1,NNOD
C           DO 170 J=1,2
C               CRD(I,J)=CRDLIN(I,J)+OLDDSP(I,J)
C170        CONTINUE
C           J=0
C160     CONTINUE
C        I=0
C For each ELNUM, locate in ALLELN find all the node connections
        DO 180 I=1,NEL
           DO 190 J=1,NELT
              IF(ALLELN(J) .EQ. ELNUM(I)) THEN
                 ELNDN(I,:)=ALLELNDN(J,:)
              ENDIF
190        CONTINUE
```

```
           J=0
180      CONTINUE
         I=0
C For each Element numbered as ELNUM,
C find the load equivalent point Coordinates
         DO 200 I=1,NEL
            ELCRDEQ(I,1)=0
            ELCRDEQ(I,2)=0
            DO 210 J=1,NNOD
               DO 220 K=1,4
                    IF(ELNDN(I,K) .EQ. NNUM(J))THEN
                      ELCRDEQ(I,1)=ELCRDEQ(I,1)+CRD(J,1)/2.0D0
                      ELCRDEQ(I,2)=ELCRDEQ(I,2)+CRD(J,2)/2.0D0
                    ENDIF
220            CONTINUE
210         CONTINUE
C                WRITE(96,3100)ELNUM(I),ELCRDEQ(I,:)
C3100            FORMAT('Element',I5,5X,'Equi X=',ES12.5E2,5X,
C     1'Y=',ES12.5E2)
200      CONTINUE
C Assume all elements on the surface are numbered orderly
C Calculate the curvature for each element
C X, Y Denotes r and z in axisymmetric coordinate system
         DO 230 I=2,NEL-1
            X0=ELCRDEQ(I,1)
            Y0=ELCRDEQ(I,2)
            X1=ELCRDEQ(I-1,1)
            Y1=ELCRDEQ(I-1,2)
            X2=ELCRDEQ(I+1,1)
            Y2=ELCRDEQ(I+1,2)
            NX= -(Y2-Y1)/SQRT((Y2-Y1)**2+(X2-X1)**2)
            NY= (X2-X1)/SQRT((Y2-Y1)**2+(X2-X1)**2)
            X1L= NY*(X1-X0)-NX*(Y1-Y0)
            Y1L= NX*(X1-X0)+NY*(Y1-Y0)
            X2L= NY*(X2-X0)-NX*(Y2-Y0)
            Y2L= NX*(X2-X0)+NY*(Y2-Y0)
             KAPPA(I)=2*A-NX/X0
             T(I,1)=NX
```

```
            T(I,2)=NY
C            WRITE(96,3110) ELNUM(I),A,KAPPA(I),T(I,1),T(I,2)
C3110        FORMAT('Element',I5,5X,'A=',D12.5,'KAPPA='D12.5,
C     1                '(',D12.5,',',D12.5,')')
230     CONTINUE
C For the elements at the ends
C For the element at the symmetry,
C if it's the first element in the array,
           X0=ELCRDEQ(1,1)
           Y0=ELCRDEQ(1,2)
           X1=-ELCRDEQ(1,1)
           Y1=ELCRDEQ(1,2)
           X2=ELCRDEQ(2,1)
           Y2=ELCRDEQ(2,2)
           NX= -(Y2-Y1)/SQRT((Y2-Y1)**2+(X2-X1)**2)
           NY= (X2-X1)/SQRT((Y2-Y1)**2+(X2-X1)**2)
           X1L= NY*(X1-X0)-NX*(Y1-Y0)
           Y1L= NX*(X1-X0)+NY*(Y1-Y0)
           X2L= NY*(X2-X0)-NX*(Y2-Y0)
           Y2L= NX*(X2-X0)+NY*(Y2-Y0)
           A=((X1L**2)*Y1L+(X2L**2)*Y2L)/(X1L**4+X2L**4)
            KAPPA(1)=2*A-NX/X0
            T(1,1)=NX
            T(1,2)=NY
C For the element at the far end,
C approximate with its left neighbor.
           KAPPA(NEL)=KAPPA(NEL-1)
            T(NEL,1)=T(NEL-1,1)
            T(NEL,2)=T(NEL-1,2)
        DO 240 I=1,NEL
           MAG(I)=KAPPA(I)*GAMMA1
C            WRITE(96,3070)ELNUM(I),I,MAG(I)
C3070        FORMAT('ELNUM=',I8,5X,'MAG(',I5,1X,')',E10.3,5X)
240     CONTINUE
      ENDIF
      I=0
      J=0
      K=0
```

```
      RETURN
      END

      SUBROUTINE UTRACLOAD(ALPHA,T_USER,KSTEP,KINC,TIME,NOEL,NPT,
     1 COORDS,DIRCOS,JLTYP,SNAME)
C
      INCLUDE 'ABA_PARAM.INC'
C
      DIMENSION T_USER(3), TIME(2), COORDS(3), DIRCOS(3,3)
      CHARACTER*80 SNAME
      INTEGER I,NEL,ELNUM(1000)
      REAL MAG(1000),T(1000,2)
      COMMON /coordinates/CRD /elementinfo/NEL,ELNUM
     1/load/MAG,T
      IF(JLTYP .EQ. 521 .OR. JLTYP.EQ.522 .OR. JLTYP.EQ.523
     1      .OR. JLTYP.EQ.524 .OR. JLTYP.EQ.525
     2      .OR. JLTYP.EQ.526) THEN
         DO 260 I=1,NEL
            IF(NOEL .EQ.ELNUM(I))THEN
               ALPHA=MAG(I)
               T_USER(1)=T(I,1)
               T_USER(2)=T(I,2)
               T_USER(3)=0
            ENDIF
260      CONTINUE
      ENDIF
      RETURN
      END
```

BIBLIOGRAPHY

[1] K. L. Mills, D. Huh, S. Takayama and M. D. Thouless. Instantaneous fabrication of arrays of normally closed, adjustable, and reversible nanochannels by tunnel cracking. *Lab on a Chip*, 10:1627–1630, 2010.

[2] T. Matsuoka, B. C. Kim, J. Huang, N. J. Douville, M.D. Thouless and S. Takayama. Nanoscale squeezing in elastomeric nanochannels for single chromatin linearization. *Nano Letters*, 12:6480–6484, 2012.

[3] N. Douville, Z. Li, S. Takayama and M. D. Thouless. Crack channelling in a metal-coated elastomer. *Soft Matter*, 7:6493–6500, 2011.

[4] K. H. Nam, I. H. Park and S. H. Ko. Patterning by controlled cracking. *Nature*, 485:221–224, 2012.

[5] B. C. Kim,C. Morales, J. Huang, T. Matsuoka, S. Takayama, M. D. Thouless. Fracture-based fabrication of normally-closed, adjustable and fully reversible micro-scale fluidic channels. *Small*, Accepted, 2014.

[6] D. Huh, K. L. Mills, M. D. Thouless and S. Takayama. Tunable elastomeric nanochannels for nanofluidic manipulation. *Nature Materials*, 6:424–428, 2007.

[7] B. C. Kim, T. Matsuoka, C. Morales, J. Huang, M.D. Thouless and S. Takayama. Guided fracture of films on soft substrates to create micro/nano-feature arrays with controlled periodicity. *Scientific Reports*, 3, 2013.

[8] H. Park, M. Radisic, J. O. Lim, B. H. Chang, and G. Vunjak-Novakovic. A novel composite scaffold for cardiac tissue engineering. *In Vitro Cellular & Developmental Biology-Animal*, 41(7):188–196, 2005.

[9] M. L. Hans and A. M. Lowman. Biodegradable nanoparticles for drug delivery and targeting. *Current Opinion in Solid State and Materials Science*, 6(4):319–327, 2002.

[10] J. Cheng, B. A. Teply, I. Sherifi, J. Sung, G. Luther, F. Gu, E. Levy-Nissenbaum, A. F. Radovic-Moreno, R. Langer, and O. C. Farokhzad. Formulation of functionalized plga–peg nanoparticles for in vivo targeted drug delivery. *Biomaterials*, 28(5):869–876, 2007.

[11] C. Wischke and S. P. Schwendeman. Principles of encapsulating hydrophobic drugs in pla/plga microparticles. *International Journal of pharmaceutics*, 364(2):298–327, 2008.

[12] S. E. Reinhold, K. H. Desai, L. Zhang, K. F. Olsen, and S. P. Schwendeman. Self-healing microencapsulation of biomacromolecules without organic solvents. *Angewandte Chemie International Edition*, 51(43):10800–10803, 2012.

[13] J. Wang, B. M. Wang, and S. P. Schwendeman. Characterization of the initial burst release of a model peptide from poly (d, l-lactide-co-glycolide) microspheres. *Journal of controlled release*, 82(2):289–307, 2002.

[14] J. M. Mazzara, M. A. Balagna, M. D. Thouless, and S. P. Schwendeman. Healing kinetics of microneedle-formed pores in PLGA films. *Journal of Controlled Release*, 171(2):172 – 177, 2013.

[15] R. Adelung, O. C. Aktas, J. Franc, A. Biswas, R. Kunz, M. Elbahri, J. Kanzow, U. Schürmann and F. Faupel. Controlled growth of nanowires within thin-film cracks. *Nature Materials*, 3:375–379, 2004.

[16] X. Zhu, K. L. Mills, P.R. Peters, J. H. Bahng, E. H. Liu, J. Shim, K. Naruse, M. E. Csete, M. D. Thouless and S. Takayama. Fabrication of reconfigurable protein matrices by cracking. *Nature Materials*, 4:403–406, 2005.

[17] D. Faruqui and A. Sharma. Stress engineered polymeric nanostructures by self-organized splitting of microstructures. *Industrial Engineering and Chemical Research*, 47:6374–6378, 2008.

[18] R. B. Henstenburg and S. L. Phoenix. Interfacial shear strength studies using the single-filament-composite test. part ii: A probability model and monte carlo simulation. *Polymer Composites*, 10:389–408, 1989.

[19] W. A. Curtin. Fiber fragmentation in a single-filament composite. *Applied Physics Letters*, 58:1155–1157, 1991.

[20] M. Heinrich, P. Gruber, S. Orso, U. A. Handge and R. Spolenak. Dimensional control of brittle nanoplatelets. a statistical analysis of a thin film cracking approach. *Nano Letters*, 6:2026–2030, 2006.

[21] A. C. Kimber and J. G. Keer. On the theoretical average crack spacing in brittle matrix composites containing continuous aligned fibres. *Journal of Materials Science Letters*, 1:353–354, 1982.

[22] X. F. Yang and K. M. Knowles. The one-dimensional car parking problem and its application to the distribution of spacings between matrix cracks in unidirectional fiber-reinforced brittle materials. *Journal of the American Ceramic Society*, 75:141–147, 1992.

[23] M. D. Thouless. Crack spacing in brittle films on elastic substrates. *Journal of the American Ceramic Society*, 73:2144–2146, 1990.

[24] M. D. Thouless, E. Olsson and A. Gupta. Cracking of brittle films on elastic substrates. *Acta Metallurgica et Materialia*, 40:1287–1292, 1992.

[25] J. W. Hutchinson and Z. Suo. Mixed mode cracking in layered materials. *Advances in Applied Mechanics*, 29:63–191, 1992.

[26] V. B. Shenoy, A. F. Schwartzman and L. B. Freund. Crack patterns in brittle thin films. *International Journal of Fracture*, 103:1–17, 2000.

[27] M. D. Thouless, Z. Li, N. J. Douville and S. Takayama. Periodic cracking of films supported on compliant substrates,. *Journal of the Mechanics and Physics of Solids*, 59:1927–1937, 2011.

[28] T. Y. Zhang and M. H. Zhao. Equilibrium depth and spacing of cracks in a tensile residual stressed thin film deposited on a brittle substrate. *Engineering Fracture Mechanics*, 69:589–596, 2002.

[29] T. Ye, Z. Suo and A. G. Evans. Thin film cracking and the roles of substrate and interface. *International Journal of Solids and Structures*, 29:2639–2648, 1992.

[30] J. Dundurs. Edge-bonded dissimilar orthogonal elastic wedges. *Journal of Applied Mechanics*, 36:650–652, 1969.

[31] H. Tada, P. C. Paris and G. R. Irwin. *The Stress Analysis of Cracks Handbook, 3rd ed.* The American Society of Mechanical Engineers, New York, NY, 2000.

[32] J. L. Beuth, Jr. Cracking of thin films bonded in residual tension. *International Journal of Solids and Structures*, 29:1657–1675, 1992.

[33] D. W. Pashley. A study of the deformation and fracture of single-crystal gold films of high strength inside an electron microscope. *Proceedings of the Royal Society*, A255:218–231, 1960.

[34] M. T. Todinov. Statistics of defects in one-dimensional components. *Computational Materials Science*, 24(4):430– 442, 2002.

[35] S. Karlin and H. E. Taylor. *A first course in stochastic processes*. Access Online via Elsevier, 1975.

[36] C. E. Inglis. Stresses in a plate due to the presence of cracks and sharp corners. *Proceedings of the Institute of Naval Architects*, 55:219–230, 1913.

[37] M. D. Thouless. Modeling the development and relaxation of stresses in films,. *Annual Review of Materials Science*, 25:69–96, 1995.

[38] A. R. Dixon, C. Moraes, M. E. Csete, M. D. Thouless, M. A. Philbert, and S. Takayama. One-dimensional patterning of cells in silicone wells via compression-induced fracture. *Journal of Biomedical Materials Research Part A*, 2013.

[39] C. Moraes, B. C. Kim, X. Zhu, K. L. Mills, A. R. Dixon, M. D. M. D. Thouless, and S. Takayama. Defined topologically-complex protein matrices to manipulate cell shape via three-dimensional fiber-like patterns. *Lab on a Chip*, 2014.

[40] D. Huh, H. J. Kim, J. P. Fraser, D. E. Shea, M. Khan, A. Bahinski, G. A. Hamilton, and D. E. Ingber. Microfabrication of human organs-on-chips. *Nature Protocols*, 8(11):2135 – 2157, 2013.

[41] J. Huang, B. C. Kim, S. Takayama, and M. D. Thouless. The control of crack arrays in thin films. *Journal of Materials Science*, 49(1):255–268, 2014.

[42] M. C. Cheng, A. T. Leske, T. Matsuoka, B. C. Kim, J. S. Lee, M. A. Burns, S. Takayama, and J. S. Biteen. Super-resolution imaging of pdms nanochannels by single-molecule micelle-assisted blink microscopy. *The Journal of Physical Chemistry B*, 117(16):4406–4411, 2013.

[43] M. Li and J. G. Brasseur. Non-steady peristaltic transport in finite-length tubes. *Journal of Fluid Mechanics*, 248:129–151, 2 1993.

[44] O. Eytan and D. Elad. Analysis of intra-uterine fluid motion induced by uterine contractions. *Bulletin of Mathematical Biology*, 61(2):221–238, 1999.

[45] K. P. Selverov and H. A. Stone. Peristaltically driven channel flows with applications toward micromixing. *Physics of Fluids*, 13(7):1837–1859, 2001.

[46] M. Yi, H. H. Bau, and H. Hu. Peristaltically induced motion in a closed cavity with two vibrating walls. *Physics of Fluids*, 14(1):184–197, 2002.

[47] N. Jeon, D. T. Chiu, C. J. Wargo, H. Wui, I. S. Choi, J. R. Anderson, and G. M. Whitesides. Microfluidics section: Design and fabrication of integrated passive valves and pumps for flexible polymer 3-dimensional microfluidic systems. *Biomedical Microdevices*, 4(2):117–121, 2002.

[48] M. A. Eddings and B. K. Gale. A pdms-based gas permeation pump for on-chip fluid handling in microfluidic devices. *Journal of Micromechanics and Microengineering*, 16(11):2396, 2006.

[49] M. Khoo and L. Chang. A novel micromachined magnetic membrane microfluid pump. In *Engineering in Medicine and Biology Society, 2000. Proceedings of the 22nd Annual International Conference of the IEEE*, volume 3, pages 2394–2397, 2000.

[50] M. A. Unger, H. P. Chou, T. Thorsen, A. Scherer, and S. R. Quake. Monolithic microfabricated valves and pumps by multilayer soft lithography. *Science*, 288(5463):113–116, 2000.

[51] R. D. Kamm and A. H. Shapiro. Unsteady flow in a collapsible tube subjected to external pressure or body forces. *Journal of Fluid Mechanics*, 95(01):1–78, 1979.

[52] D. Tang, C. Yang, S. Kobayashi, and D. N. Ku. Steady flow and wall compression in stenotic arteries: a three-dimensional thick-wall model with fluid–wall interactions. *Journal of Biomechanical Engineering*, 123(6):548–557, 2001.

[53] D. Tang, C. Yang, H. Walker, S. Kobayashi, and D. N. Ku. Simulating cyclic artery compression using a 3d unsteady model with fluid–structure interactions. *Computer & Structures*, 80(20):1651–1665, 2002.

[54] W. W. Schultz and S. H. Davis. One dimensional liquid fibers. *Journal of Rheology*, 26(4):331–345, 1982.

[55] T. T. Perkins, D. E. Smith, and S. Chu. Single polymer dynamics in an elongational flow. *Science*, 276(5321):2016–2021, 1997.

[56] E. E. Schmitt and R. A. Polistina. Surgical sutures. US Patent 3,297,033, 1 1971.

[57] B. D. Klugherz, P. L. Jones, X. Cui, W. Chen, N. F. Meneveau, S. DeFelice, J. Connolly, R. L. Wilensky, and R. J. Levy. Gene delivery from a dna controlled-release stent in porcine coronary arteries. *Nature Biotechnology*, 18(11):1181–1184, 2000.

[58] X. Wang, S. S. Venkatraman, F. YC Boey, J. SC Loo, and L. P. Tan. Controlled release of sirolimus from a multilayered plga stent matrix. *Biomaterials*, 27(32):5588–5595, 2006.

[59] C.J. Pan, J.J. Tang, Y.J. Weng, J. Wang, and N. Huang. Preparation and characterization of rapamycin-loaded plga coating stent. *Journal of Materials Science: Materials in Medicine*, 18(11):2193–2198, 2007.

[60] C. W. Patrick Jr, B. Zheng, C. Johnston, and G. P. Reece. Long-term implantation of preadipocyte-seeded plga scaffolds. *Tissue engineering*, 8(2):283–293, 2002.

[61] Y. Wang, G. A. Ameer, B. J. Sheppard, and R. Langer. A tough biodegradable elastomer. *Nature Biotechnology*, 20(6):602–606, 2002.

[62] J. H. Park, M. G. Allen, and M. R. Prausnitz. Biodegradable polymer microneedles: fabrication, mechanics and transdermal drug delivery. *Journal of Controlled Release*, 104(1):51–66, 2005.

[63] R. A. T. M. van Benthem, W. Ming, and G. de With. Self healing polymer coatings. In *Self Healing Materials*, pages 139–159. Springer Netherlands, 2008.

[64] G. O. Wilson, H. M. Andersson, S. R. White, N. R. Sottos, J. S. Moore, and P. V. Braun. *Self-Healing Polymers*. John Wiley & Sons, Inc., 2002.

[65] S. H. Cho, S. R. White, and P. V. Braun,. Self-healing polymer coatings. *Advanced Materials*, 21(6):645–649, 2009.

[66] K. S. Toohey, N. R. Sottos, J. A. Lewis, J. S. Moore, and S. R. White. Self-healing materials with microvascular networks. *Nature Materials*, 6:581–585, 2007.

[67] P. Vettiger, G. Cross, M. Despont, U. Drechsler, U. Durig, B. Gotsmann, W. Haberle, M. A. Lantz, H. E. Rothuizen, R. Stutz, and G. K. Binnig. The "millipede" - nanotechnology entering data storage. *Nanotechnology, IEEE Transactions on*, 1(1):39–55, 2002.

[68] S. Nakahara. Microporosity in thin films. *Thin Solid Films*, 64(1):149 – 161, 1979.

[69] J. Kang and S. P. Schwendeman. Pore closing and opening in biodegradable polymers and their effect on the controlled release of proteins. *Molecular pharmaceutics*, 4(1):104–118, 2007.

[70] J. Chakrabarty. *Theory of plasticity*. Butterworth-Heinemann, 2006.

[71] D. L. Henann and L. Anand. Surface tension-driven shape-recovery of micro/nanometer-scale surface features in a Pt57.5Ni5.3Cu14.7P22.5 metallic glass in the supercooled liquid region: A numerical modeling capability. *Journal of the Mechanics and Physics of Solids*, 58(11):1947 – 1962, 2010.

[72] D. Y. Kwok and A. W. Neumann. Contact angle measurement and contact angle interpretation. *Advances in Colloid and Interface Science*, 81(3):167–249, 1999.

[73] R. S. Lakes. *Viscoelastic materials*. Cambridge University Press, 2009.

[74] L. H. Sperling. *Introduction to physical polymer science*. John Wiley & Sons, Inc., 2005.

[75] A. G. Evans and E. A. Charles. Strength recovery by diffusive crack healing. *Acta Metallurgica*, 25(8):919–927, 1977.

[76] D. L. Smith and B. Evans. Diffusional crack healing in quartz. *Journal of Geophysical Research: Solid Earth (1978–2012)*, 89(B6):4125–4135, 1984.

[77] J. Rödel and A. M. Glaeser. High-temperature healing of lithographically introduced cracks in sapphire. *Journal of the American Ceramic Society*, 73(3):592–5601, 1990.